Predicting the Impact of Sex-specific Differences in Vascular Smooth Muscle Cells in Mechanisms of Hypertension

By

GONZALO HERNANDEZ HERNANDEZ
DISSERTATION

Submitted in partial satisfaction of the requirements for the degree of

DOCTOR OF PHILOSOPHY

in

Biophysics

in the

OFFICE OF GRADUATE STUDIES

of the

UNIVERSITY OF CALIFORNIA

DAVIS

Approved:

_____

Colleen E. Clancy, Chair

_____

Luis Fernando Santana

_____

Timothy J. Lewis

Committee in Charge

2022

Abstract

Hypertension is considered to be the largest modifiable risk factor for cardiovascular disease. Even with the longstanding recognition of hypertension as a disease, there is still poor understanding of the observable differences in men and women responses to antihypertensive agents. The necessity of treating hypertension to prevent premature death has led to the urgent need to develop new approaches for *revealing* sex-specific mechanisms of hypertension and *predicting* how drugs will alter vascular function. The smooth muscle cells that line the walls of small resistance arteries and arterioles have been the subject of investigation for decades due to their important role in regulating blood flow and blood pressure. This dissertation focuses on formulating an *in silico* model of the vascular smooth muscle cell incorporating new electrophysiological and Ca^{2+} signaling data suggesting key sex-specific differences in male and female arterial myocytes. The model highlights the importance of sex-specific differences in $Ca_V1.2$ and $K_V2.1$ channels. The $Ca_V1.2$ and $K_V2.1$ channels have previously been associated with remodeling in the pathogenesis of hypertension and model predictions described herein also suggest differential responses to antihypertensive agents. The work covered in this dissertation provides insights into sex-specific differences in arterial smooth muscle cell physiology and has the potential to expand our understanding for how sex-dependent differences in the expression, spatial organization, and function of key important ion channels are involved in the regulation of vascular smooth muscle.

Acknowledgments

First and foremost, I am deeply grateful and extremely humbled to my advisor, mentor, and dear friend Colleen Clancy for her unwavering support, motivation, cheering, and encouragement in the development of my dissertation. Colleen provided me with all the resources and direction I needed to begin my career as an independent scientist. Furthermore, Colleen and I went through a lot together, and she helped me through the most difficult times and uplifted me when sometimes I was on the verge of giving up. Because words cannot express my gratitude toward Colleen, I would like to dedicate my dissertation to her.

I am grateful to Fernando Santana for his guidance, knowledge, and patience. Fernando was always willing to spend the time necessary to share his knowledge and skills as a scientist with me. Fernando, thank you for repeatedly answering the same questions and for always having your door open to discuss science with me. I am also grateful to Igor Vorobyov and Tim Lewis for their ongoing support, feedback, and critique. Similarly, I would like to extend my gratitude to Pei-Chi Yang for her support and for training me with the computational techniques that were essential to the development of my dissertation.

To the current and former members of the Clancy lab, collaborators, and UC Davis classmates, I thank you for your friendship, thoughtful and fruitful scientific discussions, and for making UC Davis a stimulating place to do science, Divya Kernik, Parya Aghasafari, Kevin DeMarco, Mao-Tsuen Jeng, Brightany Li, Khoa Ngo, Mindy Tieu, John Grubbs, John R. Dawson, Kyle Rouen, Yanxiao Han, Steffen Docken, Emily Meyer, Adam Rose, Laura Guarina, Samantha O'Dwyer, Collin Matsumoto and Xianwei Zhang.

I will never forget the people who inspired and motivated me to continue a career in science, my friend Angie Polanco and my high school teachers Daniel Royster, Stephanie Norton, and Jim Broderick. Last but not least, I would like to extend my sincere thanks to my master's thesis advisor Yohannes Shiferaw for his support, guidance, and for paving the way for me to get to this point.

Finally, I could not have undertaken this journey without the unconditional love and support of my parents Aristeo and Ricarda, and my family Aurelio, Agustina, Matteo, Ariana, Diego, Gerardo, Veronica, Ricardo, Nayeli, Emmanuel, Mayra, Adrian, Damian, Analida, Lucio, Valerie, and Osvaldo.

Table of Contents

Abstract ……..……ii

Acknowledgments.…….…….…….……iii

List of Figures and Tables ….……...vii

List of Abbreviations ….……..……...…….……....ix

Chapter 1: Introduction…….1

1.1 The Cardiovascular System……...……..1

1.2 Cell size and structure of mesenteric vascular smooth muscle cells……..…….5

1.3 Ion channels and the electrophysiology of vascular smooth muscle cells……7

1.4 Excitation-Contraction coupling in vascular smooth muscle cells……12

Chapter 2: Mathematical modeling……..……15

2.1 Biophysical properties of the excitable cell membranes…..……15

2.2 Mathematical modeling of ionic currents……...19

2.3 Mathematical modeling of ion channel voltage-dependent gating……20

2.4 Computational methods……..22

2.4.1 Optimization of ionic currents…….…….22

2.4.2 Numerical integration……23

2.4.3 Noise……...24

2.5 General approach and hypotheses……26

Chapter 3: The Hernandez-Hernandez model of male and female vascular smooth muscle cell Ca^{2+} signaling and electrophysiology……...28

3.1 Abstract…….…28

3.2 Introduction……29

3.3 Experimental Methods…….……31

3.3.1 Animals……...……31

3.3.2 Isolation of arterial myocytes from systemic resistance arterioles……..31

3.3.3 Patch-clamp electrophysiology……..……32

3.4 Model development……34
3.5 Whole-cell male and female models……49
3.6 Results……51
3.7 Discussion……71
3.8 Limitations……79
3.9 Summary and key findings……80

Chapter 4: A stochastic model of ion channel formation in the plasma membrane of vascular smooth muscle cells……83
4.1 Abstract……83
4.2 Introduction……84
4.3 Methods……87
4.3.1 Immunofluorescence and super-resolution microscopy……87
4.3.2 tsA-201 cell transfection……89
4.3.3 Time-lapse confocal microscopy……90
4.3.4 Stochastic self-assembly model ……91
4.4 Results……94
4.5 Discussion……118

Chapter 5: The Hernandez-Hernandez model and future directions ……126
5.1 Conclusion……126
5.2 Future directions……128

References…………130

List of figures and tables

Figure 1.1 Diagram of the cardiovascular system.
Figure 1.2 Illustration of the three main compartments in vascular smooth muscle cells.
Figure 1.3 Excitation-Contraction coupling in VSMCs.
Figure 2.1 The cell membrane as a circuit.
Figure 2.2 Diagram of a two-state kinetic scheme of a subunit gate.
Figure 3.1 A schematic representation of the Hernandez-Hernandez model.
Figure 3.2 Membrane potential and ionic concentrations.
Figure 3.3 Ionic currents.
Figure 3.4 Calcium signaling.
Figure 3.5 L-type calcium currents ($I_{Cav1.2}$) were experimentally measured and modeled from male and female vascular smooth muscle cells.
Figure 3.6 Experimentally measured and modeled potassium (K_V) currents from male and female vascular smooth muscle cells.
Figure 3.7 Experimentally measured and modeled large-conductance Ca^{2+}-activated K^+ (BK_{ca}) currents.
Figure 3.8 Membrane potential from experiments and simulations in male and female vascular smooth muscle myocytes.
Figure 3.9 Differential effects of voltage-gated potassium current (I_{KVTOT}) block in male and female myocytes.
Figure 3.10 Simulated effects of L-type calcium currents ($I_{Cav1.2}$) and calcium influx in male and female vascular smooth muscle cells.
Figure 3.11 Predicted acute responses of membrane potential and intracellular calcium $[Ca]_{cyt}$ to selective channel blockers.
Figure 4.1. In silico stochastic self-assembly model.
Figure 4.2. Channel clustering.
Figure 4.3. The distributions of $Ca_V1.2$, TRPV4, and BK channels in smooth muscle cells could be explained by the stochastic self-assembly of clusters.
Figure 4.4. Time course of the formation of $Ca_V1.2$ channel clusters in tsA-201 cells.
Figure 4.5. Time course of the formation of TRPV4 channel clusters in tsA-201 cells.
Figure 4.6. Dwell times for $Ca_V1.2$ and TRPV4 channels in tsA-201 cell are fast.
Figure 4.7. P_g and P_R determine channel and cluster dwell time.
Figure 4.8. In silico stochastic self-assembly of protein clusters with realistic sizes and densities.
Figure 4.9. Sigmoidal time-dependent changes in P_g, P_n, and P_R reproduce the time course of $Ca_V1.2$ cluster formation in the plasma membrane of tsA-201 cells.
Figure 4.10. Sigmoidal time-dependent changes in P_g, P_n, and P_R reproduce the time course of TRPV4 cluster formation in the plasma membrane of tsA-201 cells.
Figure 4.11. Feedback model for $Ca_V1.2$ cluster formation
Figure 4.12. Feedback model for TRPV4 cluster formation.
Figure 5.1. Extended VSMCs model.

Table 1.1 Ionic concentrations of Na^+, K^+, Cl^- and Ca^{2+}.
Table 1.2 Potassium channels in mesenteric VSMCs
Table 1.3 Main features of the voltage-gated L-type $Ca_V1.2$ channels
Table 1.4 Transient receptor potential (TRP) family of ion channels in mesenteric VSMCs
Table 1.5 Ion transportation of pumps and transporter in VSMCs
Table 1.6 Main functions of intracellular membrane transporter and receptors
Table 3.1. Male parameters of $\mathrm{I}_{\mathrm{Cav2.1}}$
Table 3.2. Female parameters of $\mathrm{I}_{\mathrm{Cav2.1}}$
Table 3.3. Male parameters of $I_{Kv2.1}$
Table 3.4. Female parameters of $I_{Kv2.1}$
Table 3.5. Male parameters of $I_{Kv1.5}$
Table 3.6. Female parameters of $I_{Kv1.5}$
Table 3.7. Parameters of I_{BKCa}
Table 3.8. Parameters of I_{NSC}
Table 3.9. Parameters of leak currents
Table 3.10. Parameters of I_{NaK}
Table 3.11. Parameters of I_{NCX}
Table 3.12. Parameters of I_{PMCA}
Table 3.13. Parameters of J_{SERCA}
Table 3.14. Parameters of J_{RyR}
Table 4.1. Feedback model parameters and initial conditions
Table 4.2. Summary of experimental super-resolution data

List of Abbreviations

MAP	Mean arterial pressure
CO	Cardiac Output
TRP	Total peripheral resistance
VSMCs	Vascular smooth muscle cells
mmHg	Millimeter of mercury
$[Ca]_i$	Intracellular cytosolic calcium concentration
ACE	Angiotensin II converting enzyme inhibitors
ARBs	Angiotensin II receptor blockers
Ca^{2+}	Calcium
Ca_V	Voltage-gated calcium channels
K_V	Voltage-gated potassium channels
µM	Micrometer
WT	Wild type
pF	Picofarads
cm	Centimeters
F	Faraday constant
Cyt	Cytosol
SR	Sarcoplasmic reticulum
Jun	Junctional
V_{cyt}	Volume of cytosol
V_{SR}	Volume of sarcoplasmic reticulum

V_{Jun}	Volume of junctional domain
Na^+	Sodium
K^+	Potassium
Cl^-	Chloride
TRP	Transient receptor potential
I_K	Voltage-gated potassium currents
$[K]_i$	Intracellular potassium concentration
$[Na]_i$	Intracellular sodium concentration
$[Cl]_i$	Intracellular chloride concentration
$[Ca]_{out}$	Extracellular calcium concentration
$[K]_{out}$	Extracellular potassium concentration
$[Na]_{out}$	Extracellular sodium concentration
$[Cl]_{out}$	Extracellular chloride concentration
NSC	Non-selective cation
GPCRs	G-protein coupled receptors
AngII	Angiotensin II
Phe	Phenylephrine
PLC	Phospholipase-C
DAG	Diglycerol
PIP2	Phosphatidylinositol 4,5-bisphosphate
IP_3	1,4,5-trisphosphate
BK, BK_{Ca}	Large-conductance, Ca^{2+}-activated K^+ channels

MLKC	Myosin chain light kinase
MCL	Myosin chain
MCLP	Myosin light chain phosphatase
ODEs	Ordinary differential equations
Q	Capacitance
C_m	Membrane capacitance
V	Voltage
R	Gas constant
T	Temperature
P_o	Open probability
γ_X	Single-channel conductance
z_X	Valence of ion X
GHK	Goldman-Hodgkin-Katz
mol	moles
μM	Micromolar
STOCs	Spontaneous transient outward currents
nM	Nanomolar
pA	Picoamps
G_X	Maximal conductance
$Perm_X$	Permeability of ion X
pF	Picofarads
t	Time

ms	Millisecond
VSM	Vascular smooth muscle
mV	millivolts
$[Ca]_{SR}$	Sarcoplasmic reticulum calcium concentration
$[Ca]_{Jun}$	Junctional calcium concentration
IBTX	Iberiotoxin
THs	transient hyperpolarizations
IBTX	Iberiotoxin
Q_{on}	ON gating charge
ER	Endoplasmic reticulum
GSD	Ground state depletion
I	Current
i	Elementary current
N	Number
P_g	Probability of growth
P_n	Probability of nucleation
P_R	Probability of removal
q	Elementary charges
ScTx1	Stromatoxin
r	Radius
nS	Nanosiemens

Chapter 1: Introduction

1.1 The Cardiovascular System

The cardiovascular system consists of the heart and blood vessels (**Figure 1.1**). The blood vessels allow the blood to flow through an interconnected closed network that carries oxygenated blood from the heart to the tissues and back to the heart. The forward momentum imparted primarily by the pumping of the heart makes the blood flow through the vessels [1].

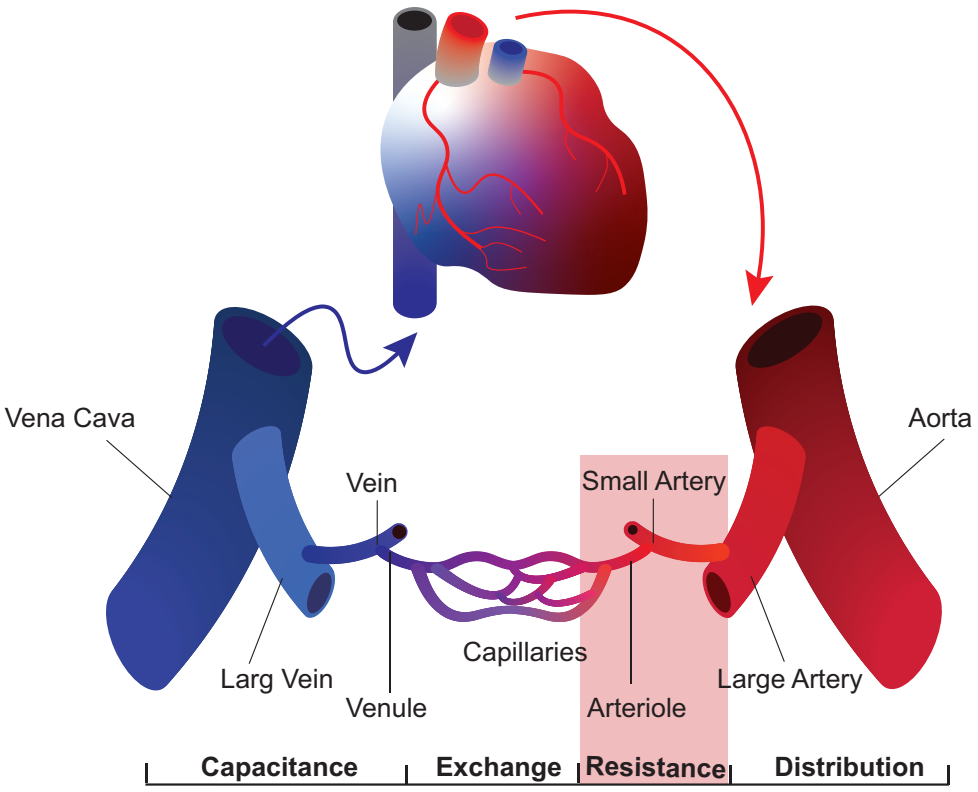

Figure 1.1. Diagram of the cardiovascular system. The illustration shows the heart, the arteries (red), the veins (blue), and the capillaries (purple).

There are three types of blood vessels:

- The arteries, which are also known as resistance blood vessels, distribute blood from the heart to all organs. Arteries can be divided into four subcategories based on their lumen diameter size: The aorta (2.5 cm), large arteries (0.5 cm), small arteries (0.4 cm), and arterioles (30 μm).
- The veins, which are also known as capacitance vessels, carry blood back to the heart. Veins can be divided into four subcategories based on their lumen diameter size: The vena cava (3 cm), large veins (1 cm), small veins (0.5 cm), and venules (20 μm).
- The capillaries, which are the smallest blood vessels with a lumen diameter of 5 μm connect arteries to the veins and are responsible for the exchange of nutrients, oxygen, and waste.

Mean arterial pressure (MAP) is determined by the product of cardiac output (CO) and total peripheral resistance (TPR).

$$MAP = (CO) \times (TPR) \qquad \text{(Eq. 1.1)}$$

The determinants of cardiac output are the heart rate and the left ventricular stroke volume. Total peripheral resistance or the friction generated when blood comes in contact with the vessel walls depends to a minor degree on blood viscosity but to a greater extent upon the diameter, number, and organization of small arteries and arterioles [1]. Small arteries and arterioles are resistance vessels responsible for delivering blood into the capillary beds and provide about 80% of the total resistance to blood flow from different vascular beds [2, 3].

The walls of small resistance arteries and arterioles consist of three structurally distinct layers [2]: First, the tunica intima layer, which is integrated with a single layer of endothelial cells that forms a blood barrier; Second, the tunica media layer, which is composed of one or two layers of smooth muscle cells (a unique and distinctive feature of small vessels and arterioles); Third, the tunica adventitia is composed mostly of collagen bundles, nerve endings, and fibroblasts [2]. Notably, the primary function of the tunica media layer is to control vessel lumen diameter through smooth muscle cell contraction and relaxation processes. Therefore, vascular smooth muscle cells (VSMCs) are key players contributing to the regulation of blood pressure by controlling the diameter of blood vessels and thus controlling total peripheral resistance.

A unique feature of VSMCs is their ability to intrinsically contract and relax in response to changes in intravascular pressure. A decrease in arterial diameter in response to increased intravascular pressure is known as the “myogenic response” or “Bayliss effect” [4, 5]. The steady-state level of contractile activity of VSMCs is controlled by changes in membrane potential and intracellular calcium ($[Ca]_i$) is known as the myogenic tone. The myogenic tone in small arteries and arterioles leads to dynamic changes in vessel diameter, and hence resistance, which keeps blood flow relatively constant over a range of intravascular pressures (~60–120 mmHg). The relationship between the radius of vessels and resistance (resistance $\propto 1/r^4$) has the potential to allow tightly controlled blood flow when needed [6]. These same processes regulate total peripheral resistance to blood flow and consequently mean arterial blood pressure.

The small arteries and arterioles located in the mesenteric vascular bed have been the subject of intensive investigation due to their major contribution to total peripheral resistance. Mesenteric arteries transfer blood from the aorta and distribute it through the gastrointestinal tract receiving about 25% of the body's cardiac output [7]. The pathophysiological progression of cardiovascular disease, such as hypertension has been linked to disruptions or alterations in total peripheral resistance and cardiac output in mesenteric arteries. Therefore, the mechanisms modulating total peripheral resistance have been a primary therapeutic target for hypertension [8]. Therapy goals for hypertension include behavioral (exercise, weight loss, quit smoking) and pharmacological (drugs) interventions.

Hypertension is a multifactorial disease; it affects more than one billion people worldwide and is estimated to account for ~60% of all cases or types of cardiovascular disease [9]. Overall, men are at greater risk for hypertension-related cardiovascular diseases than women [10, 11]. Despite the known sex differences, men and women are given similar treatment for hypertension. As a consequence, treated women achieve blood pressure control at a significantly lower rate (44.8%) compared with men (51.1%) [12]. Calcium channel blockers, Angiotensin II converting enzyme inhibitors (ACE), and Angiotensin II receptor blockers (ARBs) are widely used to decrease total peripheral resistance, and hence decrease blood pressure in hypertensive patients. Interestingly, sex-specific differences in the response to antihypertensives have been reported [13]. For example, while Ca^{2+} channel blockers are more effective in lowering blood pressure in women than in men, men see a larger decrease in blood pressure in response to Angiotensin II

signaling modulators such as ACE inhibitors [13]. The mechanisms underlying these differences are poorly understood.

The necessity of treating hypertension to prevent premature death has led to the urgent need to develop new approaches for *revealing* the mechanisms of male and female hypertension and *predicting* how drugs will alter vascular function in males and females. The work of this dissertation focuses on the development of a mathematical model to describe the electrical activity of a mesenteric vascular smooth muscle cell incorporating sex-specific differences observed in $Ca_V1.2$ and $K_V2.1$ channels. These channels have previously been associated with the remodeling in the pathogenesis of hypertension and differential responses to antihypertensive agents.

1.2 Cell size and structure of mesenteric vascular smooth muscle cells

Vascular smooth muscle cells are spindle-shaped cells, ranging in length from 100 to 800 μM. While VSMCs are very long, they tend to be typically very thin with an average cross-sectional diameter of ~2.5 to 10 μM. One important feature is that, unlike skeletal or cardiac cells, VSMCs are not organized in sarcomeres and do not have transverse tubules (t-tubules). In fact, these cells are known as “smooth” because of the lack of the appearance of striations.

In this dissertation, we used VSMCs found in the mesenteric region of male and female WT mice C57BL/6J. Based on all the cells used in the experiments (N=45), the mean capacitance of the cells was calculated to be 16± 3 pF. Assuming the cells are roughly

cylindrical in shape, the expected radius should be 2.485 μM and a length of 100 μM leading to a surface area of 1.6×10^{-5} cm^2 and a total volume of approximately 1.94×10^{-12} liters. The cell capacitance of excitable membranes is assumed to be 1.0×10^{-6} F/cm^2, with the calculated surface area the estimated total cell capacitance is, therefore, C_m = 16 pF.

Because the total cell volume is roughly 2×10^{-12} liters, it is assumed that 50% of the total cell volume is occupied by organelles. There are three main compartments in VSMCs important to the regulation of membrane potential and calcium signaling (**Figure 1.2**); the cytosol, sarcoplasmic reticulum (SR), and specialized junctional domains formed by the SR and the plasma membrane. The cytosol occupies approximately 50% of total cell volume (V_{cyt} = 1.0×10^{-12} L). The sarcoplasmic reticulum occupies 5% of cell cytosolic volume (V_{SR} = 5.0×10^{-14} L), and the junctional domain volume is approximately 1% of the cytosol volume (V_{Jun} = 0.5×10^{-14} L).

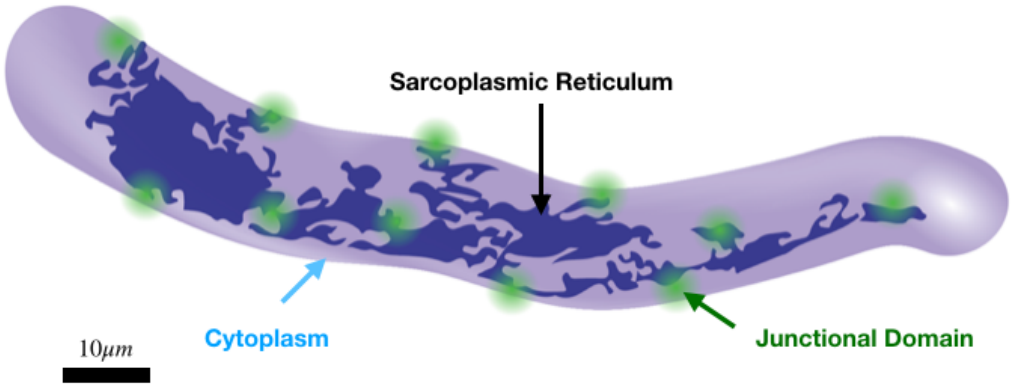

Figure 1.2. Illustration of the three main compartments in vascular smooth muscle cells.

1.3 Ion channels and the electrophysiology of vascular smooth muscle cells

The electrical activity in vascular smooth muscle cells is generated by the flow of sodium (Na^+), potassium (K^+), chloride (Cl^-), and calcium (Ca^{2+}) ions through specialized proteins known as ion channels, pumps, and transporters in the plasma membrane. The movement of ions across the membrane is due to its electrochemical gradient composed of an electrical component and a chemical (concentration) component [14]. For instance, a charge difference across the lipid membrane causes the electrical component while the differential concentration of ions across the membrane is responsible for the chemical component. When the electrical and chemical components are equal in magnitude, the ion is said to be in electrochemical equilibrium. The equilibrium potential of Na^+, K^+, Cl^-, and calcium Ca^{2+} ions in mesenteric VSMCs based on experimental measurements are shown in **Table 1.1**.

Intracellular Concentrations	**Extracellular Concentrations**	**Nernst Potential (E_X)**
$[Ca]_i$= 0.0001 mM	$[Ca]_{out}$= 2.0 mM	E_{Ca}= 126 mV
$[K]_i$ = 140 mM	$[K]_{out}$= 5.0 mM	E_K= -85 mV
$[Na]_i$ = 10mM	$[Na]_{out}$= 130 mM	E_{Na}=65 mV
$[Cl]_i$ = 42 mM	$[Cl]_{out}$= 141 mM	E_{Cl}=-30 mV

Table 1.1. Ionic concentrations of Na^+, K^+, Cl^- and Ca^{2+} in VSMCs and their equilibrium potentials.

Vascular smooth muscle cells found in the mesenteric small arteries and arterioles express a plethora of ion channels in the plasma membrane, including potassium (K^+) channels, calcium (Ca^{2+}) channels, and multiple members of the transient receptor potential (TRP) family of ion channels, pumps, and transporters.

Voltage-gated potassium (K^+) channels. The membrane potential is mostly determined by potassium (K^+) conductances, which are important in the pathway involved in the hyperpolarization of VSMCs. In isolated mesenteric VSMCs, electrophysiological recordings of voltage-gated K^+ currents (I_K) elicited in response to 500ms depolarizations ranging from -50 to +50 mV and K_V selective inhibition suggest that channels in **Table 1.2** are major contributors to I_K [15].

Channel	Full name	Accessory Units	Inhibitors/Agonist
$K_V1.2$	Delayed rectifier K^+ channel	$K_V\beta1$, $K_V\beta2$	4-Aminopyridine
$K_V1.5$	Delayed rectifier K^+ channel	$K_V\beta1$, $K_V\beta2$, $K_V\beta3$	4-Aminopyridine
$K_V2.1$	Delayed rectifier K^+ channel	$K_V9.3$	Stroma-toxin 1
$K_{Ca}1.1/BK_{Ca}$	Large-conductance Ca^{2+}-activated K^+ channel	β1	Iberiotoxin, Charybdotoxin

Table 1.2 Potassium channels in mesenteric VSMCs.

Voltage-gated calcium (Ca^{2+}) channels. In mesenteric VSMCs, two voltage-gated Ca^{2+} channels have been identified: Ca_V1 (L-type, dihydropyridine sensitive) and Ca_V3 (T-type, dihydropyridine insensitive) channels [16]. However, studies have highlighted the essential role of L-type $Ca_V1.2$ Ca^{2+} channels in maintaining arterial tone [17-19]. Voltage-gated L-type calcium $Ca_V1.2$ channels are critical in determining cytosolic concentration ($[Ca^{2+}]_i$) in vascular mesenteric smooth muscle cells and are the predominant pathway for Ca^{2+} entry. Upon depolarization in the range of -45 to -30 mV, the overlap of steady-state activation and inactivation forms a “window” current resulting in the activation of a small number of $Ca_V1.2$ channels that can supply the steady Ca^{2+}

influx needed to support a maintained constricted state in small arteries and arterioles [20, 21]. **Table 1.3** describes the main features of $Ca_V1.2$ channels such as accessory subunits and common $Ca_V1.2$ channel blockers.

Channel	Full name	Accessory Units	Inhibitors/Agonist
$Ca_V1.2$	L-type $Ca_V1.2$ channel	β2, β3, α_2 δ_1	Nifedipine, Nimodipine, Diltiazem, Verapamil

Table 1.3. Main features of the voltage-gated L-type $Ca_V1.2$ channels.

Transient receptor potential (TRP) channels. In VSMCs, the resting membrane potential is less negative than the equilibrium potential of potassium (E_K = -84 mV), suggesting active participation of inward currents regulated by the sodium conductance [22]. Before the discovery of TRP channels, the depolarizing inward currents measured in different VSMCs were thought to be generated by background non-selective cation (NSC) channels. Although the specific channels generating depolarizing inward currents have not been unequivocally identified, recent studies have provided possible ion channel candidates that belong to the extensive family of TRP channels. Studies in cerebral VSMCs suggest that TRPM4 channels are the main contributors to the non-selective cation currents [23]. Other potential contributors include the TRPC6 and TRPV4 channels, but they require the activation of G-protein coupled receptors (GPCRs) signaling pathways [16, 24-26]. **Table 1.4** describes the ion selectivity and physiological activation of potential ion channel candidates that contribute to depolarizing inward currents.

Channel	Full name	Ion selectivity	Physiological activation
TRPC6	Transient Receptor Potential Cation Channel Subfamily C Member 6	Ca^{2+}, Na^{+}	Diacylglycerol (DAG), stretch
TRPM4	Transient Receptor Potential Cation Channel Subfamily M Member 4	Na^{+}	Ca^{2+}
TRPV4	Transient Receptor Potential Cation Channel Subfamily V Member 4	Ca^{2+}, Na^{+}	Mechanical stimuli, heat, and G_q signaling
TRPP1	Transient Receptor Potential Cation Channel Polycystin	Ca^{2+}, Na^{+}	Mechanosensation

Table 1.4. Transient receptor potential (TRP) family of ion channels in mesenteric VSMCs

Pumps and transporters. In VSMCs, pumps and transporters are essential for the regulation of intracellular Na^{+}, K^{+}, and Ca^{2+} ionic concentrations. In mesenteric guinea-pig smooth VSMCs, the Na-K pump was shown to be important not only in the maintenance of the Na^{+} and K^{+} ionic concentrations but also in the regulation of membrane potential and therefore an important contributor to the vascular tone [27]. The Na^{+}-Ca^{2+} exchanger (NCX) normally mediates Ca^{2+} entry in tonically constricted small arteries [28]. The plasma membrane Ca^{2+}-ATPase removes Ca^{2+} from the cytosol to the extracellular space, and it is essential to arterial myocytes' survival and function. **Table 1.5** summarizes the ion transportation by pumps and transporters.

Pump/Transporter	Full name	Ion transportation
Na-K Pump	Sodium/potassium pump current	Forward mode results in the expulsion of $3Na^+$ ions and the uptake of $2K^+$ ions.
NCX	Sodium/calcium exchanger	In forward mode, the NCX pump transports Ca^{2+} outside the cell. In reverse mode, the NCX takes up extracellular Ca^{2+}.
PMCA	Plasma membrane Ca^{2+} ATPase	Expels Ca^{2+} from the cytosol.

Table 1.5. Ion transportation of pumps and transporter in VSMCs.

Intracellular membrane transporters and receptors. In the sarcoplasmic reticulum (SR), ryanodine receptors (RyRs) and SR Ca^{2+}-ATPase (SERCA) generate intracellular currents important in Ca^{2+} signaling. A recent study identified that the ryanodine receptor isoform 2 (RyR2) plays a dominant role in local and global Ca^{2+} release in systemic arteries [29]. RyR2 mediates Ca^{2+} release in the form of sparks generated by a single cluster of RyRs in a single junctional domain. SERCA plays an important role in calcium signaling by maintaining low intracellular Ca^{2+} in the cytoplasm. **Table 1.6** describes the main function of intracellular membrane RyRs and SERCA.

Receptor/Transporter	Full name	Main function
RyR2	Ryanodine receptor type 2	Responsible for Ca^{2+} sparks in the junctional domain.
SERCA	SR Ca^{2+}-ATPase	The main pathway for uptake Ca into the sarcoplasmic reticulum.

Table 1.6. Main functions of intracellular membrane transporter and receptors.

1.4 Excitation-Contraction coupling in vascular smooth muscle cells

In mesenteric smooth muscle, an increase in $[Ca]_i$, which leads to contraction and the onset of myogenic tone, can occur through voltage-dependent electro-mechanical coupling and voltage-independent pharmaco-mechanical coupling mechanisms. Both processes increase $[Ca]_i$ leading to the activation of contractile proteins myosin and actin. Smooth muscle relaxation occurs through a direct negative feedback mechanism that opposes the voltage-dependent electro-mechanical coupling. In addition, smooth muscle relaxation is promoted by the activation of signaling pathways. A detailed diagram of the excitation-contraction coupling in VSMCs is shown in **Figure 1.3**.

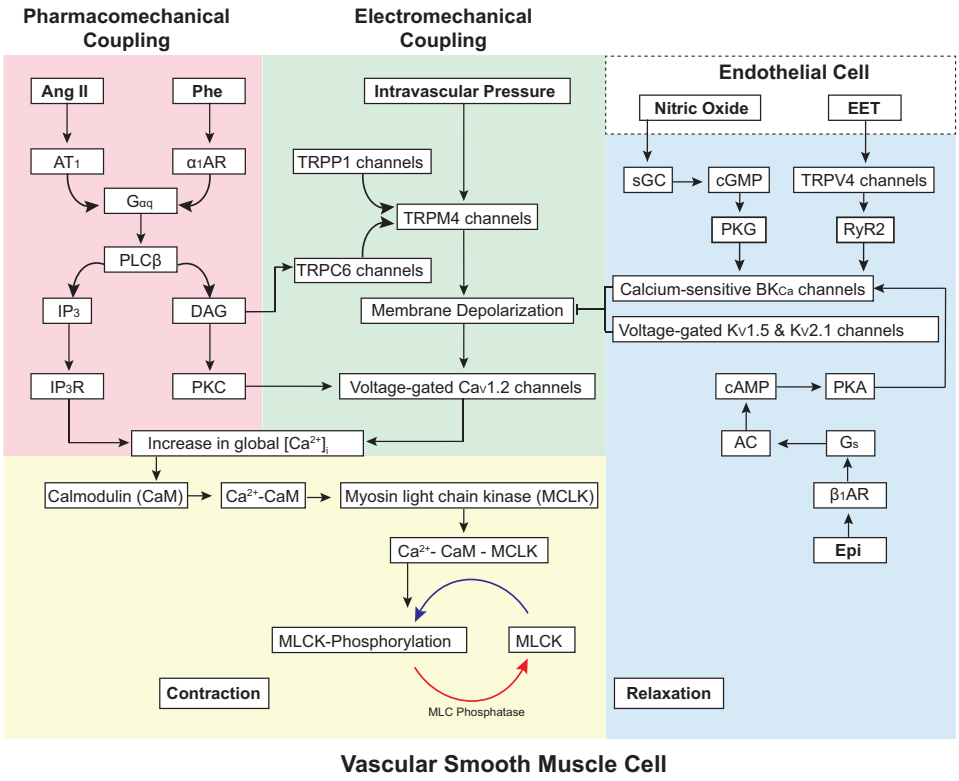

Figure 1.3. **Excitation-contraction coupling in VSMCs**. Diagram illustrating the electro-mechanical (green) and the pharmaco-mechanical coupling (pink), the negative feedback mechanism (blue), and the actin-myosin cross-bridge cycling (yellow).

The electromechanical coupling (**Figure1.3**, *green background*) is initiated by membrane stretch and activates Na^+-permeable canonical TRPC6, melastatin-type TRPM4, and TRPP1 (PKD2) channels [30-32]. The opening of these channels depolarizes arterial smooth muscle cells, thereby activating voltage-gated, dihydropyridine-sensitive L-type $Ca_V1.2$ Ca^{2+} channels. Ca^{2+} entry via a single or small cluster of $Ca_V1.2$ channels produces a local increase in intracellular free Ca^{2+} ($[Ca^{2+}]_i$) called a "$Ca_V1.2$ sparklet" [17-19]. Activation of multiple $Ca_V1.2$ sparklets produces a global increase in $[Ca^{2+}]_i$ that activates myosin light chain kinase, which initiates actin-myosin cross-bridge cycling and thus contraction.

During pharmaco-mechanical coupling (**Figure1.3**, *pink background*) [33], activation of G_q-protein-coupled receptors (G_qPCRs) by vasoactive agents (such as angiotensin II (AngII) or phenylephrine (Phe)) leads to the activation of the enzyme phospholipase-C (PLC), which cleaves phosphatidylinositol 4,5-bisphosphate (PIP2) to form two signaling molecules diglycerol (DAG) and 1,4,5-trisphosphate (IP_3). This leads to increases in $[Ca^{2+}]_i$ through activation of sarcoplasmic reticulum IP_3 receptors or protein-kinase C-dependent Ca^{2+}-permeable sarcolemma channels [6]. Consequently, the global increase in $[Ca^{2+}]_i$ activates myosin light chain kinase, which initiates actin-myosin cross-bridge cycling and contraction.

Negative feedback regulation (**Figure1.3**, *blue background*) of Ca^{2+} influx via $Ca_V1.2$ channels occurs through the activation of large-conductance, Ca^{2+}-activated K^+ (BK_{Ca}) channels, as well as voltage-dependent $K_V2.1$ and $K_V1.2/1.5$ K^+ channels [34-36]. BK_{Ca}

channels are organized into clusters along the sarcolemma [37] or arterial myocytes and activated by Ca^{2+} sparks, resulting from the simultaneous opening of ryanodine receptors type 2 (RyR2) located in the junctional domain (Jun). Because the input resistance of arterial myocytes is high (about 10 GΩ) [38, 39], the relatively small currents produced by the activation of a single cluster of 6-12 BK_{Ca} channels transiently hyperpolarize the membrane potential activation of smooth muscle cells by 10-30 mV to near the Nernst equilibrium potential for K^+. Acute pharmacological blockade of BK_{Ca}, $K_V1.2$, $K_V1.5$, or $K_V2.1$ channels eliminates a substantial component of delayed rectifier current in arterial myocytes and causes constriction in rat cerebral artery smooth muscle [40-43].

For contraction to occur, the actin-myosin cross-bridge cycling (**Figure1.3**, *yellow background*) is initiated by free calcium Ca^{2+} in the cytosol binding the calcium buffer calmodulin. The Ca^{2+} -bound calmodulin activates myosin chain light kinase (MLKC), which leads to the phosphorylation of the regulatory myosin chain (MCL) enabling myosin heads to form cross-bridges with actin. The cross-bridge cycling leads to cell shortening and force development [44]. However, phosphorylated MCL can be dephosphorylated by the enzyme myosin light chain phosphatase (MCLP). Therefore, relaxation can occur if $[Ca]_i$ decreases, MLCK activity decreases, and/or if $[Ca]_i$ enables MLC dephosphorylation to dominate.

Chapter 2: Mathematical modeling

"*It can be argued that of all biological sciences, physiology is the one in which mathematics has played the greatest role* "James Keener and James Sneyd

2.1 Biophysical properties of the excitable cell membranes

All living organisms are composed of basic building blocks called cells. Cells are complex self-sustained units that produce their own energy to produce signals to contract, relax, move, excrete, reproduce, and carry out multiple tasks. The fascinating thing is that the complex network of interacting chemicals and substrates within cells obeys basic physical principles [45].

In 1952, Alan Hodgkin and Andrew Huxley introduced the mathematical framework on which modern biophysical modeling studies of excitable cells are based. In their groundbreaking work, Hodgkin and Huxley developed a conductance-based model defined by a set of ordinary differential equations (ODEs) describing the ionic basis of the action potential in neurons [46]. The Hodgkin and Huxley model was developed using empirical data, thus the fusion of model and experiment provided a new approach to understanding and teasing out the mechanisms underlying physiological phenomena in excitable cells using mathematical equations.

The general assumption is that the cell membrane, ion channels, and the concentration gradient of different ions are analogous to the basic components of a resistor-capacitor (RC) circuit [45].

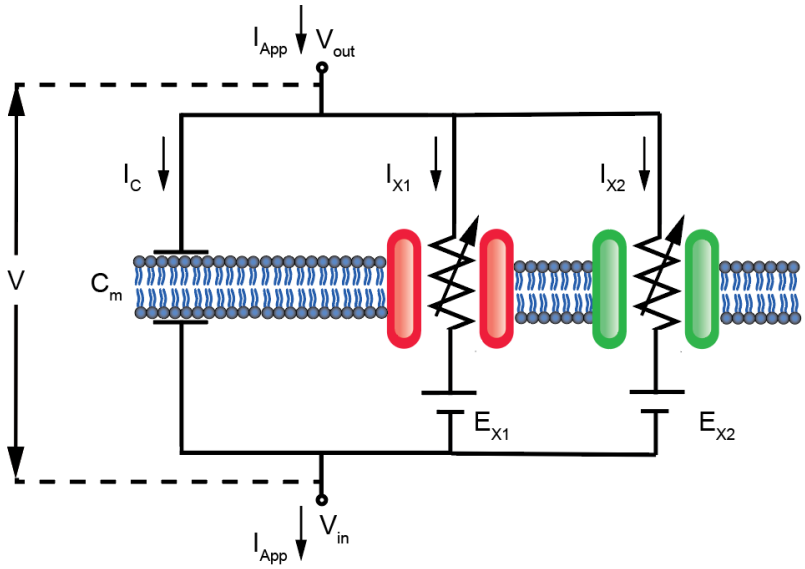

Figure 2.1. The cell membrane as a circuit. Diagram illustrating the RC circuit (Capacitor, resistor, batteries) and its corresponding cell components (cell membrane (blue), ion channels (red, green), electrochemical driving forces).

a) The membrane lipid bilayer is analogous to a two-plate capacitor that accumulates or dissipates ionic charge as the electrical potential across the two plates changes.
b) The ionic permeabilities of the membrane are analogous to resistors in the electric circuit.
c) The electrochemical driving force of ionic currents is analogous to batteries in the electrical circuit.

The capacitive and ionic currents of the membrane are organized in parallel. Applying the mathematical description of an RC circuit, the charge across the capacitance (Q) is proportional to the voltage potential required to hold that charge (V) and the capacitance of an insulator (C_m).

$Q = C_m V$ (Eq. 2.1)

Assuming that C_m is constant, the capacitance current can be defined as

$$\frac{dQ}{dt} = \frac{dV}{dt} C_m \qquad \text{(Eq. 2.2)}$$

$$I_C = \frac{dV}{dt} C_m \qquad \text{(Eq. 2.3)}$$

Because the ion channels are analogous to resistors and the voltage drops across the channels in the circuit are ΔV_{X1} and ΔV_{X2}, using Ohm's law the ionic currents shown in **Figure 2.1** can be defined as

$$I_{X1} = \left(\frac{1}{R_{X1}}\right) \Delta V_{X1} = \frac{1}{R_{X1}} (V - E_{X1}) \qquad \text{(Eq. 2.4)}$$

$$I_{X2} = \left(\frac{1}{R_{X2}}\right) \Delta V_{X2} = \frac{1}{R_{X2}} (V - E_{X2}) \qquad \text{(Eq. 2.5)}$$

Where E_X is the reversal potential of ion channel X. Define as

$$E_X = \frac{RT}{z_X F} ln \left(\frac{[X]_{out}}{[X]_i}\right) \qquad \text{(Eq. 2.6)}$$

Where R is the gas constant, F is the Faraday constant, T is the absolute temperature in Kelvin and z_X is the valence of ion X. $[X]_i$ and $[X]_{out}$ is the concentration of ion X inside and outside the cell, respectively.

Noting that the ionic conductances are $G_X = \frac{1}{R_X}$, the ionic current for a specific ion X can be described as

$$I_X = G_X * (V - E_X) \qquad \text{(Eq. 2.7)}$$

Applying Kirchhoff's current law, the capacitance current (I_C) and the ionic currents (I_{X1} and I_{X2}) must add up to the externally applied current (I_{App}):

$$I_{App} = I_C + I_{X1} + I_{X2} \qquad \text{(Eq. 2.8)}$$

Therefore,

$$C_m \frac{dV}{dt} = -G_{X1}(V - E_{X1}) - G_{X2}(V - E_{X2}) + I_{App} \qquad \text{(Eq. 2.9)}$$

Because all ionic currents run in parallel, the equation Eq. 2.9 can be expanded to a N number of ionic currents.

$$\frac{dV}{dt} = -\frac{1}{C_m}\left(\sum_{i=1}^{N} G_i(V - E_i) + I_{App}\right) \qquad \text{(Eq. 2.10)}$$

2.2 Mathematical modeling of ionic currents

In the simplified mathematical description (Eq. 2.7), the ionic current across the cell membrane is assumed to be a linear function of the membrane potential [14, 45]. However, the opening and closing of ion channels in response to changes in membrane potential is fundamental in describing ionic currents. Therefore, the proportion of open channels in a population of N channels defined as P_o must be included,

$$I_X = G_X * \mathrm{P_O} * (V - E_X) \qquad \text{(Eq. 2.11)}$$

where G_X is the specific conductance or maximal conductance and has units of Siemens/cm^2. In addition, $G_X = N*\gamma_X$ and γ_X is the single-channel conductance in pico-siemens (pS) and I_X has units of Amperes/cm^2.

Eq. 2.10 assumes that each contributing ionic current describing the movement of specific ions across the cell membrane follows Ohm's law. However, this is not always the case. An alternative mathematical equation is the Goldman-Hodgkin-Katz (GHK) formalism in which the current is a non-linear function of voltage and linear in the ionic concentration [45]. Similarly, P_o is included,

$$I_X = P_0 * N * Perm_X * \frac{z_X^2 F^2}{RT} * V * \left[\frac{[X]_i * e^{\frac{z_X FV}{RT}} - [X]_{out}}{e^{\frac{z_X FV}{RT}} - 1}\right] \qquad \text{(Eq. 2.12)}$$

Where $Perm_X$ is the permeability of ion channel with units cm^3/s and N is the number of channels.

The two most common ionic current formulations (Eq. 2.11 and Eq. 2.12) are used in theoretical models of the cellular electrical activity [45]. For example, for voltage-gated Ca^{2+} currents, the GHK equation best describes the experimental observations because of the 10,000-fold Ca^{2+} concentration gradient and divalent change [47]. In contrast, voltage-gated Na^{+} and K^{+} currents are generally described using either the ohmic ion current formulation or the GHK current formulation based on the linear or non-linear voltage behavior observed in the current-voltage (I-V) relationships.

2.3 Mathematical modeling of ion channel voltage-dependent gating

To complete the mathematical framework, a description of how the ion channels open and close is needed. An ion channel fluctuates between multiple conformational states (e.g., open, close, and inactivated). The open probability term (P_o) in equations (Eq. 2.11 & 2.12) can be viewed as the probability that any given channel is open or the proportion of open channels in a large population of N channels [45, 47]. In the traditional Hodgkin-Huxley model approach, the ion channel gating is determined by a set of subunit gates, which are given a functional definition and represent the aggregated fraction of open subunits. The mathematical description of the subunit gate does not always represent a realistic structural model of the ion channels. However, as Hodgkin and Huxley showed such approach is sufficient if one is interested only in the current-carrying capacity of the channel [14].

In the Hodgkin-Huxley gating model approach, each subunit gate is independent of one another, and the transition of each subunit gate is given by a simple two-state kinetic scheme as shown in **Figure 2.2**.

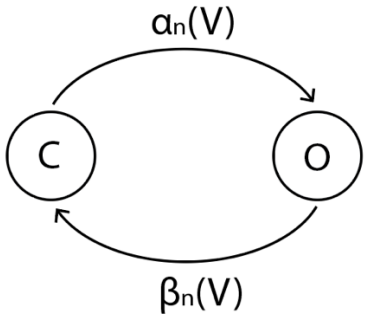

Figure 2.2. Diagram of a two-state kinetic scheme of a subunit gate.

For the subunit gate (n), the transition rate α_n from close (C) to open (O) and the transition rate β_n open (O) to close (C) are voltage dependent. The master equation that describes the time evolution of the two-state kinetic scheme is then

$$\frac{dP_O}{dt} = \alpha_n(V)P_C - \beta_n(V)P_O \quad \text{(Eq. 2.13)}$$

$$\frac{dP_C}{dt} = \beta_n(V)P_O - \alpha_n(V)P_C \quad \text{(Eq. 2.14)}$$

Noting that $P_C = 1 - P_O$ and defining $n = P_O$, Eq. 2.13 becomes

$$\frac{dn}{dt} = \alpha_n(V)(1-n) - \beta_n(V)n \qquad \text{(Eq. 2.15)}$$

Dividing equation 2.15 by $\alpha_n(V)+ \beta_n(V)$, one obtains another useful form to fit the gating models to experimental data [14].

$$\frac{dn}{dt} = \frac{(n_\infty(V)-n)}{\tau_n(V)} \qquad \text{(Eq. 2.16)}$$

where

$$\tau_n(V) = \frac{1}{\alpha_n(V)+\beta_n(V)} \qquad \text{(Eq. 2.17)}$$

and

$$n_\infty(V) = \frac{\alpha_n(V)}{\alpha_n(V)+\beta_n(V)} \qquad \text{(Eq. 2.18)}$$

It is important to note that the open probability of an ion channel often is described as an aggregated fraction of multiple open independent subunits. For instance, in the Hodgkin-Huxley model, the activation process of potassium channels is described by a fourth-order process, therefore $P_O = n^4$. Whereas the sodium channel gating is described by a third-order activation process and a first-order inactivation process, therefore $P_O = m^3h$.

2.4 Computational methods

2.4.1 Optimization of ionic currents

Here, the open probability P_o of each voltage-dependent gating variable "n" will be defined by opening- and closing-rate voltage-dependent functions α_n and β_n respectively and will be modeled by simple exponentials of the form:

$$\alpha_n(V) = x_1 e^{\left(\frac{V}{x_2}\right)} \qquad \text{(Eq. 2.19)}$$

$$\beta_n(V) = x_3 e^{\left(\frac{V}{x_4}\right)} \qquad \text{(Eq. 2.20)}$$

$$\tau_n(V) = \frac{1}{\alpha_n(V)+\beta_n(V)} + x_5 \qquad \text{(Eq. 2.21)}$$

The steady-state availability will remain the same as the formulation in Eq. 2.16 and the time constant values will follow a modified version formulation by accommodating an extra parameter x_5 (Eq. 2.21). (x_1, x_2, x_3, x_4, x_5) are parameters to be optimized using experimental data. We will use the parameter optimization employed by Kernik et al. 2019, which minimizes the error between model and experimental data using the Nelder–Mead minimization of the error function. Random small perturbations (<10%) were applied to find local minima, to improve data fit. The parameter fit with the minimal error function value after 1000 to 10000 perturbations was used as the optimal model fit to the data [48].

2.4.2 Numerical integration

Forward Euler method**.** Euler's method is the basic explicit method for solving numerical integration problems of ordinary differential equations. Based on the simplicity of our equations, forward Euler's method is the first method of choice as simulations are not computationally expensive.

Considering Eq. 2.16, numerical implementation using the forward Euler method is given by

$$n(t + \Delta t) = n(t) + \left(\frac{n_\infty(V(t)) - n(t)}{\tau_n(V(t))}\right)\Delta t \qquad \text{(Eq. 2.22)}$$

where Δt is the time-step.

2.4.3 Noise

VSMCs operate at a low voltage regime under conditions of high resistance membrane where the opening of a small number of channels accounts for the excitability and calcium signaling. Due to the nature of the stochastic activity of ion channels, local fluctuations in the function of ion channels provide a source of noise to the excitability of VSMCs. To model ion channels noise two methods are presented.

Current noise. The first method to incorporate noise into the Hodgkin-Huxley-like systems is to add a fluctuating current term ξ(t) to the membrane potential (dV/dt) equation, as shown in Eq. 2.23. Here it is assumed ξ(t) is only a function of time. In addition, ξ(t) is Gaussian white noise and it is meant to represent the combined effect of the stochastic activity of ion channels on the voltage dynamics of the cell [49].

$$\frac{dV}{dt} = -\frac{I_{total}(V)}{C_m} + \sigma\,\xi(t) \qquad \text{(Eq. 2.23)}$$

Eq. 2.23 can be implemented using the Euler-Maruyama method as follows.

$$V(t+\Delta t) = V(t) - \frac{I(V(t))}{C_m}\Delta t + \sigma * \text{randN} * \sqrt{\Delta t} \qquad \text{(Eq. 2.24)}$$

Where randN is a random number from a normal distribution (N(0,1)) with mean 0 and variance 1. Δt is the time step and σ is the "diffusion coefficient", which represents the amplitude of the noise.

Subunit noise. The second method is to add noise to the subunit gate differential equation (Eq. 2.13) [50]. The Euler-Maruyama method approximates the numerical solution of a stochastic differential equation. It is a generalization of the first-order Euler method for ordinary differential equations

$$\frac{dn}{dt} = \alpha(1-n) - \beta n + \sigma_n \xi(t), \quad n(0) = n_0 \qquad \text{(Eq. 2.25)}$$

$$\sigma_n = \sqrt{\frac{\alpha(1-n)+\beta n}{N}} = \sqrt{\frac{1}{N}\frac{n+n_\infty - 2n*n\infty}{\tau_n}} \qquad \text{(Eq. 2.26)}$$

$$\frac{dn}{dt} = \frac{n_\infty - n}{\tau_n} + \sigma_n \xi(t), \quad n(0) = n_0 \qquad \text{(Eq. 2.27)}$$

And it is implemented using the forward Euler method as follows;

$$n(t+\Delta t) = n\,(t) + \left(\frac{n_\infty(V(t)) - n(t)}{\tau_n(V(t))}\right)\Delta t + \sqrt{\frac{\Delta t}{N}\frac{n(t) + n_\infty(V(t)) - 2n(t)n_\infty(V(t)}{\tau_n(V(t))}} * \text{randN}$$

(Eq. 2.28)

Where randN is a random number from a normal distribution (N(0,1)) with mean 0 and variance 1. Because the open probability of the ion channels is often described by the aggregated fraction of multiple open subunits the aggregated noise may not represent the stochastic noise of ion channel opening. However, if a channel is gated by a single subunit, Eq. 2.25 is appropriate [50].

2.5 General approach and hypotheses

The approach that we will follow is similar to what has been done in the field of cardiac modeling. Owing to the maturity of the field, computational models of cardiac electrophysiology have shown a potential for clinical applications in all areas of cardiovascular medicine, including drug safety evaluation, disease diagnosis, and personalized therapy [51, 52]. Often cardiac electrophysiological models are multi-scale endeavoring to simulate the electrophysiology of cardiac myocytes and tissue [52]. A multi-scale approach often contains as a fundamental unit a cellular model, which is typically set by ordinary differential equations (ODEs) that predict membrane potential and Ca^{2+} signaling. Hence, in this dissertation, I developed male and female computational models of vascular smooth muscle cell electrophysiology that will serve as a fundamental building block to allow the development of tissue and organ scale models of vascular vessels.

<u>Aim 1:</u> To develop male and female computational models of vascular smooth muscle cell electrophysiology: Our goal is to establish fundamental sex-specific mechanisms controlling electrophysiological response and intracellular calcium concentration ($[Ca^{2+}]_i$) in unpressurized single vascular smooth muscle (VSM) cells.

Driving Hypothesis for Aim 1: Differences in the amplitude and voltage dependencies of L-type $Ca_V1.2$ currents between males and females cause higher Ca^{2+} influx, $[Ca^{2+}]_i$, in female than in male mesenteric smooth muscle cells.

<u>Aim 2:</u> To develop a feedback computational model by which channel clusters are formed and regulated in size in the plasma membrane of vascular smooth muscle cells and test the hypothesis that ion channel clustering is the consequence of a stochastic self-assembly process.

Driving Hypothesis for Aim 2: Analyses of the size distributions of the channel clusters measured in arterial smooth muscle as well as heterologous cells are described by exponential functions, indicative of a Poisson process, therefore channel cluster organization is the consequence of a stochastic self-assembly process.

Chapter 3: The Hernandez-Hernandez model of male and female vascular smooth muscle cell Ca^{2+} signaling and electrophysiology

3.1 Abstract

The smooth muscle cells that line the walls of small resistance arteries and arterioles have been the subject of investigation for decades due to their important role in regulating blood flow and blood pressure. A substantial body of published experimental data has allowed for the formulation of several *in silico* models of vascular smooth muscle cells. The models have revealed mechanisms of control of the membrane potential and $[Ca^{2+}]_i$ during the development of myogenic tone in arterial blood vessels. One limitation of the existing models is that they are based on data from male animals only. Here, we describe a new model of an isolated mesenteric smooth muscle cell incorporating new electrophysiological and Ca^{2+} signaling data suggesting key sex-specific differences in male and female arterial myocytes. The model successfully describes the electrical activity of membrane potential, as well as local and global intracellular Ca^{2+} cycling observed in male and female myocytes. Contrary to established models suggesting that $K_V1.5$ channels are the most prominent K_V channels regulating membrane potential, our model predicts that $K_V2.1$ channels play an unexpected primary role in the control of membrane potential in female myocytes but not in male myocytes. Furthermore, our model predicts that clinically used antihypertensive $Ca_V1.2$ channels blockers cause larger reductions in $Ca_V1.2$ currents in female than in male arterial myocytes. The Hernandez-Hernandez model highlights the importance of sex-specific differences in $Ca_V1.2$ and $K_V2.1$ channels. These channels have previously been associated with the

remodeling in the pathogenesis of hypertension, and we demonstrate differential responses to antihypertensive agents.

3.2 Introduction

A recent study by O'Dwyer *et al*. [15] suggested that $K_V2.1$ channels have dual conducting and structural roles in arterial smooth muscle. In arterial myocytes, $K_V2.1$ plays both conductive and structural roles with opposing functional consequences. Conductive $K_V2.1$ channels oppose vasoconstriction by inducing membrane hyperpolarization. Paradoxically, by promoting the structural clustering of the $Ca_V1.2$ channel, $K_V2.1$ enhances Ca^{2+} influx and induces vasoconstriction. Importantly, O'Dwyer *et al*. found that $K_V2.1$ protein is expressed to a larger extent in female than in male arterial smooth muscle. Because experiments were performed using a global constitutive $K_V2.1$ knockout mouse, there is a possibility of long-term and systemic compensatory mechanisms. Therefore, in our study, using mathematical modeling we tease out the contributions of $K_V2.1$ channels to voltage-gated K^+ currents (I_K) in male and female myocytes.

Previous mathematical models have attempted to describe membrane potential and calcium signaling in single VSMCs [53-56]. Such models were generated to describe the membrane potential and Ca^{2+} signaling in vascular smooth muscle cells have been focused on describing the activation of G-protein-coupled receptors (GPCRs) by endogenous or pharmacological vasoactive agents activating inositol 1,4,5-trisphosphate (IP_3) and ryanodine receptors (RyRs) preceding the initiation of calcium waves. By doing so, these mathematical models have provided insights into the contraction activation by

agonists and the behavior of vasomotion. In a major step forward, equipped with new cell structure data and electrophysiology experimental data, Karlin [57] proposed a new model suggesting that the essential behavior of membrane potential and Ca^{2+} signaling arises from intracellular microdomains found in the structure of arterial myocyte. Despite the efforts, a major limitation of all previous models is that they are based entirely on data from male animals. Furthermore, they do not take into consideration the role of $K_V2.1$ channels in the regulation of smooth muscle cell membrane potential.

Here, we describe a new model, called the Hernandez-Hernandez model of the mesenteric smooth muscle myocyte incorporating new electrophysiological and Ca^{2+} signaling data suggesting key sex-specific differences in male and female arterial myocytes. The model simulates the membrane currents and their impact on membrane potential, as well as local and global $[Ca^{2+}]_i$ signaling in male and female myocytes. The Hernandez-Hernandez model predicts that $K_V2.1$ channels play a critical, unexpectedly large role in the control of membrane potential in female myocytes compared to male myocytes. Importantly, our model predicts that clinically used antihypertensive $Ca_V1.2$ channels blockers cause larger reductions in $Ca_V1.2$ currents in female than in male arterial myocytes. The Hernandez-Hernandez model demonstrates the importance of sex-specific differences in $Ca_V1.2$ and $K_V2.1$ channels, which are often associated with remodeling, leading to the pathogenesis of hypertension and differential responses to antihypertensive agents.

3.3 Experimental methods

3.3.1. Animals

Four-eight-week-old male and female C57BL/6J (The Jackson Laboratory, Sacramento, CA) were used in this study. Animals were euthanized with a single lethal dose of sodium pentobarbital (250 mg/kg) intraperitoneally. All experiments were conducted in accordance with the University of California Institutional Animal Care and Use Committee guidelines.

3.3.2. Isolation of arterial myocytes from systemic resistance arterioles

Third and fourth-order mesenteric arteries were carefully cleaned of surrounding adipose and connective tissues, dissected, and held in ice-cold dissecting solution (Mg^{2+}-PSS; 5 mM KCl, 140 mM NaCl, 2mM $MgCl_2$, 10 mM glucose, and 10 mM HEPES adjusted to pH 7.4 with NaOH). Arteries were first placed in dissecting solution supplemented with 1.23 mg/ml papain (Worthington Biochemical, Lakewood, NJ) and 1 mg/ml DTT for 14 minutes at 37˚C. This was followed by a second 5-minute incubation in dissecting solution supplemented with 1.6 mg/ml collagenase F (Sigma-Aldrich, St. Louis, MO), 0.5 mg/ml elastase (Worthington Biochemical, Lakewood, NJ), and 1 mg/ml trypsin inhibitor from *Glycine max* (Sigma-Aldrich, St. Louis, MO) at 37˚C. Arteries were rinsed three times with dissection solution and single cells were obtained by gentle trituration with a wide-bore glass pipette. Myocytes were maintained at 4˚C in dissecting solution until used.

3.3.3. Patch-clamp electrophysiology

All electrophysiological recordings were acquired at room temperature (22–25°C) with an Axopatch 200B amplifier and Digidata 1440 digitizer (Molecular Devices, Sunnyvale, CA). Borosilicate patch pipettes were pulled and polished to resistances of 3-6 MΩ for all experiments using a micropipette puller (model P-97, Sutter Instruments, Novato, CA). Freshly dissociated arterial smooth muscle cells were kept in ice-cold Mg^{2+}-PSS before being recorded.

Voltage-gated Ca^{2+} currents ($I_{Cav1.2}$) were measured using conventional whole-cell voltage-clamp sampled at a frequency of 50 kHz and low-pass filtered at 2 kHz. Arterial myocytes were continuously perfused with 115 mM NaCl,10 mM TEA-Cl, 0.5 mM $MgCl_2$, 5.5 mM glucose, 5 mM CsCl, 20 mM $CaCl_2$, and 10 mM HEPES, adjusted to pH 7.4 with CsOH. Micropipettes were filled with an internal solution containing 20 mM CsCl, 87 mM Aspartic acid, 1 mM MgCl2, 10 mM HEPES, 5 mM MgATP, and 10 mM EGTA adjusted to pH 7.2 using CsOH. Current-voltage relationships were obtained by exposing cells to a series of 300 ms depolarizing pulses from a holding potential of -70 mV to test potentials ranging from -70 to +60 mV. A voltage error of 9.4 mV due to the liquid junction potential of the recording solutions was corrected offline. Voltage dependence of Ca^{2+} channel activation (G/G_{max}) was obtained from the resultant currents by converting them to conductance via the equation $G = I_{Ca}/(\text{test potential} - \text{reversal potential of } I_{Ca})$; normalized G/G_{max} was plotted as a function of test potential. Time constants for activation and inactivation of I_{Ca} were fitted with a single exponential function.

I_{Kv} recordings were performed in the whole-cell configuration with myocytes exposed to an external solution containing 130 mM NaCl, 5 mM KCl, 3 mM $MgCl_2$, 10 mM Glucose, and 10 mM HEPES adjusted to 7.4 using NaOH. The internal pipette solution constituted of 87 mM K-Aspartate, 20 mM KCl, 1 mM $CaCl_2$, 1 mM $MgCl_2$, 5 mM MgATP, 10 mM EGTA, and 10 mM HEPES adjusted to 7.2 by KOH. A resultant liquid junction potential of 12.7 mV from these solutions was corrected offline. To obtain current-voltage relationships cells were subjected to a series of 500 ms test pulses increasing from -70 to +70 mV. To isolate the different K+ channels attributed to overall I_K, cells were first bathed in external I_K solution, subsequently exposed to 100 nM Iberiotoxin (Alomone, Jerusalem, Israel) to eliminate any BK_{Ca} channel activity and finally immersed in an external solution containing both 100 nM Iberiotoxin and 100 nM Stromatoxin (Alomone, Jerusalem, Israel) to remove both BK_{Ca} and Kv1 activity. Ionic current was converted to conductance via the equation $G = I(V-E_K)$. E_K was calculated to be -78 mV based on bath and pipette solutions. Activation time constants for Kv2.1 currents were fitted with a single exponential function.

BK_{ca}-mediated spontaneous transient outward currents (STOCs) and membrane potential were recorded using the perforated whole-cell configuration. To measure both, myocytes were continuously exposed to a bath solution consisting of 130 mM NaCl, 5 mM KCl, 2 mM $CaCl_2$, 1 mM $MgCl_2$, 10 mM glucose, and 10 mM HEPES, pH adjusted to 7.4 with NaOH. Pipettes were filled with an internal solution containing 110 mM K-aspartate, 30 mM KCl, 10 mM NaCl, 1 mM $MgCl_2$, 0.5 mM EGTA, and 10 mM HEPES adjusted to a pH of 7.3 with KOH. The internal solution was supplemented with 250 µg/ml

amphotericin B (Sigma, St. Louis, MO). STOCs were measured in the voltage-clamp mode and were analyzed with the threshold detection algorithm in Clampfit 10 (Axon Instruments, Inc). Membrane potential was measured in the current-clamp mode solely on cells exhibiting STOC activity.

Whole-cell ionic currents were recorded using the perforated whole-cell configuration. The composition of the external bath solution consisted of 134 mM NaCl, 6 mM KCl, 1 mM $MgCl_2$,2 mM $CaCl_2$,10 mM glucose, and 10 mM HEPES adjusted to a pH of 7.4 using NaOH. Pipettes were filled with an internal solution of 110 mM K-aspartate, 10 mM NaCL, 30 mM KCl, 1 mM $MgCl_2$, and 10 mM HEPES using NaOH to adjust to pH to 7.2. Myocytes were sustained at a holding potential of -70 mV before being exposed to a 400 ms ramp protocol from -140 to +60 mV. A voltage error of 12.8 mV resulting from the liquid junction potential was corrected for offline. Kir channels were blocked using 100 μM Ba^{2+}.

3.4 Model development

The male and female *in silico* models are single whole-cell models based on the electrophysiology of isolated unpressurized mesenteric vascular smooth muscle myocytes. A schematic of the proposed model is shown in **Figure 3.1**.

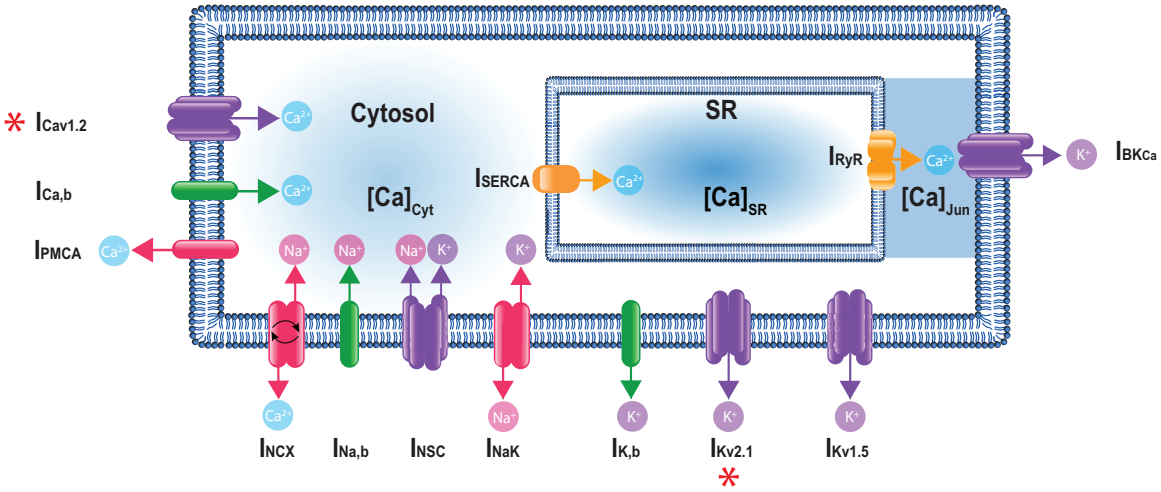

Figure 3.1. A schematic representation of the vascular smooth muscle (VSM) cell computational model. The components of the model include major ion channel currents shown in purple including the voltage-gated L-type calcium current ($I_{Cav1.2}$), nonselective cation current (I_{NSC}), and voltage-gated potassium currents ($I_{Kv1.5}$ and $I_{Kv2.1}$) and large-conductance Ca^{2+}-sensitive potassium current (I_{BKCa}). Currents from pumps and transporters are shown in red including the sodium/potassium pump current (I_{NaK}), sodium/calcium exchanger current (I_{NCX}), and plasma membrane ATPase current (I_{PMCA}). Leak currents are indicated in green including the sodium leak current ($I_{Na,b}$), potassium leak current ($I_{K,b}$), and calcium leak current ($I_{Ca,b}$). In addition, there are two currents in the sarcoplasmic reticulum shown in yellow: the sarcoplasmic reticulum Ca-ATPase current (I_{SERCA}) and ryanodine receptor current (I_{RyR}). Calcium compartments comprise three discrete regions including cytosol ($[Ca]_i$), sarcoplasmic reticulum ($[Ca]_{SR}$), and the junctional region ($[Ca]_{Jun}$). Red stars (*) indicate measured sex-specific differences in ion channels.

The membrane electrophysiology can be described by the differential equation:

$$\frac{dV}{dt} = \frac{-I_{ion}}{C_m} \qquad \text{(Eq. 3.1)}$$

Where V is voltage, t is time, C_m is membrane capacitance I_{ion} is the sum of transmembrane currents. The contribution of each transmembrane current to the total transmembrane ionic current can be described by the following equation:

$$I_{ion} = (I_{Kv1.5} + I_{Kv2.1} + I_{BKCa} + I_{K,b} + I_{Cav1.2} + I_{PMCA} + I_{Ca,b} + I_{NCX} + I_{NSC} + I_{NaK} + I_{Na,b}) \qquad \text{(Eq. 3.2)}$$

The eleven transmembrane currents are generated by ion channels, pumps, and transporters. Currents from ion channels include the voltage-gated L-type calcium current ($I_{Cav1.2}$), the nonselective cation current (I_{NSC}), voltage-gated potassium currents ($I_{Kv1.5}$ and $I_{Kv2.1}$), and the large-conductance Ca^{2+}-sensitive potassium current (I_{BKCa}). Additionally, there are three background or leak currents ($I_{K,b}$, $I_{Ca,b}$, and $I_{Na,b}$). Currents from pumps and transporters include the sodium-potassium pump current (I_{NaK}), plasma membrane Ca-ATPase transport current (I_{PMCA}), and sodium-calcium exchanger current (I_{NCX}). Cytosolic concentrations of sodium and potassium as a function of time are determined by considering the sum of their respective fluxes into the cytosol.

$$\frac{d[K^+]_i}{dt} = -\frac{\left(I_{Kv2.1}+I_{Kv1.5}+I_{BKca}+I_{K,b}-2I_{NaK}+I_{NSC-K}\right)}{z_K Vol_{cyt} F} \qquad \text{(Eq. 3.3)}$$

$$\frac{d[Na^+]_i}{dt} = -\frac{\left(3I_{NCX}+3I_{NaK}+I_{Na,b}+I_{NSC-Na}\right)}{z_{Na} Vol_{cyt} F} \qquad \text{(Eq. 3.4)}$$

Where F is the Faraday's constant, Vol_{cyt} is the cytoplasmic volume and z_K and z_{Na} are the valence of potassium and sodium ions, respectively.

The calcium dynamics is compartmentalized into three distinct regions; cytosol $[Ca^{2+}]_i$, the sarcoplasmic reticulum $[Ca^{2+}]_{SR}$, and the junctional region $[Ca^{2+}]_{jun}$. The cytosol includes calcium buffering which we assume can be described as a first-order dynamics process.

Cytosolic calcium region ($[Ca^{2+}]_i$*):* calcium concentration in this region varies between 100-300 nM and is mainly influenced by the following fluxes; transmembrane pumps and transporters, the sarcoplasmic reticulum Ca-ATPase (J_{SERCA}), diffusion from the junctional microdomain region ($J_{Jun-Cyt}$) and the calcium buffer calmodulin (BUF_{CAM}).

$$I_{Ca_{total}} = I_{CaL} + I_{Ca-leak} + I_{PMCA} - 2I_{NCX} \qquad \text{(Eq. 3.5)}$$

$$\frac{d[Ca^{2+}]_i}{dt} = \frac{-I_{Ca_{total}}}{Vol_{Cyt} * F * z_{Ca}} - J_{SERCA} + J_{jun-cyt} - \left(k_{BUF_{on}} * Ca_i * (BUF_T - BUF_{CAM}) - k_{BUF_{off}} * BUF_{CAM} \right) \quad \text{(Eq. 3.6)}$$

Sarcoplasmic reticulum region ($[Ca^{2+}]_{SR}$*):* calcium concentration in this region varies between 100-150 μM and it is mainly influenced by the sarcoplasmic reticulum Ca-ATPase (J_{SERCA}) and the ryanodine receptors (J_{RyR}).

$$\frac{d[Ca]_{SR}}{dt} = \left[\frac{Vol_{Cyt}}{Vol_{SR}}\right] J_{SERCA} - \left[\frac{Vol_{Cyt}}{Vol_{SR}}\right] [J_{Ryr}] \qquad \text{(Eq. 3.7)}$$

Junctional region ($[Ca^{2+}]_{jun}$*):* calcium concentration in this region varies between 10-100 μM and is mainly influenced by the flux from the ryanodine receptors (J_{RyR}), the diffusion from junctional region to cytoplasm ($J_{Jun-Cyt}$).

$$\frac{d[Ca]_{jun}}{dt} = \left[\frac{Vol_{Cyt}}{Vol_{jun}}\right] J_{Ryr} - \left[\frac{Vol_{Cyt}}{Vol_{jun}}\right] J_{jun-cyt} \qquad \text{(Eq. 3.8)}$$

Ion channel models. Male voltage-gated calcium current ($I_{Cav2.1}$) model equations.

Parameters	**Values**
Initial conditions (dL, dF)	(0.0062, 07450)
Activation parameters (x_1, x_2, x_3, x_4, x_5)	(0.3321, 12.9372, 0.1557, -10.3606, 1.763)
Inactivation parameters (x_1, x_2, x_3, x_4, x_5)	(0.0028, -54.1923, 0.0111, 22.3706, 74.28)

Table 3.1. Male parameters of $I_{Cav2.1}$

Male activation gate equations

$$alpha_{act} = 0.3321 * e^{\left(\frac{V}{12.9372}\right)};$$

$$beta_{act} = 0.1557 * e^{\left(\frac{V}{-10.3606}\right)};$$

$$dL_{bar} = \frac{1}{1 + \left(\frac{beta_{act}}{alpha_{act}}\right)};$$

$$tau_{dL} = \frac{1}{alpha_{act} + beta_{act}} + 1.763;$$

Male inactivation gate equations

$$alpha_{ina} = 0.0028 * e^{\frac{V}{-54.1923}};$$

$$beta_{ina} = 0.0111 * e^{\frac{V}{22.3706}};$$

$$dF_{bar} = \frac{1}{1 + \left(\frac{beta_{ina}}{alpha_{ina}}\right)};$$

$$tau_{dF} = \frac{1}{alpha_{ina} + beta_{ina}} + 74.28;$$

Activation and inactivation differential equations

$$\frac{dL}{dt} = \left(\frac{dL_{bar} - dL}{tau_{dL}}\right);$$

$$\frac{dF}{dt} = \left(\frac{dF_{bar} - dF}{tau_{dF}}\right);$$

The male voltage-gated calcium current is given by

$$I_{CaV,M} = 0.22 * dL * dF * \left(\frac{F^2}{R*T}\right) * V * \left(\frac{\left(Ca_i * e^{\left(\frac{z_{Ca}*F*Vm}{R*T}\right)} - Ca_{out}\right)}{e^{\left(\frac{z_{Ca}*F*Vm}{R*T}\right)} - 1.}\right) \text{(Eq. 3.9)}$$

Female voltage-gated calcium male current ($I_{Cav2.1}$) model equations.

Parameters	**Values**
Initial conditions (dL, dF)	(0.0062, 07450)
Activation parameters (x_1, x_2, x_3, x_4, x_5)	(0.4278, 10.8837, 0.1938, -11.5189, 1.8555)
Inactivation parameters (x_1, x_2, x_3, x_4, x_5)	(0.0032, -44.637, 0.0117, 30.4336, 68.7682)

Table 3.2. Female parameters of $I_{Cav2.1}$

Female activation gate equations

$$alpha_{act} = 0.4278 * e^{\left(\frac{V}{10.8837}\right)};$$

$$beta_{act} = 0.1938 * e^{\left(\frac{V}{-11.5189}\right)};$$

$$dL_{bar} = \frac{1}{1 + \left(\frac{beta_{act}}{alpha_{act}}\right)};$$

$$tau_{dL} = \frac{1}{alpha_{act} + beta_{act}} + 1.8555;$$

Female inactivation gate equations

$alpha_{ina} = 0.0028 * e^{\frac{V}{-54.1923}}$;

$beta_{ina} = 0.0111 * e^{\frac{V}{22.3706}}$;

$dF_{bar} = \frac{1}{1+\left(\frac{beta_{ina}}{alpha_{ina}}\right)}$;

$tau_{dF} = \frac{1}{alpha_{ina} + beta_{ina}} + 74.28$;

Activation and inactivation differential equations

$\frac{dL}{dt} = \left(\frac{dL_{bar} - dL}{tau_{dL}}\right)$;

$\frac{dF}{dt} = \left(\frac{dF_{bar} - dF}{tau_{dF}}\right)$;

The female voltage-gated calcium male current is given by

$$I_{CaV,F} = 0.38 * dL * dF * \left(\frac{F^2}{R*T}\right) * V * \left(\frac{\left(Ca_i * e^{\left(\frac{z_{Ca}*F*Vm}{R*T}\right)} - Ca_{out}\right)}{e^{\left(\frac{z_{Ca}*F*Vm}{R*T}\right)} - 1.}\right) \text{ (Eq. 3.10)}$$

Male voltage-gated potassium current ($I_{Kv2.1}$).

Parameters	**Values**
Initial conditions (p_{K21})	(0.0001)

Activation parameters (x_1, x_2, x_3, x_4, x_5)	(0.0404 10.5223 0.0355 221.4551 11.4616)
G_{K21}	0.7 (nS)

Table 3.3. Male parameters of $I_{Kv2.1}$

Male activation gate equations

$$alpha_x = 0.0404 * e^{\left(\frac{V}{10.5223}\right)}$$

$$beta_x = 0.0355 * e^{\left(\frac{V}{221.4151}\right)}$$

$$p_{Kbar} = \frac{1}{1+\left(\frac{beta_x}{alpha_x}\right)}$$

$$tau_{p_K} = \frac{1}{alpha_x+beta_x} + 11.4616$$

$$\frac{dp_{K21}}{dt} = \left(\frac{p_{Kbar} - p_K}{tau_{p_K}}\right)$$

The male voltage-gated $K_{v2.1}$ potassium current is given by

$$I_{Kv21,M} = G_{K21} * p_{K21} * (V - E_K) \qquad \text{(Eq. 3.11)}$$

Female voltage-gated potassium current ($I_{Kv2.1}$).

Parameters	**Values**
Initial conditions (p_{K21})	(0.0001)
Activation parameters (x_1, x_2, x_3, x_4, x_5)	(0.0717 12.9290 0.0533 191.7326 0.3489)
G_{K21}	1.8 (nS)

Table 3.4. Female parameters of $I_{Kv2.1}$

Female activation gate equations

$$alpha_x = 0.0717 * e^{\left(\frac{V}{12.9290}\right)}$$

$$beta_x = 0.0533 * e^{\left(\frac{V}{191.7326}\right)}$$

$$p_{Kbar} = \frac{1}{1+\left(\frac{beta_x}{alpha_x}\right)}$$

$$tau_{p_K} = \frac{1}{alpha_x+beta_x} + 0.3489$$

$$\frac{dp_{K21}}{dt} = \left(\frac{p_{Kbar} - p_K}{tau_{p_K}}\right)$$

The female voltage-gated $K_{v2.1}$ potassium current is given by

$$I_{Kv21,F} = G_{K21} * p_{K21} * (V - E_K) \qquad \text{(Eq. 3.12)}$$

Male voltage-gated potassium current ($I_{Kv1.5}$).

Parameters	**Values**
Initial conditions (p_{K15})	(0.0001)
Activation parameters (x_1, x_2, x_3, x_4, x_5)	(0.0717 12.9290 0.0533 191.7326 0.3489)
G_{K15}	1.8 (nS)

Table 3.5. Male parameters of $I_{Kv1.5}$

Male activation gate equations

$$alpha_x = 0.0717 * e^{\left(\frac{V}{12.9290}\right)}$$

$$beta_x = 0.0533 * e^{\left(\frac{V}{191.7326}\right)}$$

$$p_{Kbar} = \frac{1}{1+\left(\frac{beta_x}{alpha_x}\right)}$$

$$tau_{p_K} = \frac{1}{alpha_x+beta_x} + 0.3489$$

$$\frac{dp_{K15}}{dt} = \left(\frac{p_{Kbar} - p_K}{tau_{p_K}}\right)$$

The male voltage-gated $K_{v2.1}$ potassium current is given by

$$I_{Kv15,M} = G_{K15} * p_{K15} * (V - E_K) \qquad \text{(Eq. 3.13)}$$

Female voltage-gated potassium current $(I_{Kv1.5})$.

Parameters	**Values**
Initial conditions (p_{K15})	(0.0001)
Activation parameters (x_1, x_2, x_3, x_4, x_5)	(0.0666 9.6398 0.0637 123.4370 -0.0015)
G_{K15}	1.5 (nS)

Table 3.6. Female parameters of $I_{Kv1.5}$

Female activation gate equations

$$alpha_x = 0.0666 * e^{\left(\frac{V}{9.6398}\right)}$$

$$beta_x = 0.0637 * e^{\left(\frac{V}{123.4370}\right)}$$

$$p_{Kbar} = \frac{1}{1+\left(\frac{beta_x}{alpha_x}\right)}$$

$$tau_{p_K} = \frac{1}{alpha_x + beta_x} - 0.0015$$

$$\frac{dp_{K15}}{dt} = \left(\frac{p_{Kbar} - p_K}{tau_{p_K}}\right)$$

The female voltage-gated $K_{v2.1}$ potassium current is given by

$$I_{Kv15,F} = G_{K15} * p_{K15} * (V - E_K) \qquad \text{(Eq. 3.14)}$$

The activation of the large-conductance Ca-sensitive potassium (BK_{Ca}) current was adapted from the Tong-Taggart model [56].

Parameter	Value	Description
BK_T	6(male) & 8(female)	Number of BK_{Ca} channels
$perm_{BKCa}$	4.00E-13	Permeability of BK_{Ca} channels (cm^3/s)

Table 3.7. Parameters of I_{BKCa}

$$xabss_z = \left(-\frac{0.681249}{1.0+\left(\frac{Ca_{jun}*1000.0-0.218988}{0.428335}\right)*\left(\frac{Ca_{jun}*1000.0-0.218988}{0.428335}\right)} + \frac{1.40001}{1.0+\left(\frac{Ca_{jun}*1000.0+228.71}{684.946}\right)*\left(\frac{Ca_{jun}*1000.0+228.71}{684.946}\right)} \right)$$

$$xabss_{vh} = \left(\frac{8540.23}{\left(\left(\frac{Ca_{jun}*1000.0+0.401189}{0.00399115}\right)^{0.668054}\right)} \right) - 109.28;$$

$$xabss = \left(\frac{1.0}{1.0+e\text{^}\left(-xabss_z*\frac{F*V-xabss_{vh}}{R*T}\right)} \right)$$

$$xabtc = \left(\frac{13.8049}{1.0+\left(\frac{V-153.019}{66.4952}\right)*\left(\frac{V-153.019}{66.4952}\right)} \right)$$

$$\frac{dx_{ab}}{dt} = \left(\frac{xabss-x_{ab}}{xabtc}\right)$$

The large-conductance Ca^{2+}-sensitive potassium current (I_{BKCa}) is given by

$$I_{BKCa} = BK_T * Perm_{BKCa} * x_{ab} * \left(\frac{z_K^2 F^2}{R*T}\right) * V * \left(\frac{\left(K_{in} * e^{\left(\frac{z_{Ca}*F*Vm}{R*T}\right)} - K_{out}\right)}{e^{\left(\frac{z_{Ca}*F*Vm}{R*T}\right)} - 1.}\right) \quad \text{(Eq. 3.15)}$$

The nonselective cations currents (I_{NSC}) model is described as a linear and time-independent cation current permeable to K^+ and Na^+ with permeability ratios P_{Na}: P_K =0.9:1.3 adapted from Tong-Taggart model [58].

Parameter	Value	Description
PnsK	1.3	Permeability of K^+
PnsNa	0.9	Permeability of Na^+
gnsNa	0.5	Conductance ratio of Na^+
gnsK	0.1	Conductance ratio of K^+
gns	4.92 (varies)	Maximum Conductance (nS)

Table 3.8. Parameters of I_{NSC}

The reversal potential (E_{NSC}) of the I_{NSC} is described by

$$E_{NSC} = \left(R * \frac{T}{F}\right) * log\left(\frac{PnsK*K_{out}+PnsNa*Na_{out}}{PnsK*K_{in}+PnsNa*Na_{in}}\right)$$

The total nonselective cations current (I_{NSC}) is given by

$$I_{NSC} = (gnsNa) * gns * \left(V - (E_{nscc})\right) + (gnsK) * gns * (V - (E_{nscc})) \quad \text{(Eq. 3.16)}$$

Leak currents are described as linear and time independent.

Parameter	Value	Description
$G_{K,b}$	0.009	Maximum Conductance of K^+ (nS)
$G_{Na,b}$	0.001	Maximum Conductance of Na^+ (nS)
$G_{Ca,b}$	0.00256	Maximum Conductance of Ca^{2+} (nS)

Table 3.9. Parameters of leak currents

$$I_{Ca,b} = G_{Ca,b} * (V - E_{Ca}) \quad \text{(Eq. 3.17)}$$

$$I_{Na,b} = G_{Na,b} * (V - E_{Na}) \quad \text{(Eq. 3.18)}$$

$$I_{K,b} = G_{K,b} * (V - E_K) \quad \text{(Eq. 3.19)}$$

Pumps and transporters were optimized to data available in the experimental literature and/or taken from computational models of vascular smooth muscle and cardiac cells. The sodium-potassium pump (I_{NaK}) current was modeled using data from smooth muscle cells from mesenteric resistance arteries of the guinea pig [27] and the voltage dependency was adapted from the Lou-Rudy II model [59].

Parameter	Value	Description
$I_{NaK_{max}}$	104.16	Maximum NaK current (pA)
$KmNaK_K$	1.6	Potassium selectivity (mM)
$KmNaK_{Na}$	22	Sodium selectivity (mM)
Q10	1.87	Q10 coefficient

Table 3.10. Parameters of I_{NaK}

$$N_{pow} = \left(Q10^{\frac{T-309.2}{10}}\right);$$

$$N_1 = \frac{(K_{out}^{1.1})}{K_{out}^{1.1} + KmNaK_K^{1.1}};$$

$$N_2 = \frac{(Na_{in}^{1.7})}{Na_{in}^{1.7} + KmNaK_{Na}^{1.7}};$$

$$N_0 = \frac{1.0}{1 + \left(0.1245 * exp\left(-0.1 * V * \frac{F}{R * T}\right)\right) + \left(2.19e - 3 * \left(e^{\left(\frac{Na_{out}}{49.71}\right)}\right) * e^{\left(-1.9 * V * \frac{F}{R * T}\right)}\right)};$$

$$I_{NaK} = I_{NaK_{max}} * N_1 * N_2 * N_0 * N_{pow} \quad \text{(Eq. 3.20)}$$

The sodium-calcium exchanger current (I_{NCX}) was adapted from the formulation in the ten Tusscher model [60] and the Lou-Rudy II [59].

Parameter	Value	Description
P_{NCX}	0.0003	Maximum NCX current (pA)
gammax	1.6	coefficient

Table 3.11. Parameters of I_{NCX}

$$phi_F = exp\left(gammax * V * \frac{F}{R * T}\right)$$

$$phi_R = exp\left((gammax - 1) * V * \frac{F}{R * T}\right)$$

$$X_{NCX} = \frac{\left(Na_{in}^3\right) * Ca_{out} * phi_F - \left(Na_{out}^3\right) * Ca_i * phi_R}{1 + 0.0003 * \left(\left(Na_{out}^3\right) Ca_{in} + \left(Na_{in}^3\right) * Ca_{out}\right)};$$

$$I_{NCX} = P_{NCX} * X_{NCX} \quad \text{(Eq. 3.21)}$$

The sarcolemma calcium pump (I_{PMCA}) current was adapted from [61].

Parameter	Value	Description
$I_{PMCAbar}$	2.8	Maximum PMCA current (pA)
K_{mPMCA}	170E-6	Calcium binding capacity (mM)

Table 3.12. Parameters of I_{PMCA}

$$I_{PMCA} = I_{PMCAbar} * \frac{Ca_i^2}{Ca_i^2 + K_{mPMCA}^2} \quad \text{(Eq. 3.22)}$$

Finally, the mathematical formulation of fluxes (J_{SERCA}) and (J_{RyR}) are described.

The sarcoplasmic reticulum Ca-ATPase flux (J_{SERCA}) is given by

Parameter	Value	Description
$I_{SERCAbar}$	5.25E-6	Maximum SERCA flux
K_{mSERCA}	219E-6	Calcium binding capacity (mM)

Table 3.13. Parameters of J_{SERCA}

$$J_{SERCA_{ALL}} = I_{SERCAbar} * \left(\frac{Ca_i^2}{Ca_i^2 + K_{mSERCA}^2}\right) \quad \text{(Eq. 3.23)}$$

The ryanodine receptor flux (J_{RyR}) is given by

Parameter	Value	Description
n_RyR_Ca_jun	1.2	
Ca_{TH}	0.12	SR Load Ca threshold (mM)
Kd	500	Calcium binding capacity (1/mM*ms)
V_{RyR}	0.0022	Maximum RyR release rate (1/ms)
$V_{jun-cyt}$	0.0008	Maximum Ca diffusion rate from junctional region to cytosol (1/ms)

Table 3.14. Parameters of J_{RyR}

$$\mathrm{Y_{SR}} = \frac{1}{1 + \left(\frac{Ca_{TH}}{[Ca]_{SR}}\right)^5}$$

$$\tau_n = \frac{1}{\alpha + \beta} = \frac{1}{K_d\left(Ca_{jun}^{\mathrm{n\_RyR\_Ca\_jun}}\ \mathrm{Y_{SR}} + \mathrm{Ca}_{\mathrm{jun_{TH}}}^{\mathrm{n\_RyR\_Ca\_jun}}\right)}$$

$$n_\infty = \frac{\alpha}{\alpha + \beta} = \frac{K_d Ca_{jun}^{\mathrm{n\_RyR\_Ca\_jun}}}{K_d\left(Ca_{jun}^{\mathrm{n\_RyR\_Ca\_jun}}\ \mathrm{Y_{SR}} + \mathrm{Ca}_{\mathrm{jun_{TH}}}^{\mathrm{n\_RyR\_Ca\_jun}}\right)} = \frac{Ca_{jun}^{\mathrm{n\_RyR\_Ca\_jun}}\ \mathrm{Y_{SR}}}{\left(Ca_{jun}^{\mathrm{n\_RyR\_Ca\_jun}}\ \mathrm{Y_{SR}} + \mathrm{Ca}_{\mathrm{jun_{TH}}}^{\mathrm{n\_RyR\_Ca\_jun}}\right)}$$

$$\frac{dn}{dt} = \frac{n_\infty - n}{\tau_n}$$

$$J_{RyR} = V_{RyR} * n * (Ca_{SR} - Ca_{jun}) \qquad \text{(Eq. 3.24)}$$

$$J_{jun-cyt} = V_{jun-cyt} * (Ca_{jun} - Ca_i) \qquad \text{(Eq. 3.25)}$$

3.5 Whole-cell male and female models

Membrane potential. First, we set the baseline membrane potential at -40 mV by adjusting the non-selective cation current (I_{NSC}) and checked that under the same initial conditions the male and female models reach steady-state. We observed that K^+, Na^+, and Ca^{2+} concentrations reach a steady-state as shown in **Figure 3.2**.

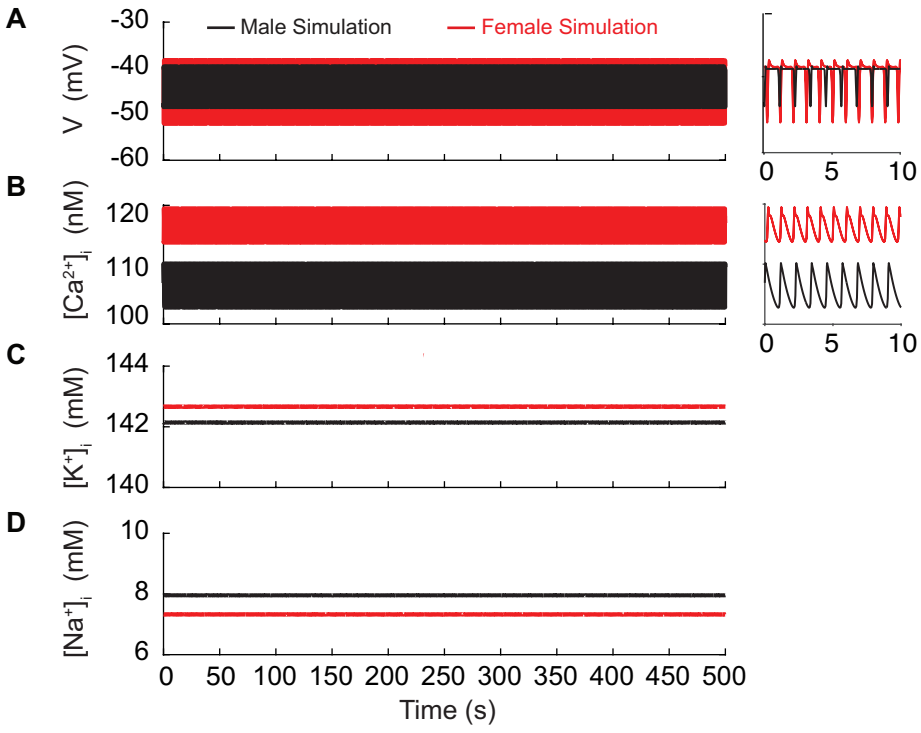

Figure 3.2. Membrane potential and ionic concentrations. Membrane potential (A) and Ca^{2+} (B), K^+(C), and Na^+(D) ion concentrations.

Ionic currents. Using the same initial conditions, we observed that in fact, sex-specific differences in $Ca_V1.2$ and $K_v2.1$ channels have an effect in the whole-cell models of male and female VSMCs. Notably, ionic currents responsible for the maintenance of Ca^{2+} signaling behave differently in male compared to female VSMCs as shown in **Figure 3.3**.

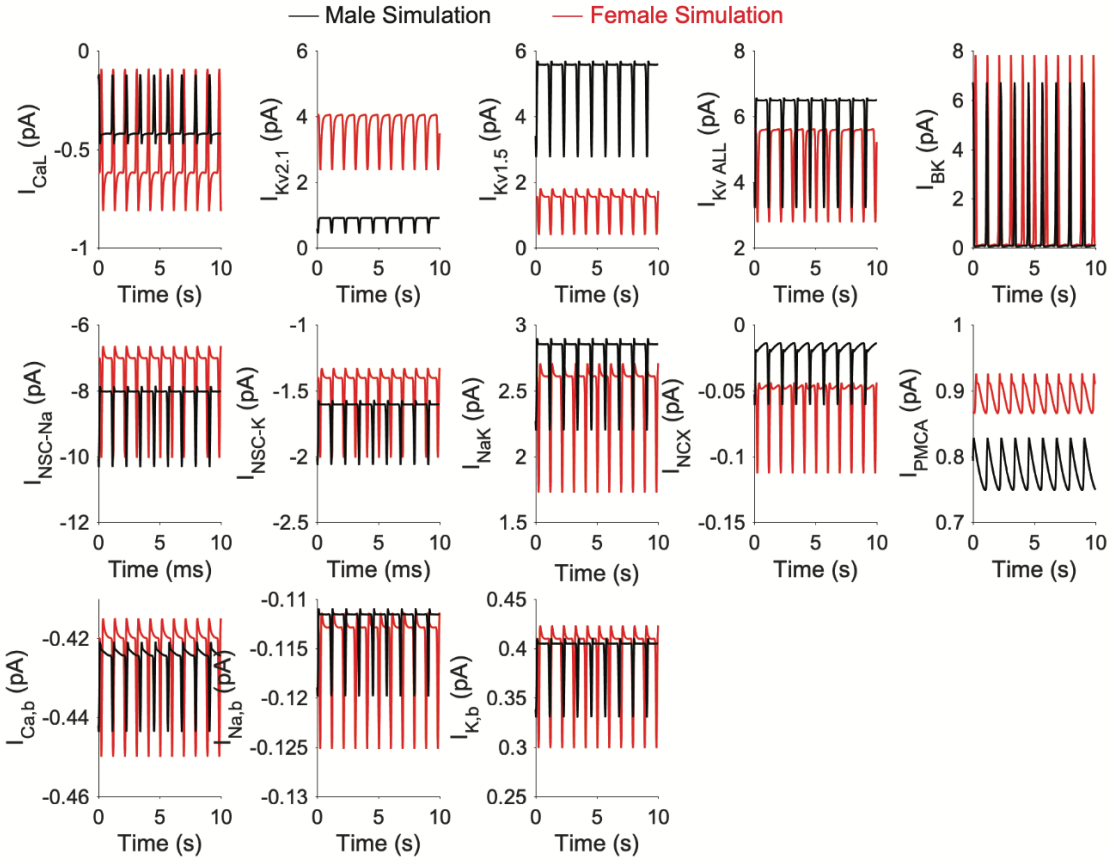

Figure 3.3. Ionic Currents. Currents in the plasma membrane of VSMCs in the male and female models

Calcium signaling. We validated Ca^{2+} signaling in the male model and used the same assumptions in the female model. ZhuGe *et al*. [62] showed elegantly the relationship between $[Ca^{2+}]_{SR}$ and Ca^{2+} sparks by devising an experimental approach to directly measure $[Ca^{2+}]_{SR}$ and its relationship to $[Ca^{2+}]_i$. First, they observed that $[Ca^{2+}]_{SR}$

oscillates between 110-120 μM causing Ca^{2+} sparks. Second, a Ca^{2+} spark produces a release of Ca^{2+} of about 10-20 μM. Finally, Ca^{2+} sparks have a minimal effect on $[Ca^{2+}]_i$. In **Figure 3.4**, Ca^{2+} signaling in the cytosol $[Ca^{2+}]_i$, the sarcoplasmic reticulum $[Ca^{2+}]_{SR}$, and the junctional region $[Ca^{2+}]_{jun}$ is shown when the baseline membrane potential in both male and female myocytes was set at -40 mV.

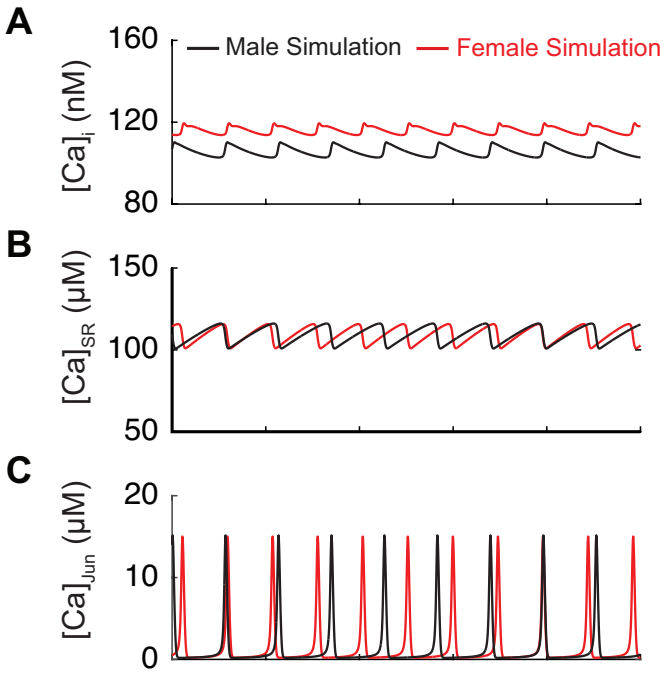

Figure 3.4. **Calcium signaling**. Ca^{2+} signaling in the male and female models. (A) The cytosol $[Ca^{2+}]_i$, (B) the sarcoplasmic reticulum $[Ca^{2+}]_{SR}$, and (C) the junctional region $[Ca^{2+}]_{jun}$.

3.6 Results

In this study, we endeavored to develop a computational model of the electrical activity of an unpressurized single vascular smooth muscle cell (**Figure 3.4**). We optimized and validated the model with experimental data and then used the model to predict the effects

of measured sex-dependent differences in the electrophysiology of smooth muscle myocytes.

In constructing the model, we first set out to measure the kinetics of the voltage-gated L-type calcium current $Ca_V1.2$ ($I_{Cav1.2}$) in male and female myocytes as shown in **Figure 3.5**. $I_{Cav1.2}$ is critical in determining cytosolic concentration $[Ca^{2+}]_i$ in vascular mesenteric smooth muscle cells and is the predominant pathway for Ca^{2+} entry [17-19]. Experiments using whole-cell patch-clamp were undertaken to measure the time constants of activation (**panel 3.5A**) and inactivation (**panel 3.5B)** in male and female mesenteric artery smooth muscle cells (shown as red and black symbols, respectively). While the data from male (n = 10) and female (n = 11) myocytes showed comparable activation time constants, small differences were observed in the inactivation time constants. Notably, inactivation is faster in female compared male myocytes in the physiologically relevant range of the myocyte from -50 to -20 mV. Steady-state activation and inactivation were also measured as shown in **panel 3.5C**, with male data in black symbols and female as red symbols. No differences in the gating characteristics of the male and female $I_{Cav1.2}$ were measured. Finally, the current-voltage relationship is shown from measurements in female (red) and male (black) in **panel 3.5D.** Measurements at the peak current indicate that female cells exhibit significantly larger whole-cell currents ($P<0.05$). Together, these data suggest notable sex-specific differences in $I_{Cav1.2}$, which may result in physiological differences in mesenteric smooth muscle cells and vessels.

To begin to better understand the impact of sex-specific differences in $I_{Cav1.2}$, we next used the experimental measurements to build and optimize a Hodgkin-Huxley model to the data described above. The model contains voltage-dependent activation and inactivation gating variables, dL and dF, respectively. Both gates were modeled following the approach by Kernik et al. [48]. Because smooth muscle cells operate within a voltage regime designated by the window current (between -50 mV and -20 mV) cytosolic calcium concentration remains below 1 μM. Therefore, we did not consider the calcium-dependent inactivation gating mode of the channel [21, 56]. The male and female models of $I_{Cav1.2}$ are described by Eq.3.9 and Eq.3.10 respectively.

Parameters were optimized to male and female experimental data as shown for activation time constants ($\tau_{activation}$) and inactivation time constants ($\tau_{inactivation}$) as solid lines in **Figure 3.5A** and **Figure 3.5B**, respectively. Model optimization to male and female activation and inactivation curves are shown in **Figure 3.5C**. The model was also optimized to the $I_{Cav1.2}$ current-voltage (I-V) relationships shown as lines in **Figure 3.5D**.

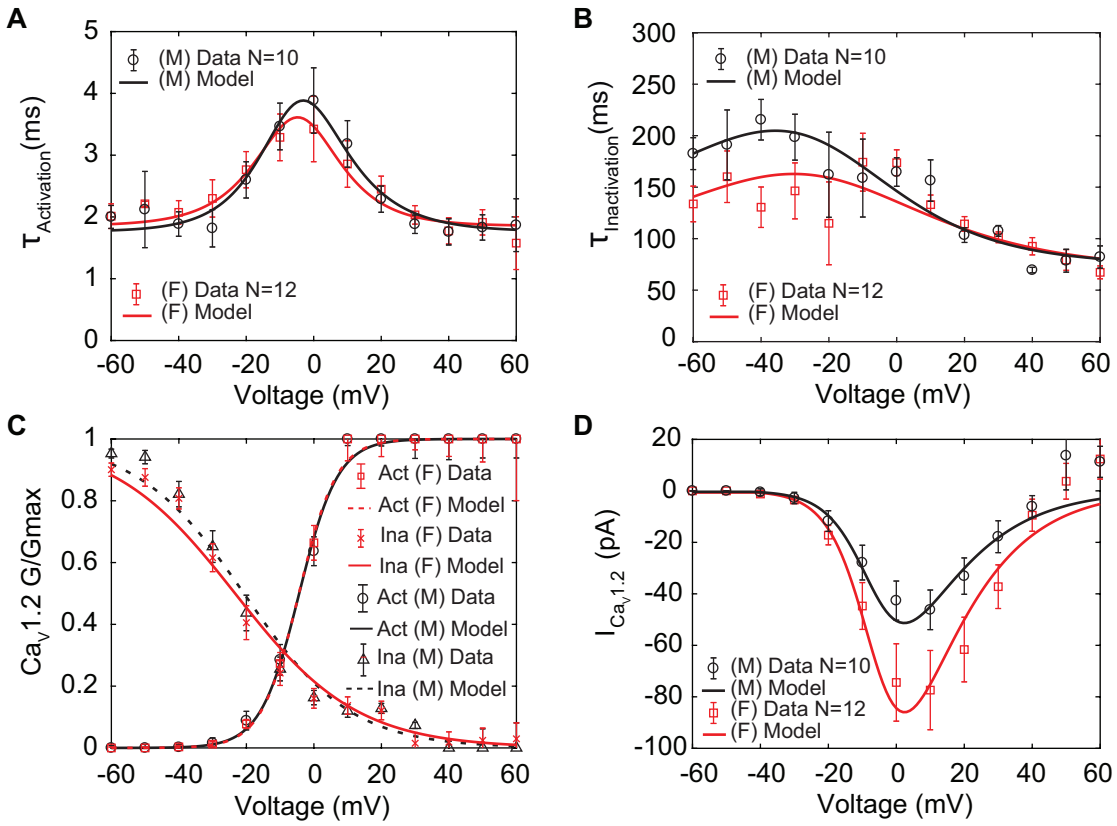

Figure 3.5. L-type calcium currents ($I_{Cav1.2}$) were experimentally measured and modeled from male and female vascular smooth muscle cells. Properties of $I_{Cav1.2}$ are derived from measurements in male and female vascular smooth muscle (VSM) cells isolated from the mouse mesenteric arteries following voltage-clamp steps from -60 to 60 mV in 10 mV steps from a -80 mV holding potential. Experimental data is shown in black circles for male and red squares for female. Model fits to experimental data are shown with black solid lines for male and red solid lines for female. (A) Male and female time constants of $I_{Cav1.2}$ activation. (B) Male and female time constants of $I_{Cav1.2}$ inactivation. (C) Male and female voltage-dependent steady-state activation and inactivation of $I_{Cav1.2}$. (D) Current-voltage (I-V) relationship of $I_{Cav1.2}$ from male and female vascular smooth muscle myocytes.

We next set out to determine sex differences in voltage-gated K^+ currents (I_K) in male and female mesenteric smooth muscle cells. I_K is produced by the combined activation of K_V and BK_{Ca} channels. Following the approach previously published by O'Dwyer et al [15], we quantified the contribution of K_V (I_{KV}) and BK_{Ca} (I_{BKCa}) current to I_K. K^+ currents were recorded before and after the application of the channel blocker iberiotoxin (IBTX; 100nm). Once identified the contribution I_{BKCa} current, we isolated the voltage-gated

potassium currents (I_{KV}) whose contributors include the voltage-gated potassium channels $K_V1.5$ and $K_V2.1$. The presumed function of $K_V1.5$ and $K_V2.1$ channels on membrane potential is to produce delayed rectifier currents to counterbalance the effect of inward currents [15, 22].

Having isolated I_{KV}, $K_V2.1$ currents were identified using the application of the $K_V2.1$ blocker ScTx1 (100 nM). As a result, the remaining current, the ScTx1-insensitive component of I_{KV} was attributed to the current produced by $K_V1.5$ channels. The results are shown in **Figure 3.6**. Experiments using whole-cell patch-clamp were undertaken to measure the steady-state activation G/G_{max} of the $K_V2.1$current ($I_{Kv2.1}$) as shown in **panel 3.6A** in female (red) and male (black) myocytes and no significant differences were observed. Measurements of time constants of activation (**panel 3.6B**) of $I_{Kv2.1}$ at -30 mV in female (red, n=10) and male (black, n=7) myocytes exhibited significant differences ($P<0.01$). Notably, activation time constants were faster in male compared to female myocytes. The current-voltage relationship of $I_{Kv2.1}$ is shown from measurements in female (red, n=20) and male (black, n=10) myocytes in **panel 3.6C**. Similarly, we measured the steady-state activation of the $K_V1.5$ current ($I_{Kv1.5}$), as shown in **Panel 3.6D** where male and female experimental data in myocytes are shown with red and black symbols. Properties of $I_{Kv1.5}$ steady-state activation G/G_{max} show minimal sex-specific differences. The current-voltage relationship of $I_{Kv1.5}$ is shown from measurements in female (red, n=10) and male (black, n=7) myocytes in **panel 3.6E.** Finally, the current-voltage relationship of the contribution from $I_{Kv1.5}$ and $I_{Kv2.1}$ to the total voltage-gated current (I_{KVTOT}) is shown in **panel 3.6F** with male and female data shown with black and

red symbols, respectively. The table in **panel 3.6H** summarizes the sex-dependent maximal conductance and the current response at specific voltages of -50 mV, -40 mV, -30 mV, and -20 mV for both $I_{Kv1.5}$ and $I_{Kv2.1}$

To understand the contribution of each K^+ current to the total voltage-gated current (I_{KVTOT}) in mesenteric vascular smooth muscle cells we built and optimized a Hodgkin-Huxley model to the data described above. First, we developed a model to describe the $K_V2.1$ current. The optimized model to $K_V2.1$ experimental data contains only a voltage-dependent activation gating variable ($X_{2.1act}$). Since inactivation time is so slow and is well estimated by steady-state [54], we did not consider its effects in our model. The male and female models of $I_{Kv2.1}$ are described by Eq.3.11 and Eq.3.12 respectively.

Parameters were optimized to male and female experimental data as shown for activation curves in **Figure 3.6A**. Model optimization to male and female time constants of activation ($K_V2.1$ $\tau_{Activation}$) are shown as solid lines in **Figure 3.6B**. The model was also optimized to the $I_{Kv2.1}$ current-voltage (I-V) relationships shown as solid lines in **Figure 3.6C**.

Similarly, we developed a model for $K_V1.5$. The model was optimized to the $K_V1.5$ experimental data and contains only a voltage-dependent activation gating variable ($X_{Kv1.5act}$). The male and female models of $I_{Kv1.5}$ are described by Eq.3.13 and Eq.3.14.

Parameters were optimized to male and female experimental data as shown for activation curves in **Figure 3.6D**. The model was also optimized to the $I_{Kv1.5}$ current-voltage (I-V) relationships shown as solid lines in **Figure 3.6E**. From experiments, we optimized the model to reproduce the overall time traces of K_V currents. The model predicted that male and female myocytes have comparable time constants of activation in $I_{Kv1.5}$ as shown in **Figure 3.6G.** Finally, the optimized model of the total voltage-gated current (I_{KVTOT}) is shown in **Figure 3.6F**. The total voltage-gated K^+ current (I_{KvTOT}) is the sum of $I_{KV1.5}$ and $I_{Kv2.1}$ mathematically described as:

$$I_{KVTOT} = I_{Kv2.1} + I_{KV1.5} \qquad \text{(Eq. 3.26)}$$

Notably, the main specific sex-specific differences observed in the total voltage-gated K^+ current (I_{KvTOT}) is attributable to the sex-specific differences in the current produced by K_V2.1 channels.

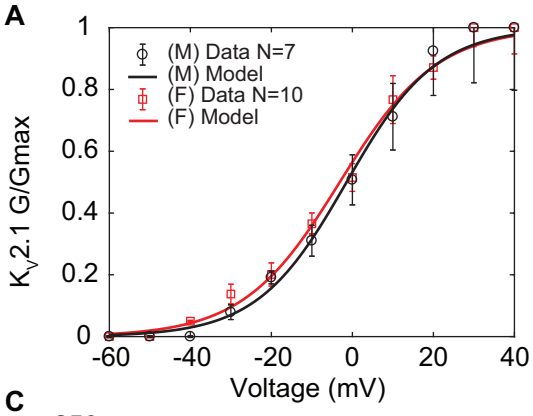

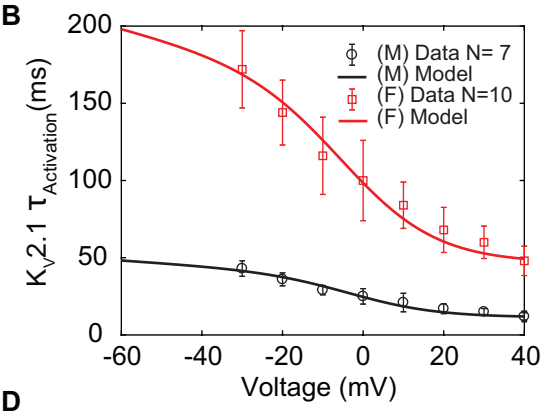

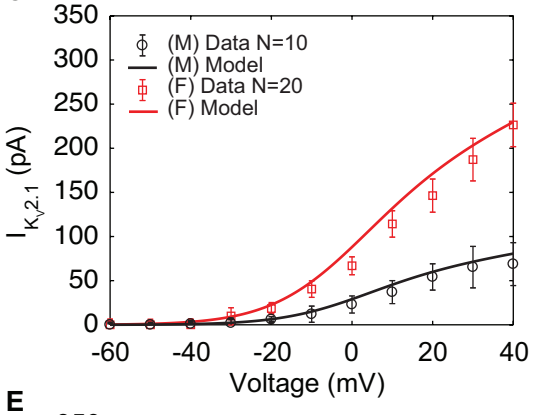

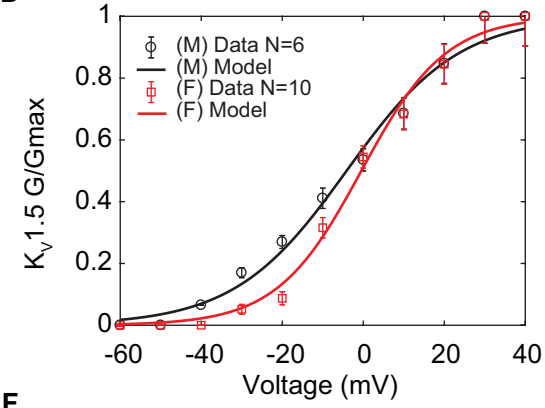

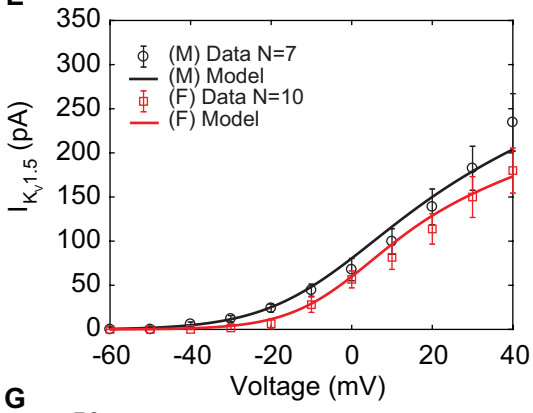

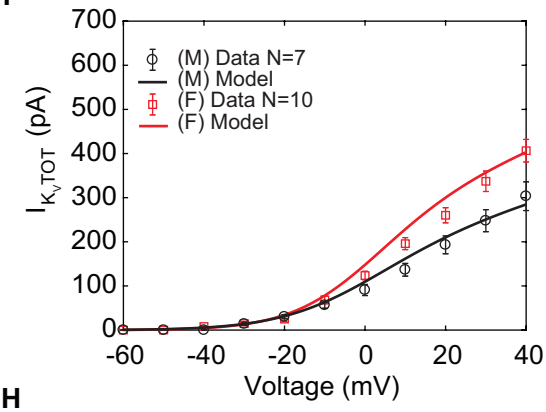

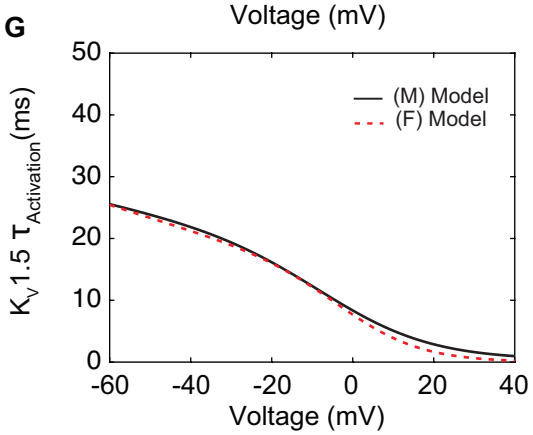

H

	Male	Female
Kv 2.1 Gmax	0.7 nS	2.0 nS
Kv 1.5 Gmax	1.8 nS	1.5 nS
Current applied*(-50 mV)	2.01 pA	1.45 pA
Current applied*(-40 mV)	5.5 pA	4.5 pA
Current applied*(-30 mV)	13.9 pA	13.2 pA
Current applied*(-20 mV)	31.5 pA	34.4 pA

Figure 3.6. Experimentally measured and modeled potassium (K_V) currents from male and female vascular smooth muscle cells. Properties of $I_{Kv1.5}$ and $I_{Kv2.1}$ from experimental measurements in male and female vascular smooth muscle (VSM) cells isolated from the mouse mesenteric arteries recorded in response to voltage-clamp from -60 to 40 mV in 10 mV steps (holding potential -80mV). Experimental data is shown as black circles for male and red squares for female. Model fits to experimental data are shown with black solid lines for male and red solid lines for female. (A) Male and female voltage-dependent steady-state activation of $I_{Kv2.1}$. (B) Male and female time constants of $I_{Kv2.1}$ activation. (C) Current-voltage (I-V) relationship of $I_{Kv2.1}$ from male and female myocytes. (D) Male and female voltage-dependent steady-state activation of $I_{Kv1.5}$. (E) Current-voltage (I-V) relationship of $I_{Kv1.5}$ from male and female myocytes. (F) Male and female total voltage-gated potassium current $I_{KvTOT} = I_{Kv1.5} + I_{Kv2.1}$. (G) Predicted male and female time constants of the $I_{Kv1.5}$ activation gate. (H) Table showing sex-specific differences in conductance and the voltage dependence of steady-state total potassium current.

We next analyzed the contribution of large-conductance calcium-activated potassium (BK_{Ca}) channels to vascular smooth muscle cell electrophysiology. BK_{Ca} channels are activated by both voltage and Ca^{2+} and are expressed in the membrane of vascular smooth muscle cells with α and β1 subunits [63]. In smooth muscle cells, Ca^{2+} sparks are the physiological activators of BK_{Ca} channels.

We relied on the assumption by Tong et al. [58] that BK_{Ca} currents (I_{BKCa}) are produced by two currents subtypes, one consisting of α subunits ($I_{BK\alpha}$) and the other consisting of α and β1 subunits ($I_{BK\alpha\beta1}$). Experimental evidence indicates that BK_{Ca} channels with αβ1 subunits form clusters in the plasma membrane in specialized junctional domains formed by the sarcoplasmic reticulum and the sarcolemma. BK_{Ca} channels with αβ1 subunits colocalize with ryanodine receptors (RyRs) in the junctional domains. During a Ca^{2+} spark, $[Ca^{2+}]_{Jun}$ elevations ranging from 10 to100 μM activate BK_{Ca} channels [64]. In our model, Ca^{2+} sparks are the physiological activators of BK_{Ca} channels.

The mathematical formulation of the BK_{Ca} with αβ1 current ($I_{BK\alpha\beta1}$) was optimized to fit the experimental whole-cell electrophysiological data from Bao and Cox 2005 obtained at room temperature from cloned mammalian smooth muscle cell with α and β1subunits expressed in *Xenous leavis* oocytes [63]. Experimental data for steady-state activation and time constants of activation is shown in **Panel 3.7A** and **Panel 3.7B** respectively. The activation gating variable (X_{ab}) depends on both voltage and junctional calcium ($[Ca^{2+}]_{Jun}$). The activation gate was adapted from the Tong-Taggart model [56]. The model of $I_{BK\alpha\beta1}$ is described by Eq. 3.15.

Model optimization to activation curves are shown with solid lines in **Figure 3.7A** at three different $[Ca^{2+}]_{Jun}$ concentrations 1 μM, 10 μM, and 100 μM. The results from the steady-state activation measurements at 10 μM are also in agreement with the experimental data in vascular myocytes by [64] (green symbols), which suggests that BK_{Ca} channels are exposed to a mean junctional calcium concentration ($[Ca^{2+}]_{Jun}$) of 10 μM. Time constants of activation were measured experimentally at $[Ca^{2+}]_{Jun}$ = 0.003 μM. Our model was optimized and fit under the same conditions shown in **Figure 3.7B** as solid lines. Notably when the model was run under predicted $[Ca^{2+}]_{Jun}$ = 10 μM conditions as shown in **Figure 3.7B** dashed lines, there is no effect of the change in $[Ca^{2+}]_{Jun}$ on the time constant. The predicted current-voltage (I-V) relationships of $I_{BK\alpha\beta1}$ are shown in **Figure 3.7C** using three different $[Ca^{2+}]_{Jun}$ concentrations; 1 μM, 10 μM, and 100 μM. We observed that the I-V curves are similar at $[Ca^{2+}]_{Jun}$ concentrations of 10 μM (black trace) and 100 μM (red trace) but markedly reduced when $[Ca^{2+}]_{Jun}$ = 1 μM (blue trace). As expected, the amplitude of the current shown in the I-V curves in **Figure 3.7D** is sensitively dependent

on the number of BK_{Ca} channels as shown, we set $[Ca^{2+}]_{Jun}$= 10 μM and simulated the I-V curves using a BK_{Ca} cluster size of 4, 6, 8 and 10 channels.

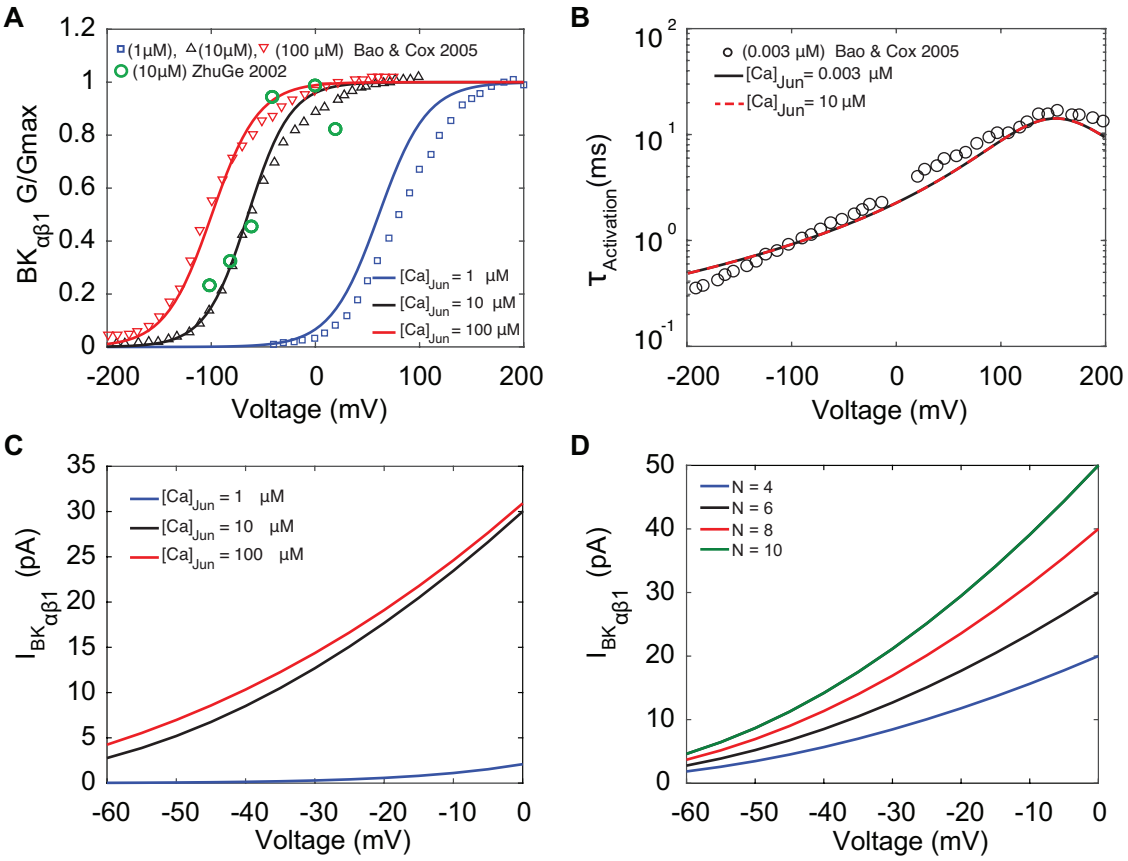

Figure 3.7. Experimentally measured and modeled large-conductance Ca^{2+}-activated K^+ (BK_{ca}) currents. The model was optimized to data from Li Bao and Brian H. Cox 2005. (A) Voltage-dependent activation of I_{BKCa} from experiments performed with three different $[Ca]_{Jun}$ concentrations (1 μM, 10 μM, 100 μM) shown in green circles is the data from [64] (B) Voltage-dependent activation time constants with $[Ca]_{Jun}$=0.003 μM and simulations $[Ca]_{Jun}$=10 μM. (C) Simulated I-V curve at different peak levels of $[Ca]_{Jun}$ levels. (D) Simulated I-V curve with different BK_{ca} average cluster sizes (N = 4,6, 8, and 10).

In VSMCs, the membrane potential over physiological intravascular pressures is less negative than the equilibrium potential of potassium (E_K = -84 mV), suggesting active participation of inward currents regulated by sodium conductance [65, 66]. It has been postulated that basally activating TRP channels generate the nonselective cations currents (I_{NSC}) that depolarize the membrane potential. Studies in cerebral vascular

smooth muscle cells suggest that TRPM4 channels are selective for monovalent cations, activated by, but impermeable to Ca^{2+} and are the main contributors of the I_{NSC} [67]. We built a model for I_{NSC} as linear and time-independent cation current permeable to K^+ and Na^+ with permeability ratios P_{Na}: P_K =0.9:1.3 adapted from Tong-Taggart model [56] with a reversal potential (E_{NSC}) described by Eq.3.16.

The electrical activity of isolated mesenteric smooth muscle cells in male and female myocytes was recorded under current-clamp and voltage-clamp. In current-clamp mode, we observed that under physiological conditions, the membrane potential in myocytes was not stable. Rather the membrane potential exhibited spontaneous transient hyperpolarizations (THs) a ubiquitous feature of vascular smooth muscle cells [68-70] as shown in **panel 3.8A.** Both male (black trace) and female (red trace) myocytes exhibited membrane hyperpolarizing transients in the potential range of -50 to -20 mV. Notably, we observed that female myocytes always reached a higher depolarizing state compared to male myocytes.

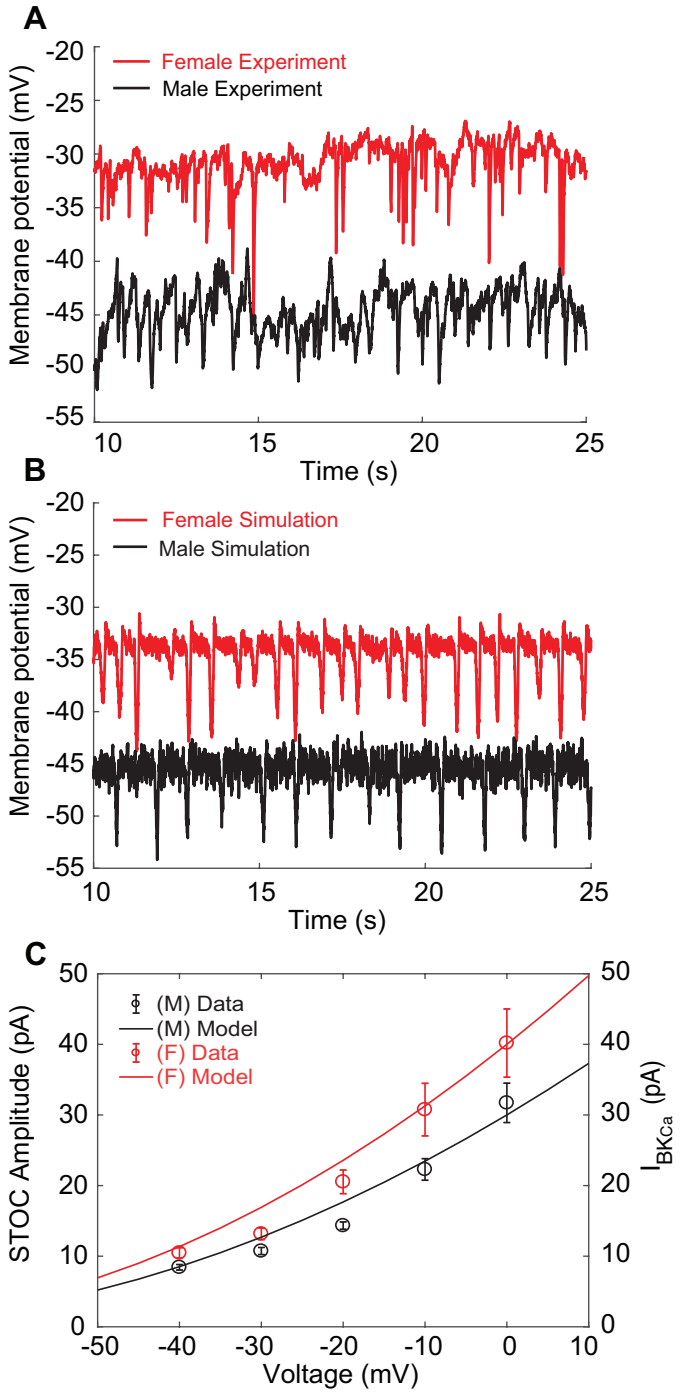

Figure 3.8. Membrane potential from experiments and simulations in male and female vascular smooth muscle myocytes. A) Whole-cell membrane potential recordings in male and female myocytes. B) Simulated whole-cell membrane potential with physiological noise. C) Model prediction suggests that female myocytes must have an average BK_{Ca} cluster size of 8 channels compared to 6 channels in male myocytes to reproduce experimental data indicating the amplitude of spontaneous transient outward currents (STOCs).

We assessed the predictive capacity of our *in silico* model by comparing it to experimental data. We first compared the morphology of the membrane potential in experiments **panel 3.8A** versus simulations **panel 3.8B** in male and female myocytes. Over the physiological range in which smooth muscle cells operate (-50 to -20 mV), ionic currents are small and produced by the activation of a small number of ion channels. Local fluctuations in the function of ion channels lead to noisy macroscopic signals that are important to the variability of vascular smooth muscle cell [71]. In addition, smooth muscle cells are subject to high input resistance where small perturbations can lead to large changes in membrane potential [38]. To approximate the physiological realities, we applied two sources of noise to our deterministic *in silico* model to simulate the stochastic fluctuations. The first source of the noise was introduced by adding a fluctuating current term to the differential equations describing changes in membrane potential (dV/dt) that represents the combined effect of the stochastic activity of ion channels in the plasma membrane. Second, we applied noise to the gating of ryanodine receptors (RyRs), which is a probabilistic local process originating at a single primary calcium discharge region [38, 72]. Simulated whole-cell membrane potential with physiological noise is shown in **figure 3.8B** in male (black trace) and female (red trace) myocytes.

In experiments during voltage-clamp, we observed spontaneous transient outward currents (STOCs), and we measured them at a membrane potential of -40, -30, -20, 0, and 10 mV. The amplitude of the STOCs exhibits small sex-specific differences in mesenteric artery smooth muscle cells shown as red and black symbols in **panel 3.8C**.

The computational model simulations led to the prediction that the STOC amplitudes in male and female myocytes are produced when BK_{Ca} channel clusters in the primary calcium discharge region contain 6 and 8 channels, respectively as shown in **figure 3.8C**.

Next, using the whole-cell vascular smooth muscle myocyte computational model, we investigated the sex-specific differences in the contribution to total voltage-gated current (I_{KVTOT}) in mesenteric vascular smooth muscle cells. An interesting prediction from the *in silico* simulations is that, at different depolarizing states (-45, -40, and -35 mV) induced by changing the conductance of nonselective cationic leak currents (I_{NSC}), the contribution of $I_{Kv2.1}$ and $I_{Kv1.5}$ to I_{KvTOT} is different based on sex. In male vascular myocytes, the contribution to total voltage-gated current (I_{KVTOT}) is largely attributable to the current produced by $K_V1.5$ channels as shown in the lower panel in **figure 3.9A**. Our modeling results are consistent with the work of multiple studies by [41, 73, 74] in animal rodent male models showing the characteristic behavior of $I_{Kv1.5}$ to control membrane potential. However, the model predicts that in female myocytes, the contribution to total voltage-gated current (I_{KVTOT}) is largely provided by the current produced by $K_V2.1$channels as shown in the upper panel in **figure 3.9B**. To illustrate this point quantitatively, at a membrane potential of -40 mV, the contribution from $I_{Kv1.5}$ is 86% and $I_{Kv2.1}$ is 14% in male myocytes, while on female myocytes the contribution from $I_{Kv1.5}$ is 28% and $I_{Kv2.1}$ is 72%. Regardless of depolarizing state at -45, -40, and -35 mV, the profiles for male and female myocytes remain essentially the same as shown in **figures 3.9C**, **3.9D,** and **3.9E**. The *in silico* simulations suggest a distinctive sex-based function of $K_V1.5$ and $K_V2.1$ channels

that produce the delayed rectifier currents to counterbalance the effect of inward currents causing graded membrane potential depolarizations.

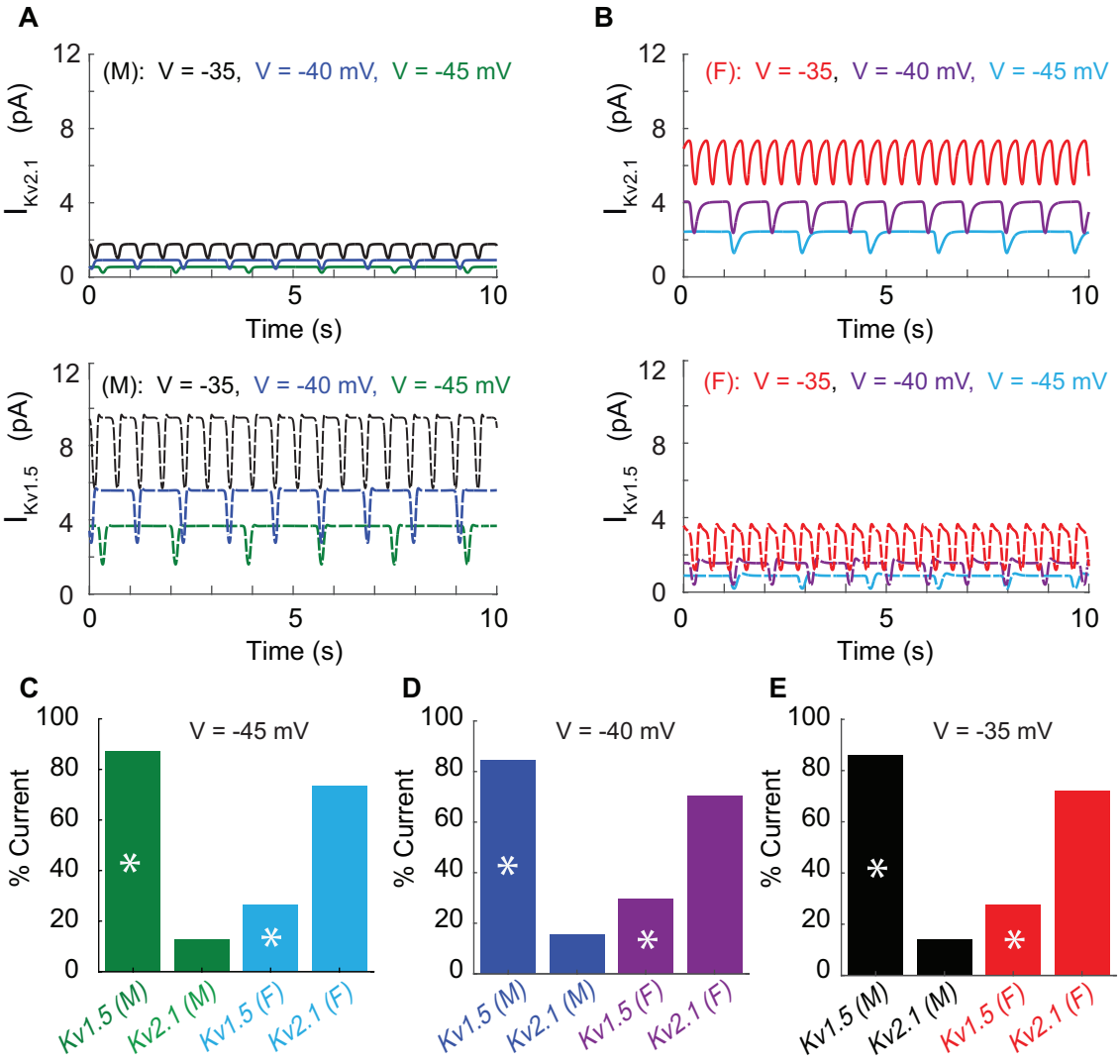

Figure 3.9. Differential effects of voltage-gated potassium current (I_{KVTOT}) block in male and female myocytes. A) Simulated time course of male $I_{Kv2.1}$ (*top panel*) and $I_{Kv1.5}$ (*lower panel*) at three different baseline membrane potentials (-45 mV, -40 mV, and -35mV). B) Simulated time course in female $I_{Kv2.1}$ (*top panel*) and $I_{Kv1.5}$ (*lower panel*) at three different baseline membrane potentials (-45 mV, -40 mV, and -35mV). Current contribution from $K_V1.5$ and $K_V2.1$ at a baseline membrane potential of -45 mV (C), -40 mV (D) and -35 mV (E).

Having explored the regulation of graded membrane potential by the activation of total voltage-gated currents counterbalancing the nonselective cations currents (I_{NSC}), we next explored the effects of steady membrane depolarization in the *in silico* vascular smooth

muscle cell myocyte model on the voltage-gated L-type calcium $Ca_V1.2$ currents in male and female myocytes. We predicted the L-type calcium $Ca_V1.2$ currents in our male and female simulations at steady membrane depolarization after simulation for 500 seconds. We observed that, as the steady membrane depolarization increases, currents in male myocytes increase from 0 to 1.0 pA, while in female myocytes it increases from 0 to 1.5 pA as shown in **figure 3.10A**. In other words, female L-type calcium $Ca_V1.2$ currents are notably larger compared to those of male myocytes. We recorded the predicted cytosolic concentration $[Ca^{2+}]_i$ and observed that L-type calcium $Ca_V1.2$ currents lead to a higher calcium influx in female compared to male simulations as shown in **figure 3.10B**. To illustrate the phenomena we show in **figure 3.10C-D**, time traces of *in silico* predictions of membrane voltage at -40 mV (*top panel*), L-type calcium $Ca_V1.2$ currents (*middle panel*), and cytosolic calcium concentration $[Ca^{2+}]_i$ (*lower panel*). In the male case (**figure 3.10C**), at a steady membrane potential of -40 mV, L-type calcium $Ca_V1.2$ channels produced a current of 0.4 pA, leading to an influx of $[Ca^{2+}]_i$ of 105 nM. However, in female simulations (**figure 3.10D**), we observed that at a steady membrane potential of -40 mV, L-type calcium $Ca_V1.2$ channels produced a current of 0.65 pA of current, leading to an influx of $[Ca^{2+}]_i$ of 123 nM. We calculated that at -40 mV in male myocytes, two open $Ca_V1.2$ channels are needed sustained 0.4 pA of current, while in female three open channels are needed sustained 0.65 pA of current. Although the sex-specific differences in male and female simulations at -40 mV are small, a 15 nM difference in $[Ca^{2+}]_i$ can have a profound effect on the constricted state of the myocytes. The predictions from the VSMC model provide a comprehensive picture of physiological conditions and support the idea that a small number of $Ca_V1.2$ channels supply the steady Ca^{2+} influx needed to

support a maintained constricted state in small arteries and arterioles [20-22]. The differences between males and females are notable in the context of observations indicating varied sex-based responses to antihypertensive agents that target the Ca^{2+} handling system in vascular smooth muscle cells.

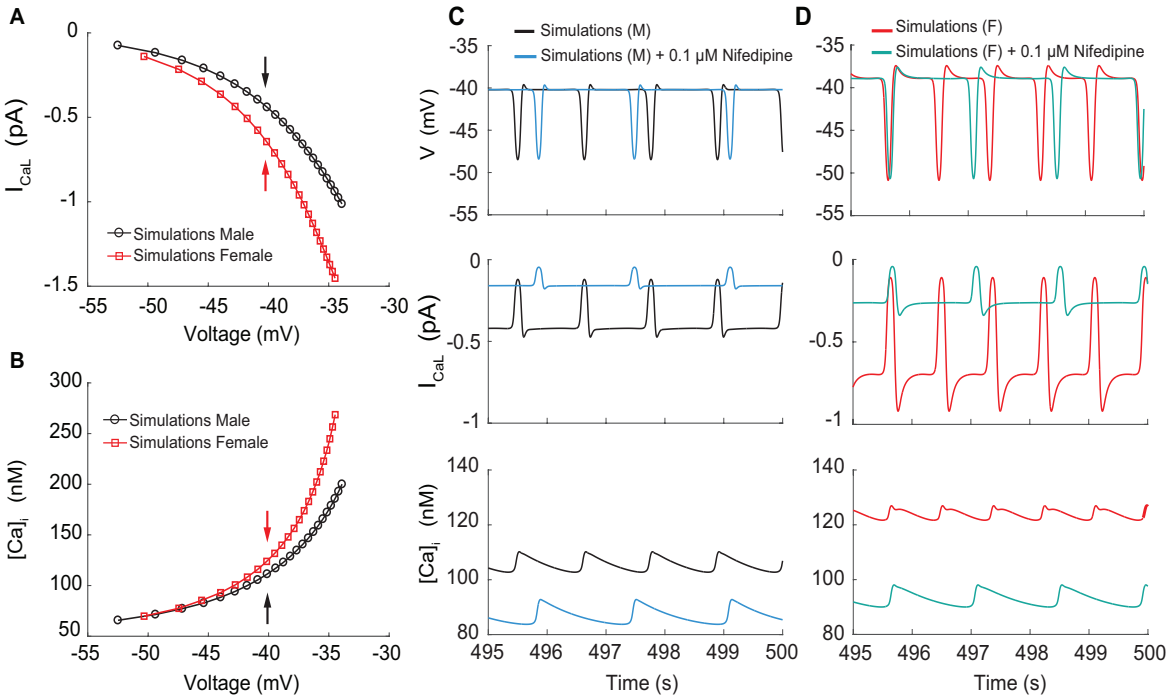

Figure 3.10. Simulated effects of L-type calcium currents ($I_{Cav1.2}$) and calcium influx in male and female vascular smooth muscle cells. A) Male and female whole-cell $I_{Cav1.2}$ membrane potential relationship. (B) Male and female intracellular calcium concentration in the cytosolic compartment at indicated membrane potential. C) Time course of membrane potential in male vascular smooth muscle cells before (black) and after (blue) simulated nifedipine application (*top panel*). Corresponding time course of L-type calcium current $I_{Cav1.2}$ (*middle panel*) and intracellular calcium $[Ca^{2+}]_i$ concentration (*lower panel*). D) Time course of membrane potential in female (*top panel*), L-type calcium current $I_{Cav1.2}$ (*middle panel*), and intracellular $[Ca^{2+}]_i$ concentration (*lower panel*).

Next, we simulated the effects of calcium channel blocker nifedipine on $I_{Cav1.2}$ at a steady membrane potential of -40 mV in male and female simulations. In **figure 3.10C-D**, we show the predicted male (blue) and female (green) time course of membrane voltage at -40 mV (*top panel*), L-type calcium $Ca_V1.2$ currents (*middle panel*), and cytosolic calcium

concentration $[Ca^{2+}]_i$ (*lower panel*). First, we observed that in both male and females 0.1 μM nifedipine modifies the frequency of oscillation in the membrane potential, by causing a reduction in oscillation frequency. Second, both male and female simulations (middle panels) show that 0.1 μM nifedipine caused a reduction of $I_{Cav1.2}$ to levels that are very similar in male and female myocytes following treatment. Consequently, the reduction of L-type calcium $Ca_V1.2$ currents causes both male and female simulations to reach a very similar baseline cytosolic calcium concentration ($[Ca^{2+}]_i$) of about 85 nM (lower panels). As a result, simulations provide evidence supporting the idea that L-type calcium $Ca_V1.2$ is the predominant regulator of intracellular $[Ca^{2+}]$ entry. Importantly, these predictions also suggest that clinically used nifedipine cause larger reductions in Ca^{2+} influx in female than in male arterial myocytes.

In vascular smooth muscle cells, the membrane potential is primarily determined by the potassium (K^+) conductance [22]. Our simulations suggest that K^+ conductance is mainly influenced by voltage-gated potassium $K_V1.5$, $K_V2.1$, and BK_{Ca} channels. In rodent animal models, downregulation of $K_V1.5$ and/or $K_V2.1$, as well as an increase in activity of $Ca_V1.2$ increase intracellular calcium $[Ca^{2+}]_i$ triggering vasoconstriction and cell proliferation. Consequently, vascular smooth muscle cells undergo remodeling leading to the pathogenesis of hypertension. Our modeling and simulation approach allowed us to produce plausible predictions in male and female myocytes regarding the effects of voltage-gated potassium currents in the regulation of membrane potential and intracellular calcium $[Ca^{2+}]_i$.

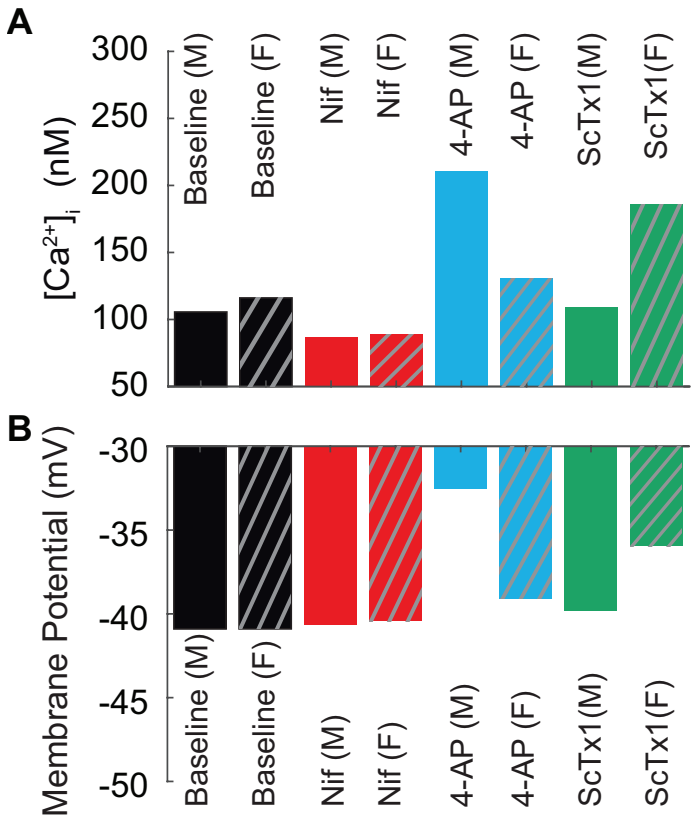

Figure 3.11. Predicted acute responses of membrane potential and intracellular calcium $[Ca]_i$ to selective channel blockers. A) Intracellular calcium $[Ca]_i$ concentration and (B) membrane potential in male (solid) and female (pattern) myocytes at baseline (black) following the selective application of 0.1 uM Nifedipine to block $Ca_V1.2$ channels(red), 5 mM 4-AP to block $K_V1.5$ channels (blue), and 100 nM ScTx1 to block $K_V2.1$ channels (green).

To summarize our results, we set a baseline by changing the conductance of nonselective cationic currents (I_{NSC}) to similar levels in male and female myocytes at -40 mV as shown in the *black bar graphs* in **figure 3.11B**. Here, we provided evidence supporting the hypothesis that differences in the amplitude and voltage dependencies of L-type $Ca_V1.2$ currents in female cause higher Ca^{2+} influx into the cytosol $[Ca^{2+}]_i$ compared to male myocytes. Moreover, our model predictions suggest that female myocytes are more sensitive to $Ca_V1.2$ channel blocker nifedipine as shown in the *red bar graphs* in **figure 3.11A** but have little or no effect on membrane potential **figure 3.11B**. Studies in rodent animal male models [41, 73, 74] have demonstrated that 4-Aminopyridine (4-AP), a

selective channel blocker of $K_V1.5$ channels depolarizes membrane potential. Our model predicts similar behavior in male myocytes as an acute response to 4-AP reduces membrane potential from -40 mV to -32 mV but when similar conditions are applied to female myocytes the response is different as we only observed a 4-mV difference as shown in the *blue bar graphs* in **figure 3.11B**. The corresponding changes to intracellular calcium $[Ca^{2+}]_i$ are in *blue bar graphs* in **figure 3.11A,** in male myocytes $[Ca^{2+}]_i$ increase from 105 nM to 211 nM while in female myocytes there is an increase from 123 to 135 nM. On the other hand, acute response to ScTx1 the selective blocker of $K_V2.1$ channels have almost no effect approximately 2 mV difference in membrane potential in male myocytes but the effect in membrane potential is noticeable in female myocytes as shown in the *green bar graphs* in **figure 3.11B**. As expected, changes in intracellular calcium are more pronounced in female than male myocytes. The results highlight the importance of sex-dependent differences and provide a framework to quantify the contribution of $K_V1.5$ and $K_V2.1$ to I_{KV} which is different in male and female myocytes. Moreover, our model predicts that $K_V2.1$ channels play an unexpectedly primary role in the control of membrane potential in female than in male myocytes.

3.7 Discussion

Here, we present the development, validation, and application of a model to understand the mechanisms of electrical activity and Ca^{2+} dynamics in an isolated mesenteric vascular smooth muscle cell. The computational model is built on new experimental data collected from male and female arterial myocytes that suggest measurable sex-specific

differences in voltage-gated $K_V2.1$ and $Ca_V1.2$ channels and then predicts the effects of those differences on membrane potential and Ca^{2+} signaling.

The “Hernandez-Hernandez” model builds upon earlier models of the vascular smooth muscle cell [53-56]. Because earlier studies have suggested the importance of restricted subcellular junctional spaces to promote tight coupling between Ca^{2+} release via ryanodine receptors (RyRs) and large-conductance Ca^{2+} activated potassium BK_{Ca} channels [75-77], we incorporated a representation of the junctional domain by explicitly describing a subcellular compartment in the model formulation following the mathematical description first introduced by Karlin [57]. The Karlin model endeavored to describe how subcellular junctional spaces influence membrane potential and $[Ca]_i$ in response to intravascular pressure, vasoconstrictors, and vasodilators. In this study, we took a different approach and reduced the complexity of the model representation of subcellular Ca^{2+} signaling spaces to include just three compartments. To specifically investigate the impact of sex-specific differences measured from ion channel experiments and their impact on membrane potential and $[Ca]_i$, we focused on the isolated myocyte in the absence of complex signaling pathways.

We first explored the effects of $Ca_V1.2$ and $K_V2.1$ channels on membrane potential as experimental data suggest key sex-specific differences in channel expression and kinetics. Notably, the peak of the current-voltage (I-V) relationship of L-type $Ca_V1.2$ current ($I_{Cav1.2}$) is 45% larger in female compared to male myocytes (**Figure 3.5D**). In female myocytes, the currents were largest at 0 mV, with a mean current of – 77.4 ± 15

pA. Similarly, currents in male myocytes were largest at 0 mV, with a mean current of -46.2 ± 7.7 pA. O'Dwyer et al. [15] used the ON gating charges ($Q_{onCav1.2}$) values to calculate the number of $Ca_V1.2$ channels expressed in the plasma membrane of mesenteric male and female myocytes. The $Q_{onCav1.2}$ values were similar in male and female myocytes and the combined analysis suggested that the number of $Ca_V1.2$ channels in mesenteric myocytes was 192,612 ± 19,168.

Similarly, the peak current-voltage (I-V) relationship of the voltage-gated $K_V2.1$current ($I_{Kv2.1}$) is 70% larger in female compared to male myocytes at +40 mV (**Figure 3.5D**). Regarding $K_V2.1$ channels, O'Dwyer and coauthors, [15] showed sex-dependent expression in the plasma membrane, where male arterial myocytes have a total of 75,000 ± 21,628 channels compared to 183,000 ± 27,716 channels in female myocytes. Notably, less than 0.01% of channels are conductive in both male and female myocytes. In the computational model, we found that to reproduce the experimentally measured amplitude of the $K_V2.1$ I-V curve (**Figure 3.6C**), a maximum of ~44 male $K_V2.1$ channels was sufficient to reproduce the peak current (68.8 pA at 40 mV). In contrast, ~145 channels were predicted to be needed in female myocytes to reproduce the experimentally measured peak current (226.42 pA at 40 mV) of the I-V relationship.

Model and simulation led to the prediction that $K_V2.1$ currents play a major role in dictating the sex-specific differences observed in I_{KvTOT} (**Figure 3.6F**). Furthermore, our model simulations suggested that in male arterial myocytes, I_{KvTOT} is largely dictated by the $K_V1.5$ channels. In contrast, in female arterial myocytes, $K_V2.1$ channels dominate I_{KvTOT}.

An important observation is that in the physiological range from -60 to -20 mV, we did not observe statistically significant differences in I_{KvTOT} or $I_{Cav1.2}$ among male and female arterial myocytes, yet we observed that small fluctuations based on the distributions of a small number of activated $Ca_V1.2$, $K_V2.1$, and $K_V1.5$ channels can lead to sex-specific emergent differences in membrane potential and calcium signaling.

In the model presented here, Ca^{2+} signaling is described in three main compartments: the cytosol (Cyt), sarcoplasmic reticulum (SR), and the junctional domain (Jun). Junctional domains are the sites where numerous RyR calcium release units cluster in arterial myocytes. However, it has been suggested that under basal physiological conditions only one junctional domain is active in a cell at a time [38]. Within the active junctional domain of a mesenteric myocyte, recent data suggest that Ca^{2+} sparks are caused by the activation of RyR2 subtype in the junction [29]. Ca^{2+} sparks drive an increase in $[Ca^{2+}]$ in the junction that also contains BK_{Ca} channels. The restricted space in the junction allows for rapid changes in the $[Ca^{2+}]_{jun}$ and therefore activation of BK_{Ca} channels. In the computational model presented here, we represented the activity of the RyRs in the junctional domain deterministically, where the opening occurs at a frequency of about 1 Hz in a space equivalent to 1% of the total cell surface area of the plasma membrane [34].

Based on experimental observations, the Hernandez-Hernandez computational model employs three key assumptions: First, Ca^{2+} sparks in the junctional domain that are initiated by activation of RyRs result from RyR gating opening probability that depends on

SR load. Second, Ca^{2+}sparks lead to a $[Ca]_{Jun}$ increase between 10-20 μM, similar to the amplitude measured in experiments (**Figure 3.7A**) [63, 64]. Third, activation of BK_{Ca} channels and the resultant current in the junctional domain derives from the experimentally observed spontaneous outward currents (STOCs) in both amplitude and morphology.

Notably, our model simulations allowed us to reveal important mechanisms underlying observations from experimental measurements of membrane potential (**Figure 3.8A**). The model predicts that the mechanism of intrinsic oscillatory behavior in the vascular myocytes results from a delicate balance of currents. Activation of non-selective cation currents (I_{NSC}) causes membrane depolarization, but the delayed rectifier currents (I_{KvTOT}) oppose them, resulting in membrane potential baseline in the physiological range of -45 to -20 mV. Interestingly, the activation threshold of the voltage-gated L-type $Ca_V1.2$ currents ($I_{Cav1.2}$) sits within this range at -45 mV. Therefore, small increases in I_{NSC} can overwhelm I_{KvTOT} below -20 mV and result in sufficient depolarization to bring the membrane potential to the threshold for activation of $I_{Cav1.2}$. It is important to notice that I_{KvTOT} increases sharply upon depolarization from -45 to -20 mV, resulting in tight control of membrane potential and prevention of large transient depolarization. Activation of L-type Ca^{2+} channels upon depolarization and subsequent Ca^{2+} release within the small volume junction that activates the BK_{Ca} channels results in hyperpolarization. Hyperpolarization then reignites the oscillatory cascade as an intrinsic resetting mechanism.

Experiments show that membrane potential is more depolarized in female compared to male myocytes. The model simulations suggested that sex-dependent differences in the total voltage-gated K^+ (I_{KvTOT}) currents cannot explain such differences, as the I_{KvTOT} currents are not significantly different in the physiological range from -50 to -20 mV in male and female myocytes. However, the simulations also led to a plausible explanation for the observed differences in membrane potential: female myocytes may be more depolarized due to larger non-selective cation currents (I_{NSC}). In the computational model, we were able to readily replicate the baseline membrane potential observed in male and female myocytes by tuning the conductance of I_{NSC}. To reproduce the experimental observations, we increased the conductance of I_{NSC} by 20% in female compared to male myocytes. Since vascular myocytes are subject to substantial noise from the stochastic opening of ion channels in the plasma membrane, and fluctuations in the local junctional domain components, such as the SR load, RyR opening, and BK_{Ca} channel activity, we added noise to the simulation. To simulate the physiological noise in the vascular smooth muscle cell (**Figure 3.8B**), we added Gaussian noise to the dV/dt equations, the dynamics of SR, and the open probability gating of the RyR receptors.

Notably, the Hernandez-Hernandez model predicts that very few channels (based on total current amplitude) are likely to control the baseline fluctuations in membrane potential. The intrinsic oscillatory properties of the vascular myocyte operating in the low voltage regime under conditions of high resistance membrane are similar to other types of oscillatory electrical cells including cardiac pacemaker cells. Indeed, the model predicts

that small changes on the order of those observed between male and female myocytes can lead to notable differences in membrane potential and Ca^{2+} signaling.

Having established the direct effect of I_{KvTOT} in the control of membrane potential baseline and because the contribution of $K_V2.1$ and $K_V1.5$ channels is different in males and females (**Figure 3.9**), the model predicts that at -40 mV in male myocytes, only one $K_V2.1$ channel and four $K_V1.5$ channels are likely activated to reproduce the total current, whereas, in female myocytes, the model predicts three $K_V2.1$ channels and one $K_V1.5$ channel are likely activated. Similarly, we calculated the number of $Ca_V1.2$ channels needed to sustain the steady-state concentration of $[Ca]_i$ in the physiological range from -60 to -20 mV (**Figure 3.10**). The model predicts that at -40 mV in male myocytes, two channels were required to generate 0.4 pA of $Ca_V1.2$ current leading to a $[Ca]_i$ of 105 nM. On the other hand, we found that in female myocytes, three channels were sufficient to generate 0.65 pA of $Ca_V1.2$ current leading to a $[Ca]_i$ of 123 nM. Furthermore, we determined that small fluctuations in the number of $Ca_V1.2$ channels are both necessary and sufficient to account for male and female differences in $[Ca]_i$. Indeed, the model results support the hypothesis that the differences in amplitude and voltage dependencies of L-type calcium $Ca_V1.2$ currents between male and female myocytes cause higher Ca^{2+} influx and $[Ca]_i$.

Importantly, we used the Hernandez-Hernandez model to predict the cellular mechanisms and sex-specific responses of $K_V2.1$ and $Ca_V1.2$ channels in the presentation and treatment of hypertension. It is established that in mesenteric arteries, downregulation of

$K_V1.5$ and/or $K_V2.1$, as well as an increase in activity of $Ca_V1.2$ channels are key determinants of the pathogenesis leading to hypertension [35, 78-80]. The Hernandez-Hernandez model confirms previous suggestions [41, 73, 74, 81] regarding the importance of $K_V1.5$ (4-AP sensitive) channels in the regulation of membrane potential in rodent male animal models. However, the model predicted that such results are not applicable in female myocytes. In fact, we found using selective acute channel block that $K_V2.1$ channels play the dominant role in female myocytes in regulating membrane potential (**Figure 3.9**). Regarding, $Ca_V1.2$ channels, simulations forecast the clinically relevant concentrations (0.1 uM) at which Ca^{2+} channel blockers (e.g., nifedipine) effectively block $Ca_V1.2$ channels in both male and female myocytes (**Figure 3.10**). The Hernandez-Hernandez model provides a computational framework and the first step towards the development of a virtual drug-screaming system that can model drug-channel interactions in vascular myocytes.

To conclude, we developed and present the Hernandez-Hernandez model of male and female isolated mesenteric vascular myocytes. The model was informed and validated with male and female vascular myocytes experimental data. We then used the model, to reveal sex-specific mechanisms of $K_V2.1$ and $Ca_V1.2$ channels in controlling membrane potential and $[Ca]_i$ dynamics. In doing so, we predicted that very few channels are needed to contribute to and sustain the oscillatory behavior of the membrane potential and calcium signaling. We then used the model to make predictions of the effects of antihypertensive drugs in vascular myocytes. The model predictions suggested differences in the response of male and female myocytes to drugs and the underlying

mechanisms for those differences. These predictions may constitute a first step towards better hypertensive therapy for males and females.

3.8 Limitations

There are several limitations present in our study. First, the model presented here describes the necessary and sufficient ion channels, pumps, and transporters to describe the electrical activity and calcium signaling of an isolated mesenteric smooth muscle cell in the absence of complex signaling pathways. Such an approach enabled us to perform a component dissection to analyze the sex-specific differences observed in the electrophysiology of male and female myocytes. However, it is well known that vascular smooth muscle cells are subject to a plethora of stimuli from endothelial cells and neurotransmitter endocrine and paracrine signals [57]. We are undertaking an expansion of the model in our immediate plans.

Second, the generation of signals to promote constriction or relaxation of smooth muscle are regulated through focal increases in intracellular Ca^{2+} concentration within specialized cellular microdomains [34, 38, 82]. In our model, we included a junctional domain to localize the activity of the RyRs and BK_{Ca} channels and assumed a single junctional domain to be active under physiological conditions following experimental observations [38]. However, the recruitment of multiple junctional domains is necessary to describe calcium signaling effects through stimulations of complex signaling pathways. Therefore, future computational studies must include the effects of multiple junctional domains. It has also been suggested that calcium-activated chloride channels are important in the

regulation of smooth muscle function through the activation of signaling pathways and or specialized microdomains [83], but we have not included them in this first model presentation.

Third, excitation-contraction coupling refers to an electrical stimulus that drives the release of calcium from the sarcoplasmic reticulum and results in the physical translocation of fibers that underlies muscle contraction. In the present model, we did not explicitly consider the mechanical description of muscle contraction. Nevertheless, we can imply its effects by tracking membrane potential and the elevation of calcium in the cytoplasm ($[Ca^{2+}]_{i.}$) as a proxy.

Ultimately, The Hernandez-Hernandez model focus on the sex-dependent differences measured in the in the voltage-gated K^+ currents (I_{KvTOT}) and the voltage-gated L-type Ca^{2+} current $Ca_V1.2$ ($I_{Cav1.2}$) in mesenteric isolated myocytes. One of the assumptions of our model is that pumps and transporters are important in calcium signaling such as the sodium-potassium pump (NaK), sodium-calcium exchanger (NCX) the sarcolemma calcium pump (PMCA) remain the same in male and female myocytes. Our model will complement future experimental research to determine if important sex-dependent mechanisms exist in the expression and function of pumps, and transporters.

3.9 Summary and key findings

a) Experimental data indicate that female membrane potential is more depolarized than male myocytes. Modeling and simulation were used to suggest that membrane

potential in vascular smooth muscle myocytes is regulated by the balance of voltage-gated potassium currents (I_{KvTOT}) and the nonselective cation currents (I_{NSC}). Simulations also predict that nonselective cation currents are larger in female compared to male vascular smooth muscle myocytes.

b) The contribution to total current (I_{KvTOT}) from $K_V1.5$ and $K_V2.1$ channels varies between male and female myocytes. While total current (I_{KvTOT}) is dominated by $K_V1.5$ channels in male vascular smooth muscle myocytes, KV2.1 channels play the dominant role in female myocytes. Predictions from the computational model suggest that $K_V2.1$ current is a more potent regulator of membrane potential in female myocytes.

c) Modeling and simulation predict that the larger L-type calcium currents ($I_{Cav1.2}$) observed experimentally in female myocytes results in larger calcium influx and higher maximal intracellular [Ca^{2+}] = 300 nM compared to male myocytes [Ca^{2+}] = 200 nM. This occurs because within the physiological range of -45 to -20 mV, measured female calcium currents ($I_{Cav1.2}$) are up to 3x larger than male calcium currents ($I_{Cav1.2}$).

d) The Hernandez-Hernandez model of VSMCs predicts that the large-conductance Ca^{2+} sensitive K^+ (BK_{Ca}) channels comprise the key membrane potential resetting mechanism by periodically repolarizing the membrane potential and deactivating voltage-gated depolarizing channels. In doing so, the BK_{Ca} channels serve as a key mechanism to regulate calcium cycling and intracellular $[Ca^{2+}]_i$ concentration.

e) The Hernandez-Hernandez model constitutes a framework to quantitatively assess the cellular mechanisms underlying the reported differences in male and female responses to antihypertensives.

Chapter 4: A stochastic model of ion channel formation in the plasma membrane of vascular smooth muscle cells

Acknowledgements: This chapter is comprised of the following published paper: Sato D et al. A stochastic model of ion channel cluster formation in the plasma membrane. Originally published in J Gen Physiol. 2019 Sep 2;151(9):1116-1134. doi: 10.1085/jgp.201912327.

4.1 Abstract

Ion channels are often found arranged into dense clusters in the plasma membranes of excitable cells, but the mechanisms underlying the formation and maintenance of these functional aggregates are unknown. Here, we tested the hypothesis that channel clustering is the consequence of a stochastic self-assembly process and propose a model by which channel clusters are formed and regulated in size. Our hypothesis is based on statistical analyses of the size distributions of the channel clusters we measured in arterial smooth muscle as well as heterologous cells, which in all cases were described by exponential functions, indicative of a Poisson process, i.e., clusters form in a continuous, independent, and memory-less fashion. We were able to reproduce the observed cluster distributions of three different types of channels in the membrane of excitable and tsA-201 cells in simulations using a computer model in which channels are 'delivered' to the membrane at randomly assigned locations. The model's three parameters represent channel cluster nucleation, growth, and removal probabilities, the values of which were estimated based on our experimental measurements. We also determined the time course of cluster formation and membrane dwell time for $Ca_V1.2$ and TRPV4 channels expressed in tsA-201 cells to constrain our model. In addition, we elaborated a more complex version of our model that incorporated a self-regulating, feedback mechanism to shape channel cluster formation. The strong inference we make from our results is that

$Ca_V1.2$, BK, and TRPV4 proteins are all randomly inserted in the plasma membranes of excitable cells and that they form homogeneous clusters that increase in size until they reach a steady-state. Further, it appears likely that the regulation of cluster size for both a diverse set of membrane-bound proteins and a wide range of cell types is regulated by a common feedback mechanism.

4.2 Introduction

Cell biologists have been studying the mechanisms of ion channel expression and delivery to the membrane for decades. This work has revealed key roles for the cytoskeleton, channel subunits, scaffolding proteins, and/or lipid microdomains (e.g., caveolae) in the organization of ion channels in the plasma membrane [84-89]. The process starts when messenger RNA encoding the transmembrane ion channel subunits is translated on endoplasmic reticulum (ER)-bound ribosomes from which the nascent polypeptides are translocated into the membrane. Fully assembled channel proteins leave the ER in vesicles that fuse with the *trans* Golgi, where they undergo post-translation processing, including, for many ion channel subunits, modification of N-linked glycosylation. These vesicles are transported as cargo by molecular motors traveling along microtubules that run from the *cis* side of the Golgi apparatus to the cytoplasmic surface [89, 90]. Ion channels appear on the cell surface upon fusion of these vesicles with the plasma membrane, which, depending on the ion channel and cell type, can occur at proximal sites or, in some cases, quite distant from where the vesicles emerged from the Golgi apparatus. Plasma membrane ion channels are eventually removed and either recycled or degraded via endocytic pathways.

The organization of ion channels has long been recognized to vary along a cell's membranous surface [91-94]. Descriptions of the distributions of ion channels in the plasma membrane have been based on the analysis of electron micrographs[93-97], confocal images of cells exposed to protein-specific antibodies attached to fluorescent moieties [98], and, more recently, super resolution imaging [26, 99-103]. In most instances, it has been shown that many ion channels aggregate into dense clusters. For example, in neurons, ligand-gated ion channel proteins involved in synaptic transmission are concentrated on the dendritic and somatic membranes[104], whereas the voltage-gated ion channels required for the release of neurotransmitter are restricted to the axon terminals [91, 92, 95, 105]. In striated muscle, dihydropyridine-sensitive voltage-gated Ca^{2+} channels form clusters along the sarcolemma and transverse tubules of the cells [94-96]. Such exquisite spatial arrangements of ion channels are critical for efficient biological functions in both neurons and muscle. Indeed, clustering of voltage-gated Ca^{2+} channels is critical for the amplification of Ca^{2+} influx that is necessary to initiate neurotransmitter release in neuronal terminals and to sustain excitation-contraction coupling in muscle. Furthermore, it has recently been demonstrated that proteins engaged in cooperative signaling cascades display co-clustering, e.g., clusters of large conductance Ca^{2+}-activated K^+ (BK) channels are surrounded by clusters of $Ca_V1.3$ channels that generate the requisite local Ca^{2+} influx [99, 106]. Yet, despite these advances, a broadly applicable quantitative model that amalgamates key concepts of ion channel insertion and organization in mammalian cells is lacking.

We gain some insight on the mechanisms underlying channel cluster formation from studies performed in bacteria, where time-lapse fluorescence images suggest that chemoreceptor proteins are inserted randomly into the membrane via the general protein translocation machinery of the cells and then diffuse to existing clusters [107]. The distance between clusters, however, varied widely within cells, prompting [108] to propose that protein cluster formation and growth is a stochastic self-assembly process in which newly synthesized proteins diffuse in the membrane and then join existing clusters or create new clusters. In their model, clusters can originate anywhere in the membrane and later become attached to scaffolding or anchoring sites. Shortly thereafter, it was reported that anchoring sites may not be required for the formation of new clusters and their simulations suggested that the periodic positioning of new clusters can emerge spontaneously in growing cells [109]. At present, however, it is unclear whether the distribution of ion channels in the surface membrane of mammalian cells could be the result of a similar stochastic self-assembly process of protein organization.

In the work described here, we used super-resolution fluorescent microscopy to determine the sizes and densities of clusters of five different ion channel proteins expressed in the surface membranes of smooth muscle cells ($Ca_V1.2$, TRPV4, and BK channels) and tsA-201 cells ($Ca_V1.2$ and TRPV4 channels). We found that the probability density functions of the cluster sizes of all of these ion channels could be fit with an exponential function, a hallmark of a Poisson process. Thus, we generated a mathematical model in which vesicles containing ion channel proteins are inserted into the membrane at random locations. The model reproduced the observed steady-state

clustering of $Ca_V1.2$, TRPV4, and BK channels in the membranes of smooth muscle, and tsA-201 cells. To further elaborate and constrain our model, we studied the formation and growth of clusters of $Ca_V1.2$ and TRPV4 channels expressed in tsA-201 cells, as well as the turnover rate of these channels in the membrane. We found that adding a regulatory feedback mechanism scaled to channel number enhanced its capacity of the model to reproduce our experimental observations. On the basis of our experimental and modeling results, we propose that the regulation of cluster size for both a diverse set of membrane-bound proteins and a wide range of cell types is regulated by a common feedback mechanism. Our model constitutes a novel tool for identifying potential mechanisms by which specific proteins and signaling pathways could dynamically shape membrane channel cluster formation.

4.3 Methods

4.3.1 Immunofluorescence and super resolution microscopy

We performed immunofluorescence and super resolution imaging experiments using methods similar to those described elsewhere [26, 99-102, 110]. Briefly, cells were fixed at the specified times after transfection by incubating in phosphate-buffered saline (PBS) containing 3% paraformaldehyde and 0.1% glutaraldehyde (GA) for 10 minutes at room temperature. After washing with PBS, cells were incubated with sodium borohydride (1 mg/ml) for 10 minutes at room temperature, washed again with PBS, and blocked by incubating in 3% bovine serum albumin and 0.25% v/v Triton X-100 in PBS for 1 hour at

room temperature (≈20 ºC). The cells were incubated either overnight at 4˚C or for 1 hour at room temperature with anti-GFP antibody conjugated to Alexa Fluor 647 (Thermo Fisher, #A-31852) diluted in blocking buffer to a concentration of 10 µg/ml. After washing with PBS, samples were post-fixed with 0.25% GA in PBS for 10 minutes at room temperature, washed with PBS and prepared for imaging.

Coverslips were mounted on microscope slides with a round bottom cavity (NeoLab Migge Laborbedarf-Vertriebs GmbH, Germany), using fresh MEA-GLOX imaging buffer. The day of the experiment a stock of 5 ml of 100 mM MEA (cysteamine hydrochloride, Sigma-Aldrich #M6500) in PBS was prepared and pH was adjusted to 8.2 with KOH, 10M. A stock of GLOX containing 50 µl of 10 mM Tris-HCl pH 8, 3.5 mg glucose oxidase (Sigma-Aldrich #G2133), and 12.5 µl of catalase (Sigma-Aldrich C100) was prepared, sonicated for 5 minutes and centrifuged for 3 minutes at 13000 rpm at 4˚C. This stock was kept at 4˚C and used within a week. Finally, 50 ml of Buffer B, containing 200 mM Tris-HCl pH 8, 10 mM NaCl, and 10% w/v glucose was prepared, kept at 4˚C, and used within 6 months. Right before mounting the coverslip the final MEA-GLOX buffer was mixed by adding a ratio of 89:10:1 of Buffer B: MEA: GLOX. Final concentration of the components in this imaging buffer were 10 mM MEA, 0.56 mg/ml glucose oxidase, and 34 µg/ml catalase. Coverslips were sealed with Twinsil (Picodent, Germany) and aluminum tape to reduce oxygen permeation.

Super-resolution images were generated using a super-resolution ground-state depletion system (SR-GSD, Leica) equipped with high-power lasers (488 nm, 1.4 kW/cm^2; 532 nm,

2.1 kW/cm^2; 642 nm, 2.1 kW/cm^2) and an additional 30 mW, 405 nm laser. Images were obtained using a 160× HCX Plan-Apochromat (NA 1.43) oil-immersion lens and an EMCCD camera (iXon3 897; Andor Technology). For all experiments, the camera was running in frame-transfer mode at a frame rate of 100 Hz. Fluorescence was detected through Leica high-power TIRF filter cubes (488 HP-T, 532 HP-T, 642 HP-T) with emission band-pass filters of 505-605 nm, 550-650 nm, and 660-760 nm.

Super-resolution localization images were reconstructed using the coordinates of centroids obtained by fitting single-molecule fluorescence signals with a 2D Gaussian function using LASAF software (Leica). A total of 35,000 images were used to construct the images. The localization accuracy of the system is limited by the statistical noise of photon counting. Thus, assuming the point-spread functions are Gaussian, the precision of localization is proportional to DLR/√N, where DLR is the diffraction-limited resolution of a fluorophore and N is the average number of detected photons per switching event [111, 112]. Accordingly, we estimated a lateral localization accuracy of 16 nm for Alexa 647 (≈1900 detected photons per switching cycle).

4.3.2 tsA-201 cell transfections

tsA-201 cells (Sigma-Aldrich) were cultured in Dulbecco's Modified Eagle Medium (DMEM; Gibco) supplemented with 10% fetal bovine serum and 1% penicillin/streptomycin at 37˚C in a humidified 5% CO_2 atmosphere. Cells were plated onto 25 mm round 1.5 coverslips and transiently transfected using jetPEI (Polyplus Transfection). For the $Ca_V1.2$ experiments, cells were transfected with plasmids

encoding the rabbit $Ca_V1.2$ (α_{1C}) conjugated to (600 ng), and rat auxiliary subunits $Ca_V\alpha_2\delta$ (300 ng), and $Ca_V\beta_3$ (600 ng), (kindly provided by Dr. Diane Lipscombe; Brown University, Providence, RI). For the TRPV4 experiments cells were transfected with 600 ng of a plasmid encoding the mouse TRPV4-EGFP (kindly provided by Dr. Philipp Slusallek, Saarland University, Saarbrücken, Germany) in which the GFP moiety has been mutated to prevent oligomerizarion. For photoactivation experiments, cells were transfected with $Ca_V1.2$ tagged at their C-terminus with photoactivatable GFP (GenScript, 600 ng) and auxiliary subunits stated above or TRPV4 tagged at their C-terminus with photoactivable GFP (GenScript, 600 ng).

4.3.3 Time-lapse confocal microscopy

The live-cell imaging of photoactivatable experiments were performed on an Olympus Fluoview 3000 (FV3000) confocal laser-scanning microscope equipped with an Olympus PlanApo 60x/1.40 NA oil-immersion objective. We used 405 nm laser light to photoactivate the PA-$Ca_V1.2$ and PA-TRPV4 channels. Pre-stimulation images were collected in order to normalize fluorescence signal. Upon excitation, robust GFP fluorescence emission was observed. Normalized fluorescence time courses were compiled by averaging line scans of various ROIs from each cell. Regions of interest were resliced and quantified over time.

4.3.4 Stochastic self-assembly model

To simulate the aggregation process of channels within cell membranes, we developed a simplified stochastic self-assembly model of cluster growth modified from stochastic self-assembly algorithms proposed for bacterial proteins and ryanodine receptors [103, 109, 113]. As was done by [26] for ryanodine receptors, our model does not consider channel diffusion for cluster formation. The observation that voltage-gated Na^+ channels in the sarcolemma of skeletal muscle fibers are immobile, suggests that lateral channel diffusion, at least in native muscle cells, may not be a significant determinant of cluster growth [114].

In our model, the cell membrane is represented by a 10 x 10 μm virtual two-dimensional square grid ($Grid_{ij}$). This space is subdivided into 10^6 'grid sites', each of which measures 10 x 10 nm and represents the space that can be occupied by an individual ion channel molecule. Particles simulating ion channels were inserted randomly into the grid with cluster growth and density determined by three model parameters representing nucleation (P_n), growth (P_g), and removal (P_R) probabilities.

We first assume that at time t = 0 there are no channels present in the grid ($Grid_{ij}$=0). Then, in each iteration, there are three processes: (1) nucleation, (2) cluster growth, (3) removal.

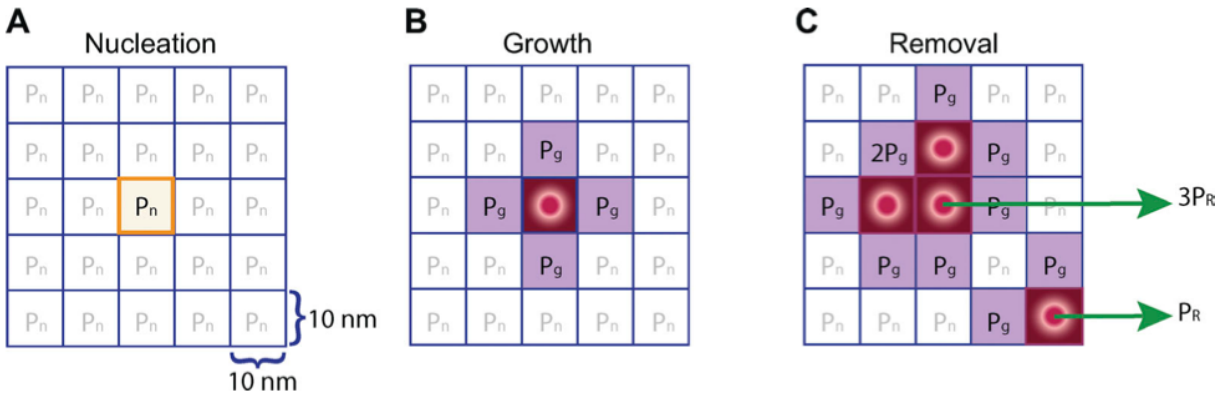

***Figure 4.1. In silico* stochastic self-assembly model.** (**A**) Nucleation process. Channels are inserted into the grid randomly with nucleation probability P_n at each time step. '1' represents occupied grid sites. (**B**) If a nucleating channel exists, channels are randomly inserted into any one of the four available grid sites immediately adjacent to the nucleating channel with growth probability P_g at each time step. (**C**) After that, the growth probability of a cluster is P_g × the number of available neighbors. Clusters are randomly removed with the removal probability, P_R × the number of channels.

(1) Nucleation. Channels are inserted into the grid randomly with nucleation probability P_n at each time step (**Figure 4.1A**). In this study, each iteration is equal to 18 seconds. Cluster growth. If a grid site becomes occupied by a channel ($Grid_{ij}$ =1) cluster growth is induced.

(2) For simplicity, cluster growth is simulated by random insertion of a channel in any one of the four available grid sites immediately adjacent to a nucleating channel with growth probability P_g at each time step (**Figure 4.1B**). Once one channel is added to the existing nucleating channel, a cluster is formed. After that, the growth probability of a cluster is P_g x the number of available neighbors.

(3) Removal of clusters. Concurrently with growth, in each time step, there is a removal probability, P_R, for clusters already formed on the grid. It is important to note that we

have defined a cluster to be a group of two or more channels. Clusters dwell in the membrane for some time before they are recycled or degraded. Therefore, the removal probability, P_R, of a cluster increase depending on its size ($P_R \times the\ number\ of\ channels$) (**Figure 4.1C**). Because clusters will grow until they are recycled or degraded the removal probability sets a limit for maximal cluster size.

The parameters P_n, P_g, and P_R were specified using two methods. In the first, we defined probabilities P_n (t), P_g (t), and P_R (t) . The probabilities P_g (t) and P_n (t) were defined to be sigmoid functions based on a correlation between the experimental fitting of mean cluster area and density and P_g and P_n, respectively. In addition, P_R was defined to be an increasing sigmoid function to account for the observation that $Ca_V1.2$ channel internalization increases as the number of channels increases [115]. These parameters were based on the experimental data using the time course of the distribution of cluster sizes and the values were determined by a non-linear least-squares method (**Figures 4.4-4.5; Table 4.1**).

	K_n	K_g	K_R	r_n	r_g	r_R	Initial P_n	Initial P_g	Initial P_R
$Ca_V1.2$	0.00045	0.07	0.001166667	0.000002	0.0018	0.0003	0.000000225	0.004375	0.00019444
TRPV4	0.00045	0.07	0.001166667	0.000002	0.0005	0.0003	0.000005921	0.004375	0.00010606

Table 4.1. Feedback model parameters and initial conditions.

In our second method, the parameters P_n, P_g, and P_R have a feedback mechanism. In this feedback model, $Ca_V1.2$ and TRPV4 expression is regulated by the number of channels. In this study, P_n, P_g, and P_R linearly increase or decrease until they reach

steady state values. Then, the basic feedback model is described by the following differential equations,

where r_n, r_g, and r_R are growth rates of P_n, P_g, and P_R, respectively, and K_n, K_g, and K_R are steady state values of P_n, P_g, and P_R , respectively, and N is the number of channels per unit area.

4.4 Results

Over the last five years, our research team has been using super-resolution imaging to determine the spatial organization of Ca^{2+}-permeable and Ca^{2+}-sensitive ion channels in the surface membrane of smooth muscle cells and other cell types. In this paper, we focused on determining the spatial organization $Ca_V1.2$ channels and the large-conductance Ca^{2+}-activated K^+ (BK) channels in the sarcolemma of arterial myocytes. We found that the $Ca_V1.2$ channels were expressed into dense clusters of different size along the surface membrane with a mean cluster area 2488 $\pm$ 140 nm^2, similar to that we found in ventricular myocytes (2555 $\pm$ 82 nm^2; [100](**Table 4.2**). The BK channels also formed clusters along the sarcolemma of the arterial myocytes with a mean cluster area of 3008 $\pm$ 223 nm^2.

Ion channel	Cluster area (nm^2)	Cluster density (clusters/μm^2)
Smooth muscle		
$Ca_V1.2$	2488 ± 140	9.7 ± 0.4
TRPV4	1834 ± 117	7.8 ± 0.2
BK	3008 ± 223	9.2 ± 0.5
*tsA-201 cells**		
$Ca_V1.2$	1566 ± 148	54.6 ± 5.7
TRPV4	1605 ± 212	73.4 ± 8.9

Table 4.2. Summary of experimental super-resolution data (**48 hours after transfection*)

Figure 4.2 displays samples of the super-resolution images we have generated for five different channel proteins (BK**,** $Ca_V1.2$, TRPV4) in arterial myocytes, and tsA-201 cells. In each case, we found that the channels are arranged into dense clusters with a wide range of sizes throughout the cell membranes. In the same figure, we have plotted the frequency distributions of cluster sizes for each of our data sets that remarkably reveal that each can be fit by a single exponential function.

Our finding that the size distributions of clusters for five different channel proteins could all be described by exponential functions, the hallmark of a Poisson process, strongly suggested that the clusters are formed stochastically in a continuous, independent, and memory-less fashion. A similar proposal was advanced by [109] and [113] to account for the spatial organization of chemotactic proteins in bacterial membranes and by [103] for ryanodine receptors in ventricular myocytes. To test our hypothesis, we modified the approach employed by [103] to create a new model to reproduce our cluster distributions and make testable predictions regarding plasma membrane protein organization.

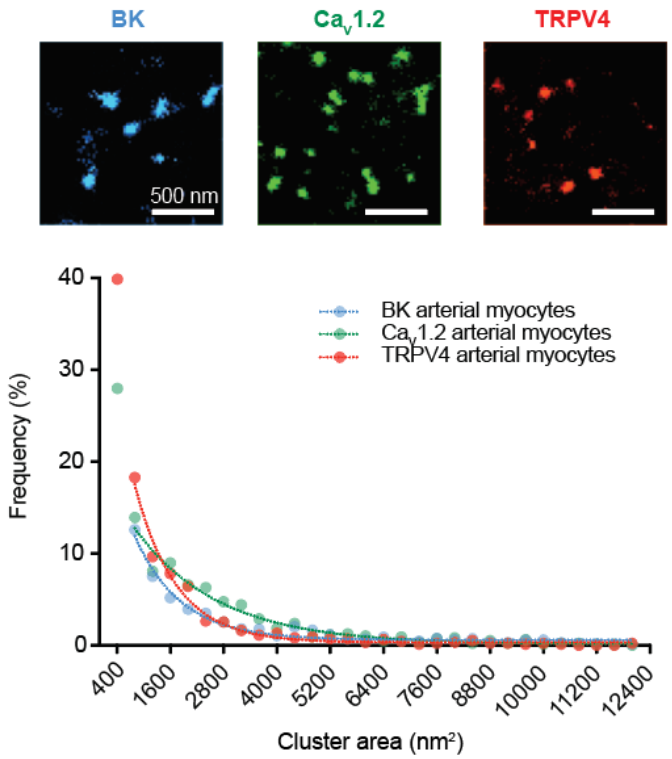

Figure 4.2. Channel clustering. BK, $Ca_V1.2$, and TRPV4 channels organize in clusters in multiple arterial myocytes exhibiting an exponential cluster area distribution.

Our modeling begins with the generation of a 10 x 10 μm grid composed of 10^6 pixels. The dimension of each pixel (100 nm^2) in this grid is similar to the size of individual Ca_V1 [116] and TRPV4 channels [117]. Particles simulating ion channels were inserted randomly into the grid with cluster growth and density determined by three model parameters representing nucleation (P_n), growth (P_g) and cluster removal (P_R). These parameters are probability functions meant to represent different biological processes. P_n is the probability that a vesicle containing an ion channel (or channels) will be randomly inserted at any site in the membrane. Nucleation is the first step in the formation of a new structure via self-assembly or self-organization. In our model, P_n values are uniform across the grid. At the beginning of the simulation, most "seeding" events involve the

insertion of single channels. However, once cluster growth has initiated, the model allows for the stochastic insertion of multiple channels at any particular site. P_g is the probability of a channel to be inserted immediately adjacent to pre-existing channels. In our model, cluster growth is simulated by random insertion of a channel in any one of the four available grid sites immediately adjacent to a nucleating channel. The growth probability of a cluster is Pg×the number of available neighbors. Once a channel or small cluster is "seeded" in the membrane, the probability of insertion of a new channel adjacent to it increases, inducing cluster growth. The final parameter, P_R, represents the probability of a channel or cluster of channels being removed from the membrane by endocytosis and/or degradation. Individual channels and clusters were randomly removed every iteration.

The key question was whether or not this simple model could reproduce the cluster area distributions we measured from our super-resolution images of endogenous channels in arterial myocytes, cardiomyocytes, hippocampal neurons, as well as channels expressed exogenously in tsA-201 cells. Because we could not observe the formation of the channel clusters as the cells develop, we assumed that the cluster area and density distributions we measured represented steady-state conditions and set the parameters P_n, P_g, and P_R to constant values.

As shown in **Figure 4.3,** our stochastic self-assembly model effectively reproduced the steady-state size distributions and mean cluster areas that we measured for all five channels proteins embedded in the membrane of four different cell types: arterial myocyte

BK channels (**Figure 4.3A**), arterial myocyte $Ca_V1.2$ channels (**Figure 4.3B**), arterial myocyte TRPV4 channels (**Figure 4.3C**).

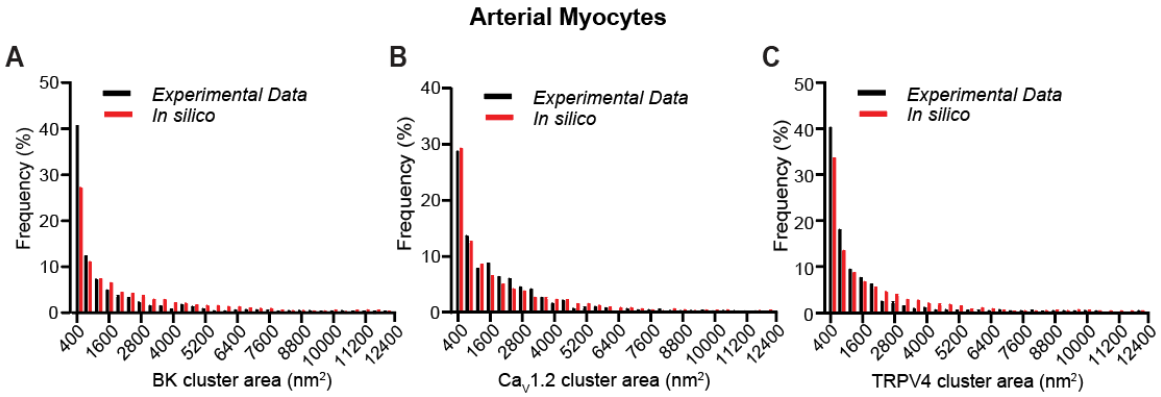

Figure 4.3. The distributions of $Ca_V1.2$, TRPV4, and BK channels in smooth muscle cells could be explained by the stochastic self-assembly of clusters. Histograms of the experimental (black bars) and simulated (red bars) clusters area distributions of (**A**) BK, (**B**) $Ca_V1.2$, and (**C**) TRPV4 channels in arterial myocytes.

As mentioned above, the super-resolution images from which we measured channel cluster sizes and densities present only a snapshot of the cell membrane. We had no information as to how the channel clusters develop and are maintained over time. To address this issue, we expressed $Ca_V1.2$-EGFP (**Figure 4.4**) or TRPV4-EGFP channels (**Figure 4.5**) in tsA-201 cells, fixed the cells at 0, 4, 6, 12, 24, 36, and 48 hours after transfection, immunolabeled the channels, and acquired super-resolution images of the channels in the membrane. These images permitted us to determine how the distribution of channel cluster sizes changed over a 48 hour period. In **Figure 4.4A**, we show super-resolution images of a tsA-201 cell at different time points following transfection with the $Ca_V1.2$-EGFP plasmid. The images were analyzed to quantify the area and densities of the $Ca_V1.2$ channel clusters (**Figure 4.4B-E**). The frequency histograms of cluster areas were generated from the images acquired at each time point. This analysis revealed that

although the number of clusters varied with time, the size distributions could all be fit with single exponential functions that differed mainly in their amplitude (**Figure 4.4B**). Accordingly, histograms generated using the percentage of total clusters within each bin of cluster area were similar (**Figure 4.4C**). These data reveal that the mean size of the $Ca_V1.2$ clusters within the population of tsA-201 cells increased rapidly over the first 12 hours post-transfection and then reached a plateau at about 24 hours (**Figure 4.4D**). These data could be fit with exponential functions with a half amplitude ($T_{1/2}$) at 5.8 hours after transfection. $Ca_V1.2$ cluster density, like mean cluster area, also reached a plateau by about 24 hours and was could be fit with a sigmoidal function with a half amplitude at 11.5 hours (**Figure 4.4E**).

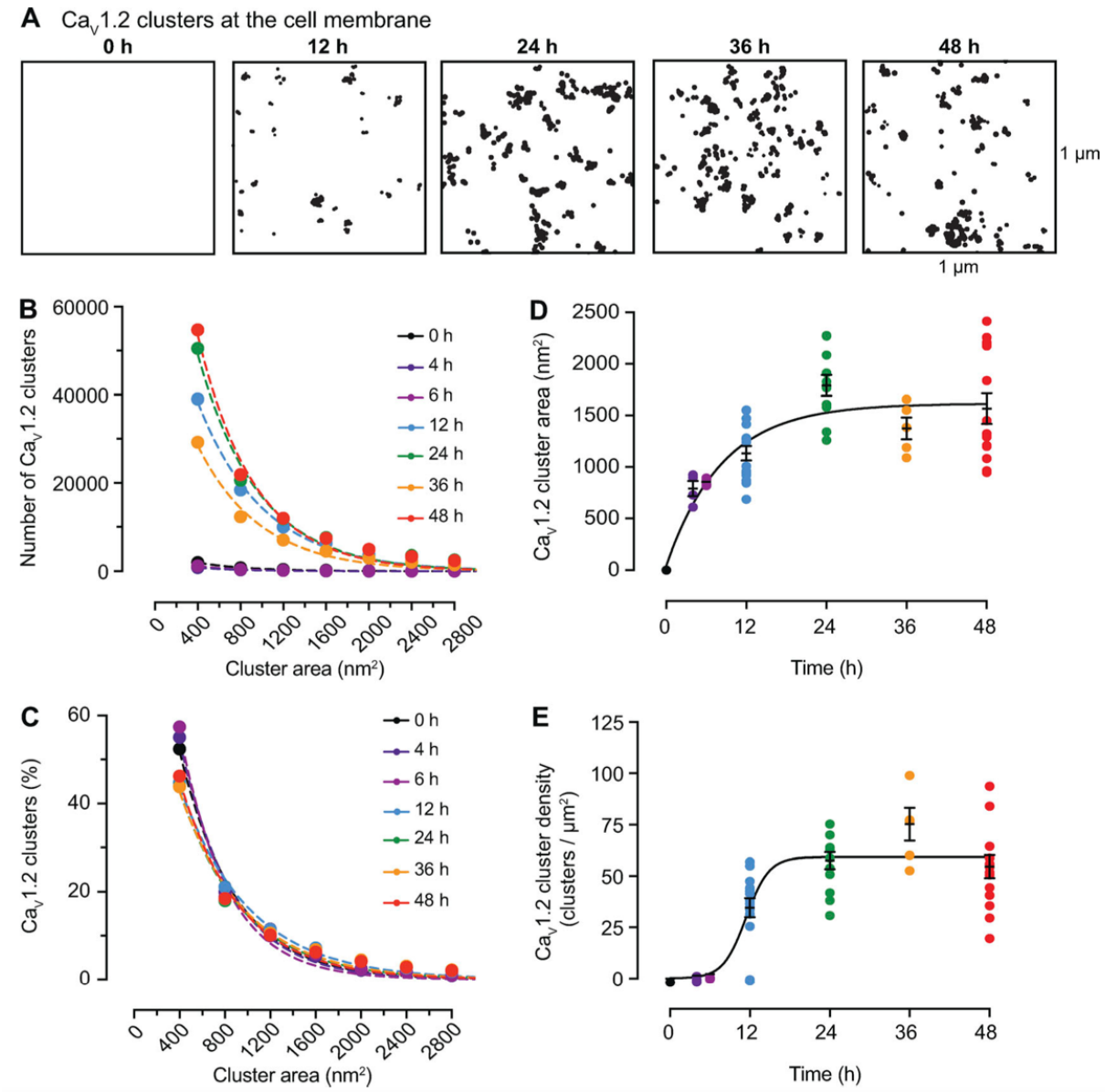

Figure 4.4. Time course of the formation of $Ca_V1.2$ channel clusters in tsA-201 cells. (**A**) Representative super-resolution GSD binary masks of immunolabeled $Ca_V1.2$ channels expressed in tsA-201 cells at 0, 12, 24, 36, and 48-hours post transfection. (**B**) Frequency distribution of $Ca_V1.2$ channels cluster areas at each time point. (**C**) Relative frequency distribution of $Ca_V1.2$ channels cluster areas expressed as percentages. Dashed color lines in **B** and **C** represent the best single exponential decay function fit for each data set. (**D**) Change of mean $Ca_V1.2$ channel cluster area at different time points post transfection, data is presented as mean ± SEM for individual cells at each time point. Mean cluster area data was fit with a one phase exponential equation (solid black line). The tau value of the fit is 8.37 hours. (**E**) Change of $Ca_V1.2$ channel cluster density at different time points post transfection. Data is presented as mean ± SEM for individual cells at each time point. Mean cluster density data was fit with a sigmoidal function (solid black line). The $logIC_{50}$ fit is 11.42 hours. (**B-E**) All data was compiled as followed: 4h: n = 1,497 clusters from 4 cells, 6h: n = 2,100 clusters from 4 cells, 12h: n = 87,209 clusters

from 16 cells, 24h: n = 114,805 clusters from 11 cells, 36h: n = 66,769 clusters from 5 cells, 48h: n = 118,281 clusters from 13 cells.

In **Figure 4.5A**, we show super-resolution images of representative tsA-201 cells at 0, 12, 24, 36, and 48 hours after transfection with the TRPV4-EGFP plasmid. As was the case for $Ca_V1.2$ channels, the sizes of the TRPV4 clusters followed exponential distributions at each time point (**Figure 4.5B-C**). As we found for $Ca_V1.2$ channels, the mean area and density of TRPV4 channel clusters increased rapidly over a period of about 12 hours and reached a plateau at about 24 hours (**Figure 4.5D-E**). Similarly, the TRPV4 cluster size and density data were fit with exponential functions with $T_{1/2}$ at 6.4 and 5.7 hours after transfection for cluster size and cluster density, respectively. The common finding that the cluster sizes and cluster densities of these two types of channels increase rapidly over a short period following transfection and expression, but then reach a steady state, suggests the presence of a regulatory, feedback mechanism controlling channel cluster size and density.

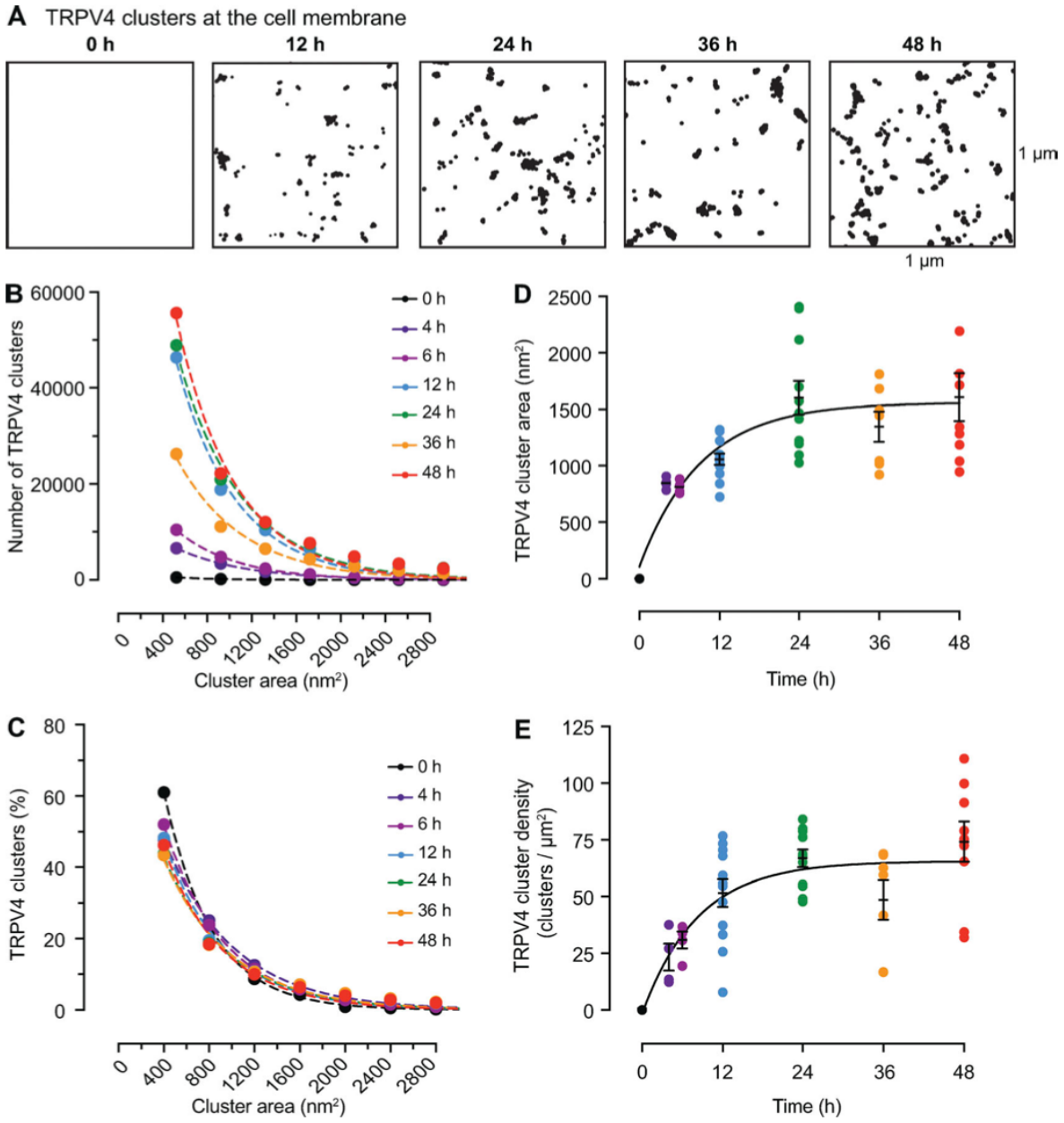

Figure 4.5. Time course of the formation of TRPV4 channel clusters in tsA-201 cells. (**A**) Representative super-resolution GSD binary masks of immunolabeled TRPV4 channels in transfected tsA-201 cells at 0, 12, 24, 36, and 48-hours post transfection. (**B**) Frequency distribution of TRPV4 channels cluster areas at each time point. (**C**) Relative frequency distribution of TRPV4 channels cluster areas expressed as percentages. Dashed color lines in **B** and **C** represent the best single exponential decay function fit for each data set. (**D**) Change of mean TRPV4 channel cluster area at different time points post transfection, data is presented as mean ± SEM for individual cells at each time point. (**E**) Change of TRPV4 channel cluster density at different time points post transfection. Data is presented as mean ± SEM for individual cells at each time point. Mean cluster area data (**D**) and mean cluster density data (**E**) were fit with a one phase exponential equation (solid black line). The tau values for cluster area and cluster density are 9.17 and 8.22 hours respectively. (**B-E**) All data was compiled as followed: 4h: n = 13734 from

four cells, 6h: 20004 clusters from four cells, 12h: n = 96295 clusters from 12 cells, 24h: n = 111632 clusters from 11 cells, 36h: n = 60518 clusters from seven cells, 48h: n = 120416 from 12 cells.

By tuning the three parameters in our model through iterative simulations, we found a connection between P_g and P_R to channel cluster size and between P_n channel cluster density.

Thus, properly constraining our model required information about channel turnover rates within cell membranes. To this end, we expressed photoactivatable-GFP tagged $Ca_V1.2$ or TRPV4 channels (PA-$Ca_V1.2$ and PA-TRPV4) in tsA-201 cells. Photoactivatable-GFP is non-fluorescent until it is exposed to a brief blue light pulse. Thus, PA-$Ca_V1.2$ and PA-TRPV4 fluorescence is limited to the set of channels expressed at the time of photoactivation. PA-$Ca_V1.2$ and PA-TRPV4 fluorescence intensity is therefore proportional to the number of channels expressed and could be used to determine dwell time, i.e., the time these channels spend in the membrane.

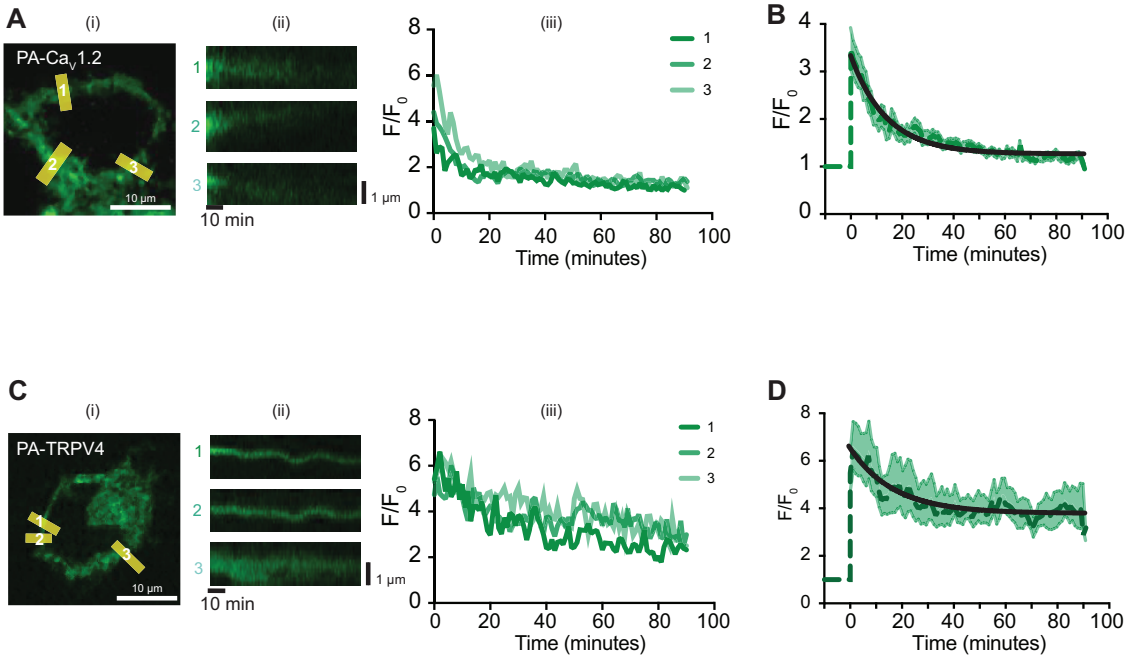

Figure 4.6. Dwell times for $Ca_V1.2$ and TRPV4 channels in tsA-201 cell are fast. (**A**) Representative image of a tsA-201 cell transfected with Ca_V4-PAGFP immediately after stimulation (**i**), with corresponding labeled ROI slices (**ii**), and fluorescent traces of the ROI slices (**iii**). (**B**) Mean time course of Ca_V4-PAGFP normalized fluorescence (dark green dashed line) and SEM at each time (light green shaded area) of all normalzed ROIs. Time course was fit with an exponential function (black line). 26 ROIs from nine cells were averaged. (**C**) Representative image of a tsA-201 cell transfected with TRV4-PAGFP immediately after stimulation (**i**), with corresponding labeled ROI slices (**ii**), and fluorescent traces of the ROI slices (**iii**). (**B**) Mean time course of TRVP4-PAGFP normalized fluorescence (dark green dashed line) and SEM at each time (light green shaded area) of all normalized ROIs. Time course was fit with an exponential function (black line). Seventeen ROIs from six cells were averaged.

For these experiments, cells expressing PA-$Ca_V1.2$ or PA-TRPV4 (**Figure 4.6**) were imaged before and after a 10 seconds exposure to 405 nm light to activate the PA-GFP. In **Figure 4.6A**, we show a confocal image from a center section of a representative tsA-201 cell expressing PA-$Ca_V1.2$. As expected, after photoactivation the fluorescence was largely limited to the surface membrane of the cell. For analysis, we measured the spatially averaged fluorescence and generated pseudo line-scans from multiple regions in the membrane from 2D image stacks. The time course of fluorescence intensity in three sites in the membrane is shown to the right of the 2D image in **Figure 4.6A**. Note that at each site, over a period of 90 min after photoactivation, PA-$Ca_V1.2$ fluorescence nearly disappears, suggesting that most channels are removed from the membrane within this period. **Figure 4.6B** shows the averaged, normalized fluorescence intensity from all the membrane sites analyzed from multiple cells. The decaying phase of the curve was fit with a single exponential function with a $T_{1/2}$ of 9.74 minutes.

In **Figure 4.6C**, we show the results of equivalent experiments for cells expressing PA-TRPV4. As in the case of PA-$Ca_V1.2$, PA-TRPV4 fluorescence in the membrane increased following 405 illumination, and decayed with time. However, unlike PA-$Ca_V1.2$,

PA-TRPV4 fluorescence seems to reach a steady state around 45% of the initial maximum signal. **Figure 4D** shows the averaged (with SEM), normalized fluorescence and decay of all the analyzed sites. These data suggest that while a population of TRPV4 channels is removed from the membrane, a larger subset of channels either remains embedded within the membrane or is removed but then recycled back to it. A $T_{1/2}$ of 11.59 minutes for the first population was estimated by fitting a single exponential function.

The model captures dwell times and time-dependent assembly of $Ca_V1.2$ and TRPV4 channel clusters*.* Our goal in acquiring the experimental measurements of the time course of channel cluster formation and channel turnover rate or dwell time described above was to extend our model beyond its successful representation of steady-state conditions (**Figure 4.3**). That is, could our model replicate the time-dependent assembly of $Ca_V1.2$ and TRPV4 channel clusters that we observed experimentally in tsA-201 cells (**Figure 4.4** and **4.5**) while incorporating the membrane dwell times that we measured (**Figure 4.6**).

Figure 4.7 shows the relationship between channel and cluster dwell times and model parameters, P_g and P_R. Channel and cluster dwell times are independent of model parameter, P_n, as dwell times correspond to events following nucleation. Note that decreasing P_R or decreasing P_g increases the membrane dwell times for both individual channels (**Figure 4.7A**) and channel clusters (**Figure 4.7B**). Further, these data suggest that the dwell times of a channel or a cluster in the membrane is determined by individual P_g values. For example, the predicted dwell times in the membrane of a cluster in a cell

with P_g = 0.07 and P_R = 0.0007 (P_g/P_R = 100) is 12 minutes, while a cell with P_g = 0.1 and P_R = 0.001 (P_g/P_R = 100) is 9 minutes.

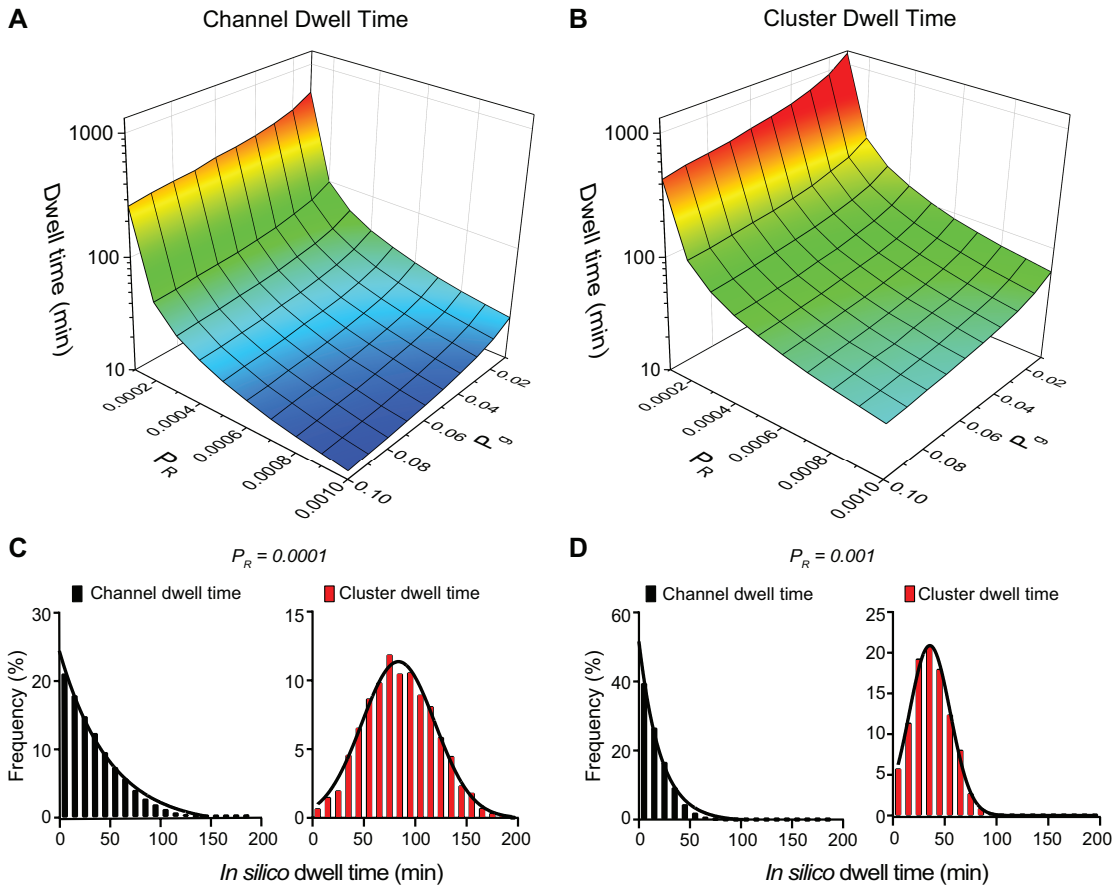

Figure 4.7. P_g and P_R determine channel and cluster dwell time. (**A**) Surface plots showing the relationships between P_g, P_R, and channel dwell time, or (**B**) cluster dwell time**.** (**C**) Frequency distributions of channel and cluster dwell times with P_R equal to 0.0001, (**D**). or 0.001. For the simulations in panels **C** and **D**, P_g and P_n were 0.01 and 0.00006, respectively.

We plotted the distributions of membrane dwell times for individual channels and channel clusters with a P_g of 0.01 and P_R of 0.0001 (**Figure 4.7C**) or 0.001 (**Figure 4.7D**). Regardless of the magnitude of P_g and P_R, our model generated exponential membrane

dwell-time distributions for individual channels that were exponential and Gaussian dwell-time distributions for channel clusters. The mean dwell times in the membrane obtained from our model for both individual channels (60 min) and channel clusters (75 min) using a P_R of 0.0001 were similar to those suggested for $Ca_V1.2$ in neuronal dendrites (≈1 hour) [118].

Because the single channel and channel cluster membrane dwell times are predominantly set by the value of P_g in our model, we examined the effects of the paraments P_R and P_n on cluster area and densities after setting P_g to 0.07, the value that reproduced our experimental measurements of the area of $Ca_V1.2$ and TRPV4 channel clusters (**Figures 4.4** and **4.5**). As shown in **Figure 4.8A**, we found that setting the values of P_g and P_R in ratios ranging from 20-100 resulted in increasing channel cluster areas and that a P_g/P_R ratio > 50 was required to generate clusters with areas similar to those measured in our experiments for $Ca_V1.2$ and TRPV4 in tsA-201 cells 48 hours after transfection. This is important as it indicates that channel cluster sizes are determined by the P_g/P_R ratio and not by individual P_g and P_R values.

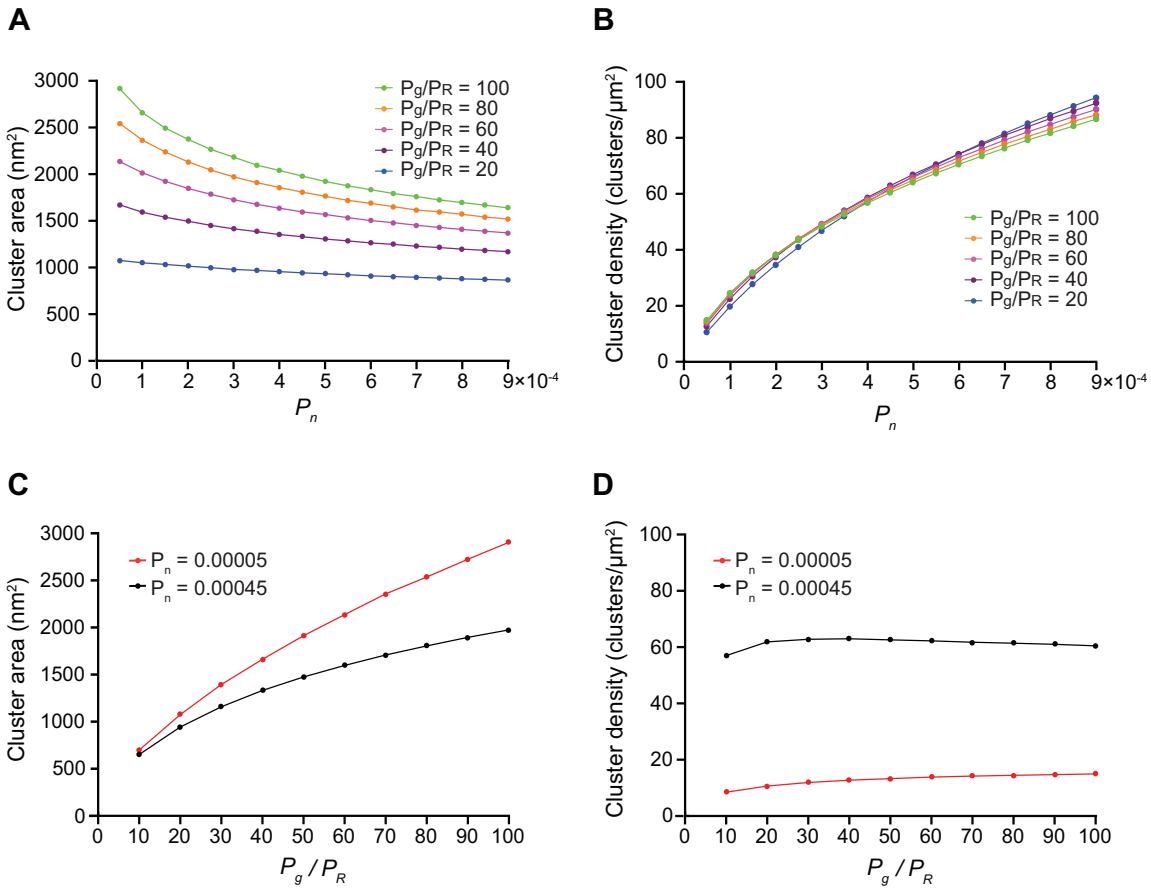

Figure 4.8. *In silico* stochastic self-assembly of protein clusters with realistic sizes and densities. (A) Plot of the relationships between P_n and cluster area at P_g/P_R ratios equal to 20 (P_g = 0.07, P_R = 0.0035), 40 (P_g = 0.07, P_R = 0.00175), 60 (P_g = 0.07, P_R = 0.001166667), 80 (P_g = 0.07, P_R = 0.000875), and 100 (P_g = 0.07, P_R = 0.0007). (**B**) Relationships between P_n and cluster density at P_g/P_R ratios equal to 20 (P_g = 0.07, P_R = 0.0035), 40 (P_g = 0.07, P_R = 0.00175), 60 (P_g = 0.07, P_R = 0.001166667), 80 (P_g = 0.07, P_R = 0.000875), and 100 (P_g = 0.07, P_R = 0.0007). For simulations in panels A and B, we averaged cluster area and density values at steady-state for 2000 iterations. (**C**) Effect of P_g/P_R ratios on cluster area. (**D**) Effect of P_g/P_R ratios on cluster density. (**C,D**) For these simulations, we set the value of P_n = 0.00005 (red traces) and P_n = 0.00045 (black traces), P_g = 0.07 and P_R ranged between 0.007 and 0.0007 to achieve P_g/P_R ratios of 10-100.

We also found that the influence of P_g/P_R ratios on channel cluster formation in our model is affected by P_n. For example, cluster area decreases as P_n is increased. This can be explained by the fact that when the P_n value is small, the probability of channel insertion decreases, and the channel clusters grow according to the specific values of P_g and P_R.

However, when P_n is increased, the probability of channel insertion increases, resulting in the initiation of multiple clusters with large variations in size and a decrease in mean cluster area as shown in **Figure 4.8A.** In contrast, cluster density is independent of the P_g/P_R ratio and mainly determined by P_n (**Figure 4.8B**).

To further illustrate the effects of P_R and P_n on channel cluster area, we show the results of a series of simulations using two different P_n values (**Figure 4.8C**): 0.00045 (black trace) and 0.00005 (red trace). Similarly, the effects of P_R and P_n on channel cluster density are shown in **Figure 4.8D.** These two P_n values were chosen because they generated simulated channel cluster areas similar to those observed in tsA-201 cells expressing $Ca_V1.2$-EGFP (**Figure 4.4**) or TRPV4-EGFP (**Figure 4.5**) (i.e., P_n = 0.00045), or to those reported in studies in the endogenous channels native cells (i.e., P_n = 0.00005) [100, 102, 103].

In silico stochastic self-assembly of $Ca_V1.2$ and TRPV4 clusters. As our model successfully simulated the creation of channel clusters with size, densities, and dwell times similar to those observed experimentally, we set out to use this model to replicate the experimental data we acquired on the time courses of $Ca_V1.2$ and TRPV4 channel cluster formations expressed in tsA-201 cells (**Figures 4.4** and **4.5)**. To do so, images were generated on every iteration of the model using time-dependent probability functions P_g, P_n, and P_R. In **Figures 4.9A and 4.10A,** we defined the time-dependent probability functions of P_g, P_n, and P_R to be sigmoid functions. The rationale for this was our own data showing that the time course of $Ca_V1.2$ and TRPV4 cluster growth (P_g) and densities

(P_n) followed a sigmoidal distribution and the work by [115] suggesting that $Ca_V1.2$ channel internalization in neurons (i.e., P_R) increased as $Ca_V1.2$ channel number increased. The range of P_n values used were determined by the density data in **Figures 4.4-4.5** as well as the P_n-density relationships in **Figure 4.8**.

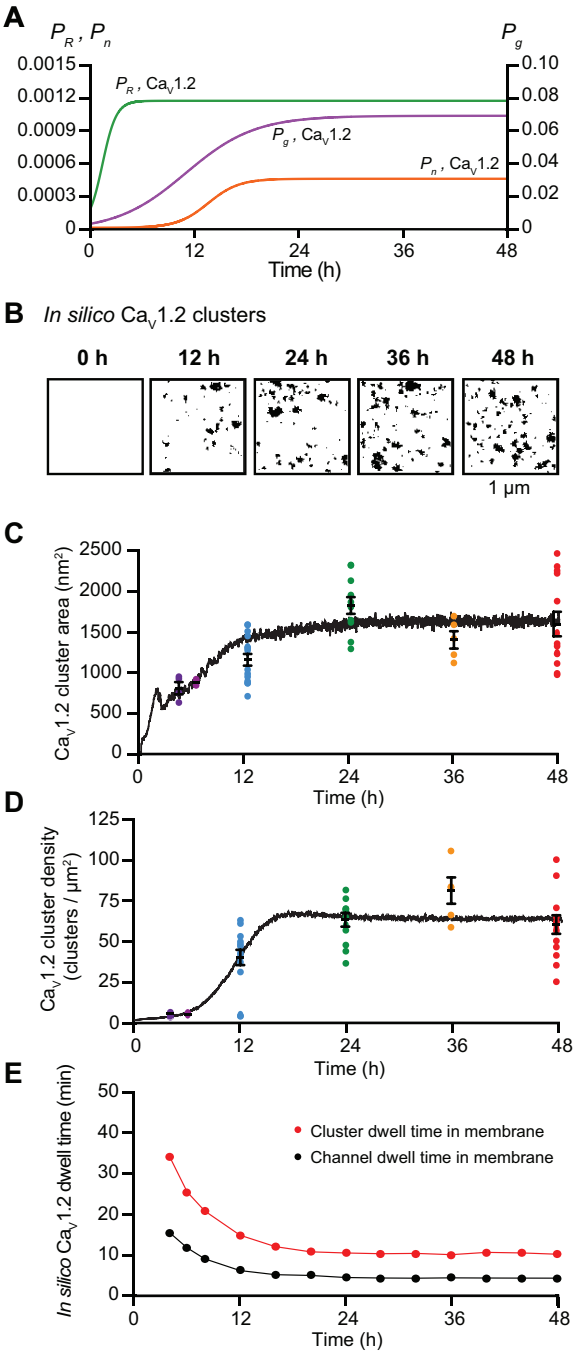

Figure 4.9. Sigmoidal time-dependent changes in P_g, P_n, and P_R reproduce the time course of $Ca_V1.2$ cluster formation in the plasma membrane of tsA-201 cells. (**A**) Plots of $P_{g,Cav1.2}$ (purple), $P_{n,Cav1.2}$ (orange), and $P_{R,Cav1.2}$ (green) versus time. $P_{R,Cav1.2} = \left(\frac{1}{1+5e^{-60t}}\right) * 0.001166667$, $P_{g,Cav1.2} = \left(\frac{1}{1+15e^{-12t}}\right) * 0.07$, and $P_{n,Cav1.2} = \left(\frac{1}{1+2000e^{-27t}}\right) * 0.00045$. (**B**) *In silico* images of $Ca_V1.2$ clusters at 0, 12, 24, 36, and 48 h after the initiation of expression using the parameters in panel **A**. (**C**) The black trace depicts the time course of mean cluster area and (**D**) densities of simulated clusters. Colored dots represent the superimposed experimental data from **Figure 3**. (**E**) Mean $Ca_V1.2$ channel (black) and cluster (red) dwell times based on the sigmoidal functions P_g, P_n, and P_R.

In the case of $Ca_V1.2$ channels, the time-dependent probability functions $P_{g,Cav1.2}$ and $P_{n,Cav1.2}$ reached steady-state in about 18 hours. Similarly, in the case of TRPV4 channels, $P_{g,TRPV4}$ and $P_{n,TRPV4}$ reached steady-state in about 20 hours. $P_{R,Cav1.2}$ and $P_{R,TRPV4}$ however, reached their steady-states in about 8 hours, which is critical as the ratio between P_R and P_g controls the cluster area. **Figures 4.9B** and **4.10B** show computer-generated 2D images of $Ca_V1.2$ and TRPV4 channel clusters at various iterations corresponding to 0, 12, 24, 36, and 48 hours after transfection.

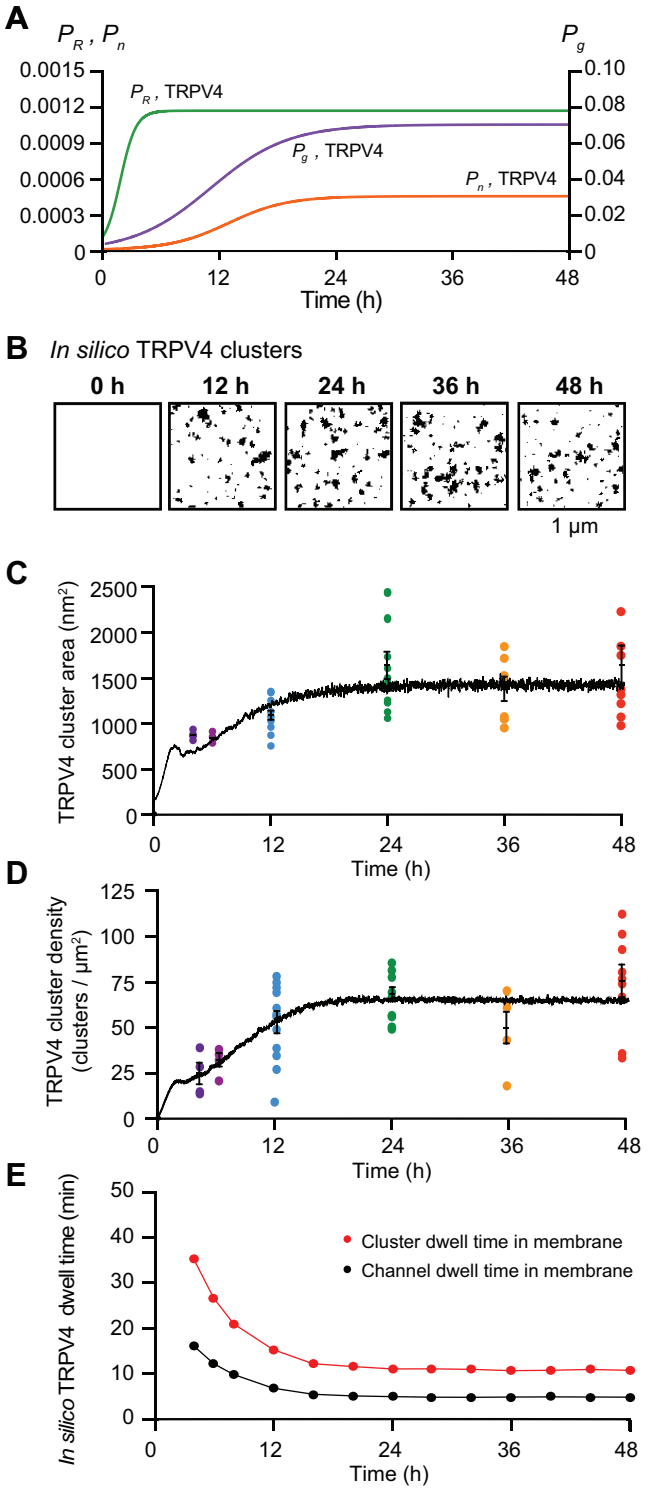

Figure 4.10. Sigmoidal time-dependent changes in P_g, P_n, and P_R reproduce the time course of TRPV4 cluster formation in the plasma membrane of tsA-201 cells. (**A**) Plots of $P_{g,TRPV4}$ (purple), $P_{n,TRPV4}$ (orange), and $P_{R,TRPV4}$ (green) versus time. $P_{R,TRPV4} = \left(\frac{1}{1+10e^{-60t}}\right) *$

0.001166667, $P_{g,TRPV4} = \left(\frac{1}{1+15e^{-12t}}\right) * 0.07$, and $P_{n,TRPV4} = \left(\frac{1}{1+75e^{-16t}}\right) * 0.00045$. (**B**) *In silico* images of TRPV4 clusters at 0, 12, 24, 36, and 48 h after the initiation of expression using the parameters in panel **A**. (**C**) The black trace depicts the time course of mean cluster area and (**D**) densities of simulated clusters. Colored dots represent the superimposed experimental data from **Figure 4**. (**E**) Mean TRPV4 channel (black) and cluster (red) dwell times based on the sigmoidal functions P_g, P_n, and P_R.

In **Figures 4.9C-D** and **4.10C-D**, we plotted the results obtained from the model simulations (black trace) relative to our experimental data points for the sizes and densities of channel clusters. Cluster sizes for $Ca_V1.2$ and TRPV4 channels are similar, but there is a key difference in their densities. The cluster density for $Ca_V1.2$ channels is low relative to TRPV4 at 4 and 8 hours. This behavior is reproduced by the time-dependent probability function for P_n.

We could extract the membrane dwell times for individual channels and channels clusters of $Ca_V1.2$ (**Figure 4.9E**) and TRPV4 channels (**Figure 4.10E**) from these simulations. The dwell times in the membrane of individual $Ca_V1.2$ and TRPV4 channels (≈ 15 minutes) and channel clusters (≈ 35 minutes) were initially high, but decreased to lower steady-state levels after approximately 12 hours. At 48 hours, the predicted dwell times of both individual channels ($Ca_V1.2$ and TRPV4 : 4.2 minutes) and channel clusters ($Ca_V1.2$ and TRPV4: 10.3 minutes) were quite similar for the two channel types. These data suggest that steady-state channel organization for either channel type can be attained by time-dependent changes in P_g and P_n and a relatively rapid turnover rate for both individual channels and clusters. Further, the data suggest feasible set points for P_g and P_n in living cells.

Feedback control of the stochastic self-assembly of $Ca_V1.2$ and TRPV4 clusters

As mentioned earlier, [115] suggested that $Ca_V1.2$ channel internalization increases as the number of channels increases, indicating some level of feedback between channel number and P_R, presumably as mediated through intracellular Ca^{2+} levels. Thus, we augmented our model to demonstrate how $Ca_V1.2$ and TRPV4 channel cluster size and density might be regulated by a feedback mechanism dependent on the number of channels present on the grid. To do so, we set the rates of cluster growth proportional to the number of channels present, represented by the first term (r_xN; x = *n, g, or R*) in equations 1, 2, and 3 in the Methods. This term provides the positive feedback component of the model. The second term (P_x/K_x; x = *n, g, or R*) in equations 1, 2, and 3 is responsible for the negative feedback component of the model. When the number of channels is small, the positive feedback process dominates. As the number of channels becomes larger, the negative feedback process dominates.

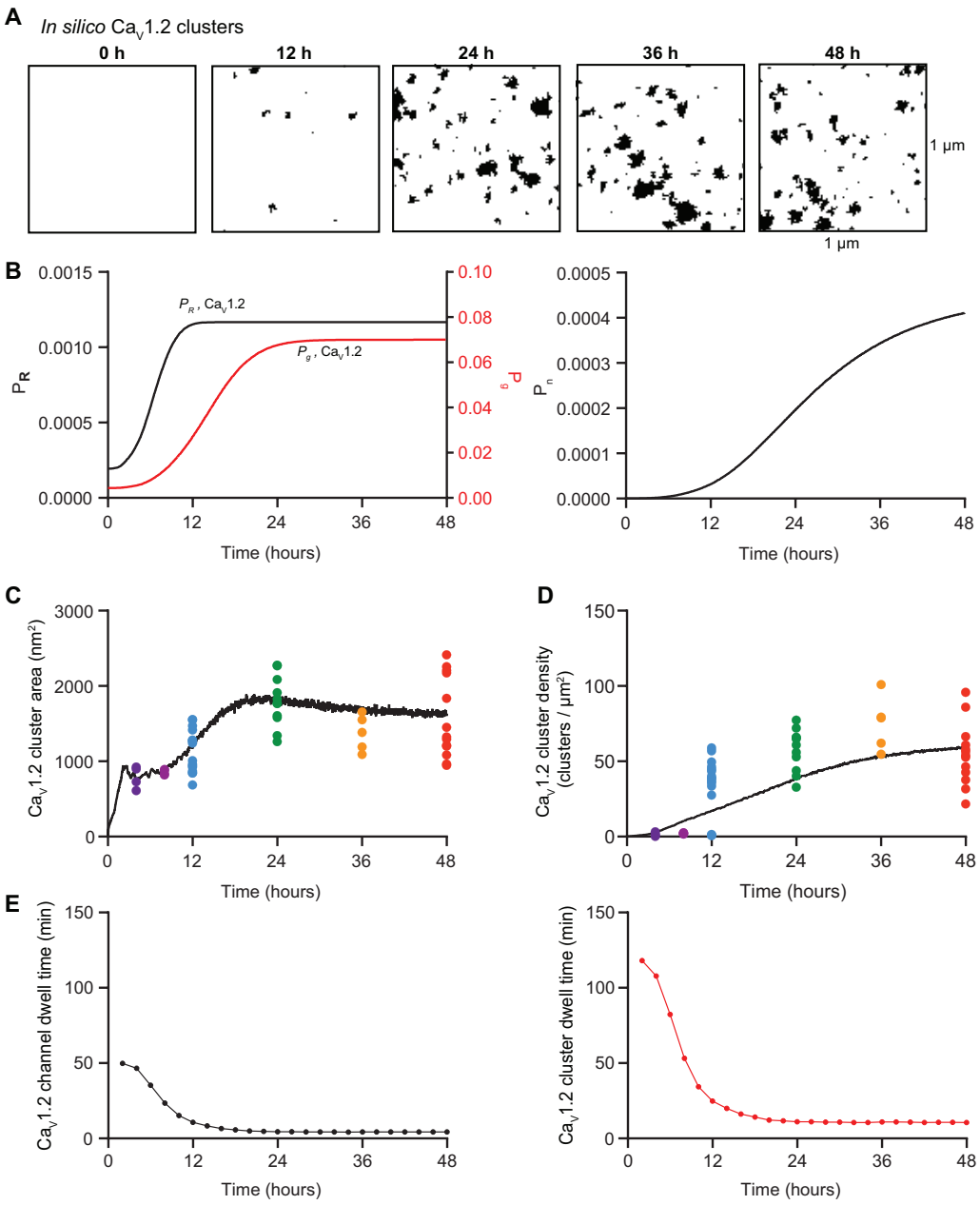

Figure 4.11. Feedback model for Ca$_V$1.2 cluster formation. (**A**) *In silico* images of Ca$_V$1.2 clusters at 0, 12, 24, 36, and 48 h after the initiation of expression. (**B**) Solutions to the feedback model equations $\frac{dP_R}{dt}$, $\frac{dP_g}{dt}$, and $\frac{dP_n}{dt}$ (**C**) The black trace depicts the time course of mean cluster area and (**D**) density of simulated Ca$_V$1.2 clusters. Color dots represent the superimposed experimental data from **Figure 4.3**. (**E**) Predicted mean Ca$_V$1.2 channel (black) and cluster dwell times (red) based on the feedback model.

The impact of these additional terms in the model are shown in **Figure 4.11** for $Ca_V1.2$ and in **Figure 4.12** for TRPV4 channels. **Figures 4.11A** and **4.12A** show simulated images of $Ca_V1.2$ and TRPV4 channel clusters at 0, 12, 24, 36, and 48 hours after transfection. The positive and negative feedback processes create sigmoidal curves for P_g, P_R, and P_n (**Figures 4.11B** and **4.12B**). The time course of cluster growth is governed by the product of the P_g and P_R curves. Accordingly, depending on the shape of P_g and P_R curves, the cluster sizes may have two phases. Cluster density was mainly determined by a sigmoidal P_n curve.

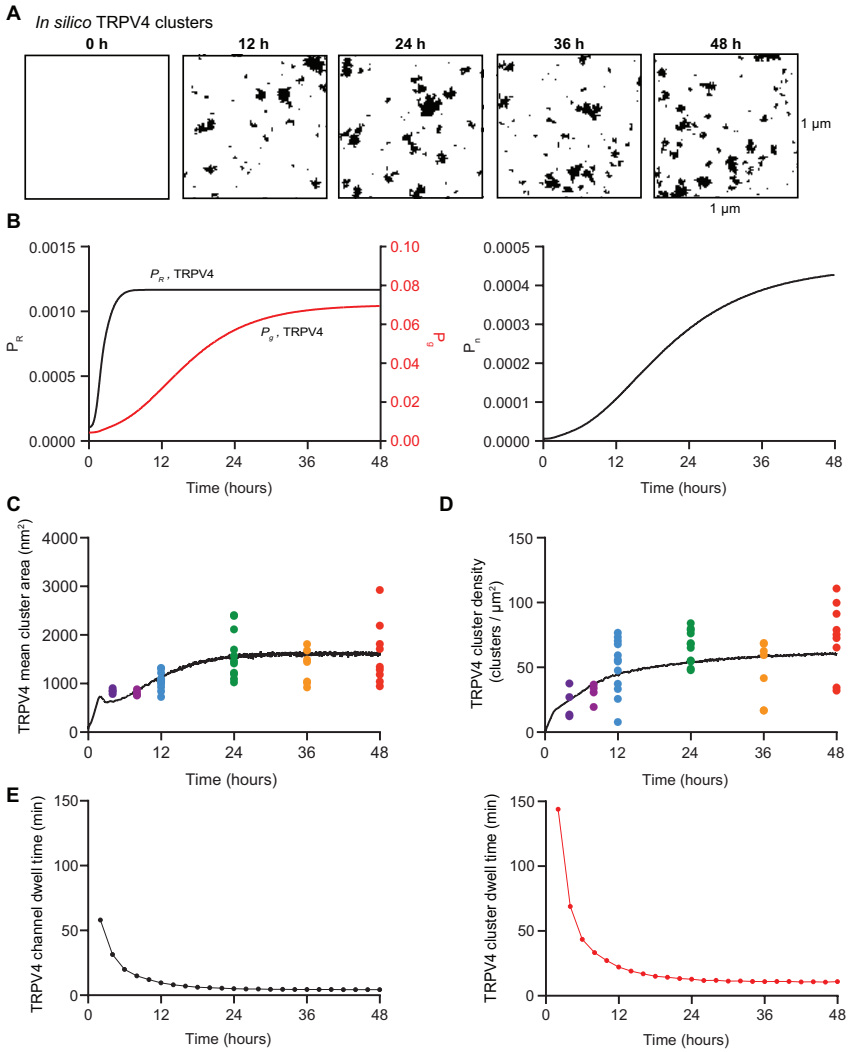

Figure 4.12. Feedback model for TRPV4 cluster formation. (**A**) *In silico* images of TRPV4 clusters at 0, 12, 24, 36, and 48 h after the initiation of expression. (**B**) Solutions to the feedback model equations $\frac{dP_R}{dt}$, $\frac{dP_g}{dt}$, and $\frac{dP_n}{dt}$ (**C**) The black trace depicts the time course of mean cluster area and (**D**) density of simulated TRPV4 clusters. Color dots represent the superimposed experimental data from **Figure 4.4**. (**E**) Predicted mean TRPV4 channel (black) and cluster dwell times (red) based on the feedback model.

In **Figures 4.11C-D** and **4.12C-D**, we plotted the simulated and experimentally-measured and cluster sizes and densities for $Ca_V1.2$ and TRPV4 channels. The simulations show that increasing $P_{n,Cav1.2}$ (from 2e-07 to 0.00045), $P_{g,Cav1.2}$ (from 0.004 to 0.07), and $P_{R,Cav1.2}$ (from 0.0002 to 0.0012) (**Figure 4.11B**) or $P_{n,TRPV4}$ (from 0.000006 to 0.00045), $P_{g,TRPV4}$ (from 0.004 to 0.07), and $P_{R,TRPV4}$ (from 0.0001 to 0.0012) (**Figure 4.12B**) increases channel cluster areas and densities over time to levels similar to those observed experimentally. In the case of $Ca_V1.2$, $P_{g,Cav1.2}$, $P_{R,Cav1.2}$ and $P_{n,Cav1.2}$ reached plateau levels at about 24, 10, and 16 hours after transfection, respectively. In the case of TRPV4, $P_{g,TRPV4}$, $P_{R,TRPV4}$ and $P_{n,TRPV4}$ values plateaued about 24, 6, and 24 hours, respectively.

We also extracted the membrane dwell times of individual $Ca_V1.2$ (**Figure 4.11E**) and TRPV4 channels (**Figure 4.12E**) and clusters from simulations using the feedback model. With the parameters used in our simulations, the mean channel ($Ca_V1.2$ = 50 minutes; TRPV4 = 60 minutes) and channel cluster ($Ca_V1.2$ = 120 minutes; TRPV4 = 140 minutes) membrane dwell times were initially high. However, these values quickly (i.e., after about 4 hours) decreased and then remained relatively stable over time for both channel types, such that at 48 hours the predicted channel and cluster dwell times for $Ca_V1.2$ were 4.3 and 10.5 minutes, respectively, and for TRPV4 were 4.3 and 10.9 minutes, respectively. To demonstrate how our feedback model works, we created videos of simulations of

$Ca_V1.2$ and TRPV4 trafficking and cluster formation in the membrane using the P_g, P_R, and P_n values in **Figures 4.11** and **4.12.**

The two methods we used to reproduce our experimental measurements of cluster formation for $Ca_V1.2$ (**Figure 4.4**) and TRPV4 (**Figure 4.5**) channels data are complementary and supportive of the concept that channel cluster size and density are regulated via feedback mechanisms. In the first method, we used empirically derived assumptions regarding time-dependent changes in P_R, P_n, and P_g**.** This first model predicts that in order to reach a plateau phase in cluster size and density, we must increase the parameters P_n, P_g, and P_R until reaching a constant or equilibrium level. We proposed that the curves should be sigmoidally-shaped such that changes in cluster size and density would be constrained to the desired values of P_n, P_g, and P_R we observed in tsA cells. In the second method, the behavior of P_n, P_g, and P_R through time was modeled using differential equations coupled by the total number of channels, allowing us to explicitly include a feedback mechanism.

4.5 Discussion

Using a combination of experimental and computer modeling approaches, we have made five important observations regarding the formation of ion channel clusters and trafficking in living cells. First, the distributions of clusters of the three types of channels studied ($Ca_V1.2$, BK, TRPV4) were all described by a single exponential function regardless of the type of cell they are expressed in, supporting the hypothesis that the presence of ion channels clusters in cell membranes is consequent to a stochastic, self-assembly process. Second, $Ca_V1.2$ and TRPV4 channel clusters form in tsA-201 cells with an initial

period of rapid growth in size, after which they are maintained in a steady-state. Third, this steady-state form in tsA-201 cells is maintained by a relatively fast turnover rate of $Ca_V1.2$ and TRPV4 channels. Fourth, our model predicts that steady-state size distributions of membrane channel clusters could be sustained by a range channel turnover rates. While we are aware of the possibility that our measurements are based solely on a heterologous expression system and might differ from those made in other cell types, our fifth observation is that both our experimentally-measured and predicted membrane dwell times are similar to those reported for $Ca_V1.2$ in cultured cardiac HL-1 cells [119] and in primary neurons [120], as well as to mean transcript and protein dwell times [121].

To illustrate how our model could be used by physiologists interested in investigating the role of a particular interacting protein in ion channel clustering, we have considered three potential scenarios in which a change in a physiological process alters ion channel cluster area or density via changes in one of the three model parameters (i.e., P_n, P_g or P_R). In the first scenario, let us propose that the insertion of channels at the plasma membrane is enhanced by the upregulation or activation of a signaling pathway. In our model, this process would result in an increase in the parameter P_n. An example of this could be the Ca^{2+}-dependent upregulation of K^+ channels expression via the activation of the calcineurin/NFAT signaling pathway. As first demonstrated by [42] and Rossow et al [122-124], Kv4 and Kv2 channel expression is tightly regulated by intracellular Ca^{2+} in cardiac and vascular cells. BK channel expression is also regulated by Ca^{2+} levels in smooth muscle [125, 126]. In this scenario, the increase in the expression of the channels will

increase the available pool of channels that can be inserted at the plasma membrane, increasing cluster density. Interestingly, the differences in $Ca_V1.2$ and TRPV4 cluster densities reported here among tsA-201 cells, smooth muscle, and ventricular myocytes were simulated by variations in the P_n among these cells. These data suggest that the level of expression of these channels and/or the proteins related with the trafficking and delivery of these channels to the plasma membrane vary between cells.

In the second scenario, we consider the possibility that the insertion of new channels is favored to occur in the same sites where other channels have been previously inserted because of the upregulation of an interacting protein. In our model, this process would increase P_g. An example of such a protein is BIN1, which binds to the inner face of the plasma membrane and forms lattices via the cooperative binding of other molecules, thus creating membrane microfolds [127]. In ventricular myocytes, BIN1 has been implicated in the formation of membrane curvatures [128] and in anchoring microtubules where newly synthesized $Ca_V1.2$ channels are delivered to the surface membrane [129, 130]. As such, BIN1 could function to increase the local concentration of $Ca_V1.2$ channels at specific sites in the plasma membrane, enhancing their clustering. Consistent with this, [110] found that overexpression BIN1 in human embryonic stem cell-derived cardiomyocytes increased $Ca_V1.2$ cluster size. Thus, BIN1 could be acting to direct the directed insertion of $Ca_V1.2$ channels in the sarcolemma of cardiac myocytes which would increase the P_g of these channels. Importantly, in the case of channels that undergo functional coupling (i.e. L-type Ca^{2+} channels), the increase in cluster size could

strengthen the coupling between these channels resulting in a further increase in the amplitude of ion flux.

Finally, in the third scenario, we imagine a situation in which the removal of individual ion channels or ion channel clusters from the plasma membrane is enhanced by an interacting protein. In our model, this process would result in an increase in the parameter P_R. An example of this could be the activation of the HECT ubiquitin ligase ALP4, which has been linked to TRPV4 channel internalization [131]. Another example is the tumor suppressor eIF3e/Int6 (eukaryotic initiation factor 3 subunit e), which induces internalization of $Ca_V1.2$ channels in neurons [115]. In this scenario, the activation of these proteins will likely be associated with an overall decrease in channel membrane dwell time and a decrease in clusters size.

An important observation we made in the course of this study is that whereas the sizes and densities of $Ca_V1.2$ and TRPV4 channel clusters expressed in tsA-201 cells increased rapidly after transfection, both parameters reach a plateau within 24 hours. These results suggest that plasma membrane expression levels and clustering of exogenously expressed $Ca_V1.2$ and TRPV4 channels is under the control of a feedback mechanism. Indeed, recent live-cell imaging experiments indicate that $Ca_V1.2$ containing vesicles in tsA-201 cells could have multiple mechanisms for interacting and delivering channel to the plasma membrane [89]. Similar proposals have been put forth for endogenous $Ca_V1.2$ in cardiac myocytes [132] and neurons [115]. The latter report suggested that action potential firing rate, channel activity, and a Ca^{2+}-driven increase in $Ca_V1.2$ internalization (i.e., P_R) was responsible for regulating plasma membrane

expression levels of $Ca_V1.2$. Our feedback model relies exclusively on channel number and does not take into account the state of the channel (e.g., open, deactivated, inactivated, desensitized). Thus, a desensitized or inactivated channel would have the same probability of being removed by internalization or endocytosis than a deactivated or open channel. Mechanisms determining steady-state levels of these ion channels in cardiac and smooth muscle will need further study.

Another intriguing question posed by our work is whether the membrane dwell times and time course of clustering of $Ca_V1.2$ and TRPV4 channels in native cells are similar to those we found operating in tsA-201 cells. The work by [110] suggests that in hESC-CMs, $Ca_V1.2$ cluster sizes and densities increased from the induction of differentiation until day 30. Interestingly, the channel cluster sizes and densities achieved at this time point were similar to those in adult ventricular myocytes, raising the possibility that they had reached an intrinsically-defined level of steady-state expression and clustering. Regardless of whether a steady state had been reached or not, these hESC-CM data suggests that the rates of cluster nucleation, growth, removal, and thus channel membrane dwell times are likely different among cells at different levels of differentiation. A testable hypothesis is that the membrane dwell time of channels is higher in rapidly dividing cells like tsA-201 cells, than in fully differentiated, non-dividing cells like ventricular myocytes, and that upon stimulation (e.g., autonomic nervous system, physiological and pathological hypertrophy) changes in gene expression, channel delivery, recycling and/or protein degradation could increase channel dynamics.

Another key question raised by our study is whether membrane channels are internalized individually or through the removal of entire clusters. Our experimental data and model simulations do not provide a definitive answer, but simulations in which channels were exclusively removed one at a time predicted the formation of a large number of macro-clusters with parameters similar to those used to reproduce experimental data from cardiac myocytes, smooth muscle cells, neurons, and tsA-201 cells. Yet, macro-clusters predicted by the model were not observed experimentally. Accordingly, we modified the model so that channel internalization would be stochastic and involve individual channels as well as channel clusters of varied sizes. Considering that the area of an endocytic vesicle could range from 1200 to 1.26 $x10^5$ nm^2 and the mean cluster areas reported here range from about 1900 to 3700 nm^2 this assumption seems reasonable. Future experiments will be required to test this hypothesis.

Finally, while our data reveal that in smooth muscle and tsA-201 cells, channels are clustered randomly throughout the entire cell surface, it is important to mention that variations in channel expression both between and within cells are commonly observed and reported. To cite just a few examples, Na_V1 channels are highly concentrated in the nodes of Ranvier of myelinated axons, but largely absent from the internodal membrane [47], $Ca_V1.2$ channel are preferentially expressed in along the T-tubules of ventricular myocytes [100], the Na^+/H^+ exchanger is absent from the T-tubules [133], and the Na^+/K^+α2ATPase proteins are distributed preferentially in the T-tubules and surface sarcolemma [134]. While these regional variations in channel expression may seem incompatible with our model, they could still be the result of a stochastic, self-assembly

process operating within a restricted cellular domain. For example, our data suggest that $Ca_V1.2$ channel clusters are stochastically self-assembled along the T-tubules of ventricular myocytes, but not throughout the entire cell. These seemingly contradictory observations can be reconciled by proposing that there may be variations in P_n, P_g, or P_R in different compartments of the same cell that lead to stochastic self-assembly of clusters therein. The possibility of regional variations in P_n, P_g, and P_R should be addressed in further studies.

In summary, we have provided a set of experimental measurements and computer simulations that support the hypothesis that the formation of ion channel clusters in the surface membrane of excitable cells reflects the operation of a stochastic self-assembly process without the involvement of any active mechanism of aggregation, such as agrin-induced recruitment of acetylcholine receptors into the post-synaptic motor endplate [135], ankyrin G-mediated clustering of voltage-gated Na^+ channels and Kv7 channels et nodes of ranvier [136], and K_V2 channel clustering by VAPA and VAPB proteins [137, 138]. Indeed, our data are consistent with the view that membrane channel clustering is the default organization for multiple types of channels in the surface membranes of VSMCs. Notably, our model incorporates a self-regulating mechanism that assumes a feedback process between channel number and channel cluster formation. Our model may be broadly applicable to the distributions of many different types of membrane (bound proteins and channels) in health and disease states. We certainly cannot rule out the possibility that one or more proteins will be found that are not randomly distributed along the surface membrane. Whether or not there is a functional consequence of

clustering for all the types of ion channels, as we have found for $Ca_V1.2$, BK, and TRPV4 channels, remains an open question, but a very important one.

Chapter 5: The Hernandez-Hernandez model and future directions

5.1 Conclusion

In this dissertation, in Chapter 1-3 we sought to study the mechanisms of electrical activity and Ca^{2+} dynamics in an isolated mesenteric VSMCs. To do so, we presented the development, validation, and application of a modeling and simulation study. The Hernandez-Hernandez computational model was built using new experimental data collected from male and female arterial myocytes that suggest measurable sex-specific differences in voltage-gated $K_V2.1$ and $Ca_V1.2$ channels and then predicted the effects of those differences on membrane potential and Ca^{2+} signaling. We tested the hypothesis that differences in the amplitude and voltage dependencies of L-type $Ca_V1.2$ currents between males and females cause higher Ca2+ influx, $[Ca^{2+}]_i$, in female than in male mesenteric smooth muscle cells. In fact, we determined that small fluctuations in the number of $Ca_V1.2$ channels are both necessary and sufficient to account for male and female differences in $[Ca]_i$.

We then used the Hernandez-Hernandez model to make predictions of the effects of antihypertensive drugs in vascular myocytes. The model predictions suggested differences in the response of male and female myocytes to drugs and the underlying mechanisms for those differences. These predictions may constitute a first step towards better hypertensive therapy for males and females.

An important prediction arising from our modeling and simulation study is that very few channels are needed to contribute to and sustain the behavior of the membrane potential and calcium signaling in male and female myocytes. Such prediction provides an explanation of why VSMCs operate at a low voltage regime under conditions of high resistance membrane potential. Due to the nature of the stochastic activity of ion channels, local fluctuations in the function of ion channels provide a source of noise to the excitability of VSMCs. Future studies will address the question of how ion channel organization in the plasma membrane regulate their function.

In Chapter 4, using a combination of experimental and computer modeling approaches, we developed a mathematical model to explain ion channel formation in the plasma membrane of VSMCs. In our model, we used three parameters to represent channel cluster nucleation, growth, and removal probabilities, the values of which were estimated based on our experimental measurements. We determined the time course of cluster formation and membrane dwell time for $Ca_V1.2$ and TRPV4 channels expressed in tsA-201 cells to constrain our model. We expanded our mathematical model to include a self-regulating feedback mechanism to influence channel cluster development. Our findings strongly suggest that $Ca_V1.2$, BK, and TRPV4 proteins are all stochastically inserted in the plasma membranes of VSMCs and form homogenous clusters that grow in size until they reach a steady-state. Furthermore, our study supports the hypothesis that the presence of ion channel clusters in cell membranes is a result of a stochastic, self-assembly process.

5.2 Future directions

Our goal is to expand the models from Chapter 3 and include the effects of canonical signaling pathways activated by endogenous and pharmacological vasoactive agents on ion channels including spatial organization. We will integrate one step at a time canonical signaling pathways and mechanosensitive ions channels as follows:

Step 1: Canonical signaling pathways will be added as follows: The mathematical equations describing each signaling pathways will be integrated one step at a time to the whole-cell male and female models.

Step 2: We will optimize voltage and pressure dependent kinetics for transient receptors potential ion channels TRPV4, TRPC6 and TRPM4 current based on experiments made in male and female mouse mesenteric arterial myocytes (1) and we will integrate individual ionic currents into sex-specific whole-cell models (2).

Step 3: We will explore and analyze effects of signaling pathways *indirectly* by measuring its effects on the production of protein kinases (PKA, PKC and PKG) and track its effects on individual developed models of male and female ion channel currents. (1). Once we add main components of case 1 and 2, we will classify main parameters in potential therapeutic targets and determine drug induced responses in the electro-mechanical and pharmaco-mechanical coupling of VSM cells.

Following successful completion of the goals above, we will have established male and female models of VSMCs that will allow us to determine main parameters that can be manipulated as potential therapeutic targets in the electromechanical and pharmaco-mechanical coupling as shown in **Figure 5.1**.

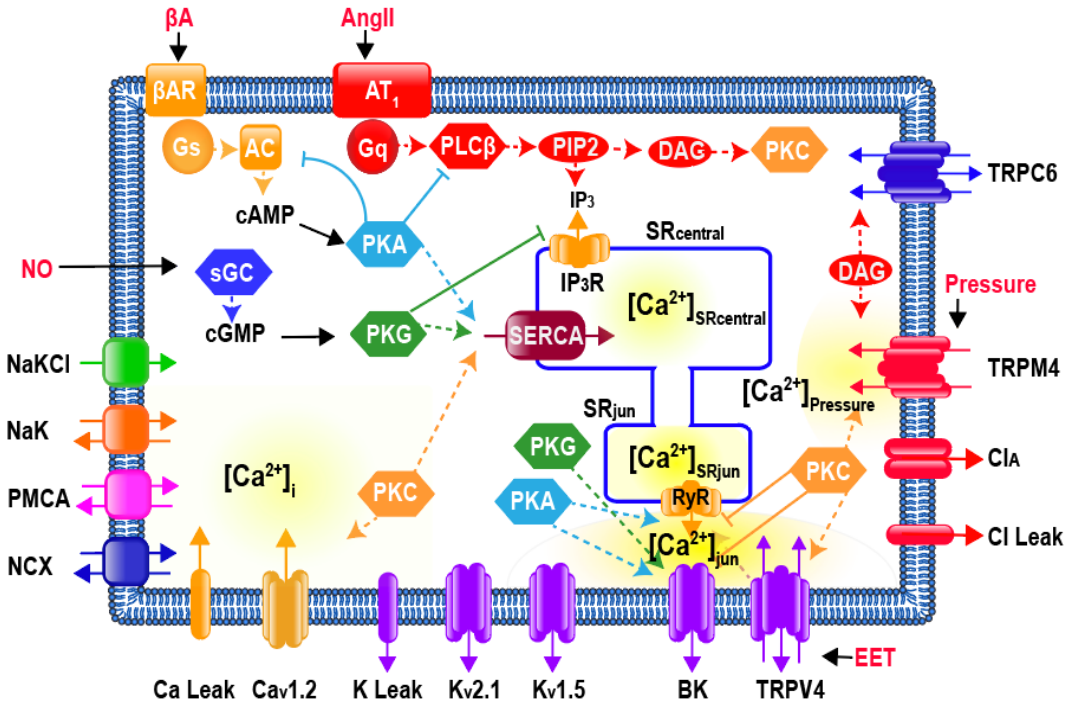

Figure 5.1. The extended model including the electromechanical and pharmaco-mechanical coupling of a single vascular smooth muscle cell.

References

[1] "Ganong's review of medical physiology," ed. New York: McGraw-Hill Medical, 2010.

[2] L. A. Martinez-Lemus, "The dynamic structure of arterioles," *Basic Clin Pharmacol Toxicol,* vol. 110, no. 1, pp. 5-11, Jan 2012, doi: 10.1111/j.1742-7843.2011.00813.x.

[3] K. L. Christensen and M. J. Mulvany, "Location of resistance arteries," *J Vasc Res,* vol. 38, no. 1, pp. 1-12, Jan-Feb 2001, doi: 10.1159/000051024.

[4] W. M. Bayliss, "On the local reaction of the arterial wall to changes in internal pressure," *Journal of Physiology,* vol. 28, pp. 220-231, 1902.

[5] M. J. Davis and M. A. Hill, "Signaling mechanisms underlying the vascular myogenic response," *Physiol Rev,* vol. 79, no. 2, pp. 387-423, Apr 1999, doi: 10.1152/physrev.1999.79.2.387.

[6] H. L. Brinks and A. D. Eckhart, "Regulation of GPCR signaling in hypertension," *Biochim Biophys Acta,* vol. 1802, no. 12, pp. 1268-75, Dec 2010, doi: 10.1016/j.bbadis.2010.01.005.

[7] K. L. Christensen and M. J. Mulvany, "Mesenteric arcade arteries contribute substantially to vascular resistance in conscious rats," *J Vasc Res,* vol. 30, no. 2, pp. 73-9, Mar-Apr 1993, doi: 10.1159/000158978.

[8] S. D. Crowley *et al.*, "Angiotensin II causes hypertension and cardiac hypertrophy through its receptors in the kidney," *Proc Natl Acad Sci U S A,* vol. 103, no. 47, pp. 17985-90, Nov 21 2006, doi: 10.1073/pnas.0605545103.

[9] J. Leete and A. T. Layton, "Sex-specific long-term blood pressure regulation: Modeling and analysis," *Comput Biol Med,* vol. 104, pp. 139-148, Jan 2019, doi: 10.1016/j.compbiomed.2018.11.002.

[10] Y. Ouchi, L. Share, J. T. Crofton, K. Iitake, and D. P. Brooks, "Sex difference in the development of deoxycorticosterone-salt hypertension in the rat," *Hypertension,* vol. 9, no. 2, pp. 172-7, Feb 1987, doi: 10.1161/01.hyp.9.2.172.

[11] N. Wiinberg *et al.*, "24-h ambulatory blood pressure in 352 normal Danish subjects, related to age and gender," *Am J Hypertens,* vol. 8, no. 10 Pt 1, pp. 978-86, Oct 1995, doi: 10.1016/0895-7061(95)00216-2.

[12] Q. Gu, V. L. Burt, R. Paulose-Ram, and C. F. Dillon, "Gender differences in hypertension treatment, drug utilization patterns, and blood pressure control among US adults with hypertension: data from the National Health and Nutrition Examination Survey 1999-2004," *Am J Hypertens,* vol. 21, no. 7, pp. 789-98, Jul 2008, doi: 10.1038/ajh.2008.185.

[13] D. M. Rabi, N. Khan, M. Vallee, M. A. Hladunewich, S. W. Tobe, and L. Pilote, "Reporting on sex-based analysis in clinical trials of angiotensin-converting enzyme inhibitor and angiotensin receptor blocker efficacy," *Can J Cardiol,* vol. 24, no. 6, pp. 491-6, Jun 2008, doi: 10.1016/s0828-282x(08)70624-x.

[14] P. Dayan and L. F. Abbott, *Theoretical neuroscience : computational and mathematical modeling of neural systems* (Computational neuroscience). Cambridge, Mass.: Massachusetts Institute of Technology Press, 2001, pp. xv, 460 p.

[15] S. C. O'Dwyer *et al.*, "Kv2.1 channels play opposing roles in regulating membrane potential, Ca(2+) channel function, and myogenic tone in arterial smooth muscle," *Proc Natl Acad Sci U S A,* vol. 117, no. 7, pp. 3858-3866, Feb 18 2020, doi: 10.1073/pnas.1917879117.
[16] N. R. Tykocki, E. M. Boerman, and W. F. Jackson, "Smooth Muscle Ion Channels and Regulation of Vascular Tone in Resistance Arteries and Arterioles," *Compr Physiol,* vol. 7, no. 2, pp. 485-581, Mar 16 2017, doi: 10.1002/cphy.c160011.
[17] M. F. Navedo and L. F. Santana, "Cav1.2 sparklets in heart and vascular smooth muscle," *J Mol Cell Cardiol,* vol. 58, pp. 67-76, May 2013, doi: 10.1016/j.yjmcc.2012.11.018.
[18] M. F. Navedo, G. C. Amberg, V. S. Votaw, and L. F. Santana, "Constitutively active L-type Ca2+ channels," *Proc Natl Acad Sci U S A,* vol. 102, no. 31, pp. 11112-7, Aug 2 2005, doi: 10.1073/pnas.0500360102.
[19] G. C. Amberg, M. F. Navedo, M. Nieves-Cintron, J. D. Molkentin, and L. F. Santana, "Calcium sparklets regulate local and global calcium in murine arterial smooth muscle," *J Physiol,* vol. 579, no. Pt 1, pp. 187-201, Feb 15 2007, doi: 10.1113/jphysiol.2006.124420.
[20] M. Rubart, J. B. Patlak, and M. T. Nelson, "Ca2+ currents in cerebral artery smooth muscle cells of rat at physiological Ca2+ concentrations," *J Gen Physiol,* vol. 107, no. 4, pp. 459-72, Apr 1996, doi: 10.1085/jgp.107.4.459.
[21] B. K. Fleischmann, R. K. Murray, and M. I. Kotlikoff, "Voltage window for sustained elevation of cytosolic calcium in smooth muscle cells," *Proc Natl Acad Sci U S A,* vol. 91, no. 25, pp. 11914-8, Dec 6 1994, doi: 10.1073/pnas.91.25.11914.
[22] M. T. Nelson, J. B. Patlak, J. F. Worley, and N. B. Standen, "Calcium channels, potassium channels, and voltage dependence of arterial smooth muscle tone," *Am J Physiol,* vol. 259, no. 1 Pt 1, pp. C3-18, Jul 1990, doi: 10.1152/ajpcell.1990.259.1.C3.
[23] S. Earley, B. J. Waldron, and J. E. Brayden, "Critical role for transient receptor potential channel TRPM4 in myogenic constriction of cerebral arteries," *Circ Res,* vol. 95, no. 9, pp. 922-9, Oct 29 2004, doi: 10.1161/01.RES.0000147311.54833.03.
[24] M. A. Spassova, T. Hewavitharana, W. Xu, J. Soboloff, and D. L. Gill, "A common mechanism underlies stretch activation and receptor activation of TRPC6 channels," (in eng), *Proceedings of the National Academy of Sciences,* vol. 103, no. 44, pp. 16586-91, Oct 31 2006.
[25] S. Earley, T. J. Heppner, M. T. Nelson, and J. E. Brayden, "TRPV4 forms a novel Ca2+ signaling complex with ryanodine receptors and BKCa channels," *Circ Res,* vol. 97, no. 12, pp. 1270-9, Dec 9 2005, doi: 10.1161/01.RES.0000194321.60300.d6.
[26] J. Mercado *et al.*, "Local control of TRPV4 channels by AKAP150-targeted PKC in arterial smooth muscle," *J Gen Physiol,* vol. 143, no. 5, pp. 559-75, May 2014, doi: 10.1085/jgp.201311050.
[27] Y. Nakamura, Y. Ohya, I. Abe, and M. Fujishima, "Sodium-potassium pump current in smooth muscle cells from mesenteric resistance arteries of the guinea-

pig," *J Physiol,* vol. 519 Pt 1, pp. 203-12, Aug 15 1999, doi: 10.1111/j.1469-7793.1999.0203o.x.
[28] J. Zhang *et al.*, "Knockout of Na+/Ca2+ exchanger in smooth muscle attenuates vasoconstriction and L-type Ca2+ channel current and lowers blood pressure," *Am J Physiol Heart Circ Physiol,* vol. 298, no. 5, pp. H1472-83, May 2010, doi: 10.1152/ajpheart.00964.2009.
[29] M. Kassmann *et al.*, "Role of Ryanodine Type 2 Receptors in Elementary Ca(2+) Signaling in Arteries and Vascular Adaptive Responses," *J Am Heart Assoc,* vol. 8, no. 9, p. e010090, May 7 2019, doi: 10.1161/JAHA.118.010090.
[30] M. A. Spassova, T. Hewavitharana, W. Xu, J. Soboloff, and D. L. Gill, "A common mechanism underlies stretch activation and receptor activation of TRPC6 channels," *Proc Natl Acad Sci U S A,* vol. 103, no. 44, pp. 16586-91, Oct 31 2006, doi: 10.1073/pnas.0606894103.
[31] S. Bulley *et al.*, "Arterial smooth muscle cell PKD2 (TRPP1) channels regulate systemic blood pressure," *Elife,* vol. 7, Dec 4 2018, doi: 10.7554/eLife.42628.
[32] A. L. Gonzales *et al.*, "A PLCgamma1-dependent, force-sensitive signaling network in the myogenic constriction of cerebral arteries," *Science Signaling,* vol. 7, no. 327, p. ra49, 2014, doi: 10.1126/scisignal.2004732.
[33] A. P. Somlyo and A. V. Somlyo, "Signal transduction and regulation in smooth muscle," *Nature,* vol. 372, no. 6503, pp. 231-6, Nov 17 1994, doi: 10.1038/372231a0.
[34] M. T. Nelson *et al.*, "Relaxation of arterial smooth muscle by calcium sparks," *Science,* vol. 270, no. 5236, pp. 633-7, Oct 27 1995, doi: 10.1126/science.270.5236.633.
[35] G. C. Amberg and L. F. Santana, "Kv2 channels oppose myogenic constriction of rat cerebral arteries," *Am J Physiol Cell Physiol,* vol. 291, no. 2, pp. C348-56, Aug 2006, doi: 10.1152/ajpcell.00086.2006.
[36] F. Plane *et al.*, "Heteromultimeric Kv1 channels contribute to myogenic control of arterial diameter," *Circ Res,* vol. 96, no. 2, pp. 216-24, Feb 4 2005.
[37] D. Sato *et al.*, "A stochastic model of ion channel cluster formation in the plasma membrane," *J Gen Physiol,* vol. 151, no. 9, pp. 1116-1134, Sep 2 2019, doi: 10.1085/jgp.201912327.
[38] V. Pucovsky and T. B. Bolton, "Localisation, function and composition of primary Ca(2+) spark discharge region in isolated smooth muscle cells from guinea-pig mesenteric arteries," *Cell Calcium,* vol. 39, no. 2, pp. 113-29, Feb 2006, doi: 10.1016/j.ceca.2005.10.002.
[39] D. C. Hill-Eubanks, M. E. Werner, T. J. Heppner, and M. T. Nelson, "Calcium Signaling in Smooth Muscle," (in English), *Cold Spring Harbor Perspectives in Biology,* vol. 3, no. 9, Sep 2011, doi: ARTN a00454910.1101/cshperspect.a004549.
[40] S. L. Archer *et al.*, "Molecular identification of the role of voltage-gated K+ channels, Kv1.5 and Kv2.1, in hypoxic pulmonary vasoconstriction and control of resting membrane potential in rat pulmonary artery myocytes," *J Clin Invest,* vol. 101, no. 11, pp. 2319-30, Jun 1 1998, doi: 10.1172/JCI333.
[41] Y. Lu, S. T. Hanna, G. Tang, and R. Wang, "Contributions of Kv1.2, Kv1.5 and Kv2.1 subunits to the native delayed rectifier K(+) current in rat mesenteric artery

smooth muscle cells," *Life Sci,* vol. 71, no. 12, pp. 1465-73, Aug 9 2002, doi: 10.1016/s0024-3205(02)01922-7.
[42] G. C. Amberg, C. F. Rossow, M. F. Navedo, and L. F. Santana, "NFATc3 regulates Kv2.1 expression in arterial smooth muscle," *J Biol Chem,* vol. 279, no. 45, pp. 47326-34, Nov 5 2004, doi: 10.1074/jbc.M408789200.
[43] X. Z. Zhong *et al.*, "Stromatoxin-sensitive, heteromultimeric Kv2.1/Kv9.3 channels contribute to myogenic control of cerebral arterial diameter," *J Physiol,* vol. 588, no. Pt 22, pp. 4519-37, Nov 15 2010, doi: 10.1113/jphysiol.2010.196618.
[44] R. C. Webb, "Smooth muscle contraction and relaxation," *Adv Physiol Educ,* vol. 27, no. 1-4, pp. 201-6, Dec 2003, doi: 10.1152/advan.00025.2003.
[45] J. P. Keener and J. Sneyd, *Mathematical physiology*, 2nd ed. (Interdisciplinary applied mathematics, no. 8). New York, NY: Springer, 2009.
[46] A. L. Hodgkin and A. F. Huxley, "A Quantitative Description of Membrane Current and Its Application to Conduction and Excitation in Nerve," (in English), *Journal of Physiology-London,* vol. 117, no. 4, pp. 500-544, 1952, doi: DOI 10.1113/jphysiol.1952.sp004764.
[47] B. Hille, *Ion channels of excitable membranes*, 3rd ed. Sunderland, Mass.: Sinauer, 2001, pp. xviii, 814 p.
[48] D. C. Kernik *et al.*, "A computational model of induced pluripotent stem-cell derived cardiomyocytes incorporating experimental variability from multiple data sources," *J Physiol,* vol. 597, no. 17, pp. 4533-4564, Sep 2019, doi: 10.1113/JP277724.
[49] A. J. Tanskanen and L. H. Alvarez, "Voltage noise influences action potential duration in cardiac myocytes," *Math Biosci,* vol. 208, no. 1, pp. 125-46, Jul 2007, doi: 10.1016/j.mbs.2006.09.023.
[50] J. H. Goldwyn and E. Shea-Brown, "The What and Where of Adding Channel Noise to the Hodgkin-Huxley Equations," (in English), *Plos Computational Biology,* vol. 7, no. 11, Nov 2011, doi: ARTN e100224710.1371/journal.pcbi.1002247.
[51] C. E. Clancy *et al.*, "Multiscale Modeling in the Clinic: Drug Design and Development," *Ann Biomed Eng,* vol. 44, no. 9, pp. 2591-610, Sep 2016, doi: 10.1007/s10439-016-1563-0.
[52] P. Pathmanathan and R. A. Gray, "Validation and Trustworthiness of Multiscale Models of Cardiac Electrophysiology," *Front Physiol,* vol. 9, p. 106, 2018, doi: 10.3389/fphys.2018.00106.
[53] D. Parthimos, D. H. Edwards, and T. M. Griffith, "Minimal model of arterial chaos generated by coupled intracellular and membrane Ca2+ oscillators," *Am J Physiol,* vol. 277, no. 3, pp. H1119-44, Sep 1999, doi: 10.1152/ajpheart.1999.277.3.H1119.
[54] J. Yang, J. W. Clark, Jr., R. M. Bryan, and C. Robertson, "The myogenic response in isolated rat cerebrovascular arteries: smooth muscle cell model," *Med Eng Phys,* vol. 25, no. 8, pp. 691-709, Oct 2003, doi: 10.1016/s1350-4533(03)00100-0.
[55] J. C. Jacobsen, C. Aalkjaer, H. Nilsson, V. V. Matchkov, J. Freiberg, and N. H. Holstein-Rathlou, "Activation of a cGMP-sensitive calcium-dependent chloride

channel may cause transition from calcium waves to whole cell oscillations in smooth muscle cells," *Am J Physiol Heart Circ Physiol,* vol. 293, no. 1, pp. H215-28, Jul 2007, doi: 10.1152/ajpheart.00726.2006.

[56] A. Kapela, A. Bezerianos, and N. M. Tsoukias, "A mathematical model of Ca2+ dynamics in rat mesenteric smooth muscle cell: agonist and NO stimulation," *J Theor Biol,* vol. 253, no. 2, pp. 238-60, Jul 21 2008, doi: 10.1016/j.jtbi.2008.03.004.

[57] A. Karlin, "Membrane potential and Ca2+ concentration dependence on pressure and vasoactive agents in arterial smooth muscle: A model," *J Gen Physiol,* vol. 146, no. 1, pp. 79-96, Jul 2015, doi: 10.1085/jgp.201511380.

[58] W. C. Tong, C. Y. Choi, S. Karche, A. V. Holden, H. G. Zhang, and M. J. Taggart, "A Computational Model of the Ionic Currents, Ca2+ Dynamics and Action Potentials Underlying Contraction of Isolated Uterine Smooth Muscle," (in English), *Plos One,* vol. 6, no. 4, Apr 29 2011, doi: ARTN e1868510.1371/journal.pone.0018685.

[59] C. H. Luo and Y. Rudy, "A dynamic model of the cardiac ventricular action potential. I. Simulations of ionic currents and concentration changes," *Circ Res,* vol. 74, no. 6, pp. 1071-96, Jun 1994, doi: 10.1161/01.res.74.6.1071.

[60] K. H. ten Tusscher, D. Noble, P. J. Noble, and A. V. Panfilov, "A model for human ventricular tissue," *Am J Physiol Heart Circ Physiol,* vol. 286, no. 4, pp. H1573-89, Apr 2004, doi: 10.1152/ajpheart.00794.2003.

[61] G. J. Kargacin, "Calcium signaling in restricted diffusion spaces," *Biophys J,* vol. 67, no. 1, pp. 262-72, Jul 1994, doi: 10.1016/S0006-3495(94)80477-1.

[62] R. ZhuGe, R. A. Tuft, K. E. Fogarty, K. Bellve, F. S. Fay, and J. V. Walsh, Jr., "The influence of sarcoplasmic reticulum Ca2+ concentration on Ca2+ sparks and spontaneous transient outward currents in single smooth muscle cells," *J Gen Physiol,* vol. 113, no. 2, pp. 215-28, Feb 1999, doi: 10.1085/jgp.113.2.215.

[63] L. Bao and D. H. Cox, "Gating and ionic currents reveal how the BKCa channel's Ca2+ sensitivity is enhanced by its beta 1 subunit," (in English), *Journal of General Physiology,* vol. 126, no. 4, pp. 393-412, Oct 2005, doi: 10.1085/jgp.200509346.

[64] R. Zhuge, K. E. Fogarty, R. A. Tuft, and J. V. Walsh, Jr., "Spontaneous transient outward currents arise from microdomains where BK channels are exposed to a mean Ca(2+) concentration on the order of 10 microM during a Ca(2+) spark," *J Gen Physiol,* vol. 120, no. 1, pp. 15-27, Jul 2002, doi: 10.1085/jgp.20028571.

[65] L. Dwyer *et al.*, "Basally activated nonselective cation currents regulate the resting membrane potential in human and monkey colonic smooth muscle," (in English), *American Journal of Physiology-Gastrointestinal and Liver Physiology,* vol. 301, no. 2, pp. G287-G296, Aug 2011, doi: 10.1152/ajpgi.00415.2010.

[66] M. Setoguchi, Y. Ohya, I. Abe, and M. Fujishima, "Stretch-activated whole-cell currents in smooth muscle cells from mesenteric resistance artery of guinea-pig," (in English), *Journal of Physiology-London,* vol. 501, no. 2, pp. 343-353, Jun 1 1997, doi: DOI 10.1111/j.1469-7793.1997.343bn.x.

[67] S. Earley, S. V. Straub, and J. E. Brayden, "Protein kinase C regulates vascular myogenic tone through activation of TRPM4," *Am J Physiol Heart Circ Physiol,* vol. 292, no. 6, pp. H2613-22, Jun 2007, doi: 10.1152/ajpheart.01286.2006.

[68] R. Bychkov, M. Gollasch, C. Ried, F. C. Luft, and H. Haller, "Regulation of spontaneous transient outward potassium currents in human coronary arteries," *Circulation,* vol. 95, no. 2, pp. 503-10, Jan 21 1997, doi: 10.1161/01.cir.95.2.503.
[69] M. Desilets, S. P. Driska, and C. M. Baumgarten, "Current Fluctuations and Oscillations in Smooth-Muscle Cells from Hog Carotid-Artery - Role of the Sarcoplasmic-Reticulum," (in English), *Circulation Research,* vol. 65, no. 3, pp. 708-722, Sep 1989, doi: Doi 10.1161/01.Res.65.3.708.
[70] Y. M. Bae, M. K. Park, S. H. Lee, W. K. Ho, and Y. E. Earm, "Contribution of Ca2+-activated K+ channels and non-selective cation channels to membrane potential of pulmonary arterial smooth muscle cells of the rabbit," *J Physiol,* vol. 514 (Pt 3), pp. 747-58, Feb 1 1999, doi: 10.1111/j.1469-7793.1999.747ad.x.
[71] L. Guarina *et al.*, "Biological noise is a key determinant of the reproducibility and adaptability of cardiac pacemaking and EC coupling," *J Gen Physiol,* vol. 154, no. 9, Sep 5 2022, doi: 10.1085/jgp.202012613.
[72] J. H. Jaggar, V. A. Porter, W. J. Lederer, and M. T. Nelson, "Calcium sparks in smooth muscle," *Am J Physiol Cell Physiol,* vol. 278, no. 2, pp. C235-56, Feb 2000, doi: 10.1152/ajpcell.2000.278.2.C235.
[73] I. N. Bratz, A. N. Swafford, N. L. Kanagy, and G. M. Dick, "Reduced functional expression of K+ channels in vascular smooth muscle cells from rats made hypertensive with N-omega-nitro-L-arginine," (in English), *American Journal of Physiology-Heart and Circulatory Physiology,* vol. 289, no. 3, pp. H1284-H1290, Sep 2005, doi: 10.1152/ajpheart.01053.2004.
[74] D. J. Sung *et al.*, "Serotonin contracts the rat mesenteric artery by inhibiting 4-aminopyridine-sensitive Kv channels via the 5-HT2A receptor and Src tyrosine kinase," *Exp Mol Med,* vol. 45, p. e67, Dec 13 2013, doi: 10.1038/emm.2013.116.
[75] C. van Breemen, N. Fameli, and A. M. Evans, "Pan-junctional sarcoplasmic reticulum in vascular smooth muscle: nanospace Ca2+ transport for site- and function-specific Ca2+ signalling," *J Physiol,* vol. 591, no. 8, pp. 2043-54, Apr 15 2013, doi: 10.1113/jphysiol.2012.246348.
[76] H. A. T. Pritchard *et al.*, "Nanoscale coupling of junctophilin-2 and ryanodine receptors regulates vascular smooth muscle cell contractility," *Proc Natl Acad Sci U S A,* vol. 116, no. 43, pp. 21874-21881, Oct 22 2019, doi: 10.1073/pnas.1911304116.
[77] A. M. Evans, "Nanojunctions of the Sarcoplasmic Reticulum Deliver Site- and Function-Specific Calcium Signaling in Vascular Smooth Muscles," *Adv Pharmacol,* vol. 78, pp. 1-47, 2017, doi: 10.1016/bs.apha.2016.10.001.
[78] E. A. Ko, W. S. Park, A. L. Firth, N. Kim, J. X. Yuan, and J. Han, "Pathophysiology of voltage-gated K+ channels in vascular smooth muscle cells: modulation by protein kinases," *Prog Biophys Mol Biol,* vol. 103, no. 1, pp. 95-101, Sep 2010, doi: 10.1016/j.pbiomolbio.2009.10.001.
[79] B. K. Joseph, K. M. Thakali, C. L. Moore, and S. W. Rhee, "Ion channel remodeling in vascular smooth muscle during hypertension: Implications for novel therapeutic approaches," (in English), *Pharmacological Research,* vol. 70, no. 1, pp. 126-138, Apr 2013, doi: 10.1016/j.phrs.2013.01.008.

[80] R. H. Cox and I. M. Lozinskaya, "Ca2+ channel inactivation in small mesenteric arteries of WKY and SHR," *Am J Hypertens,* vol. 21, no. 4, pp. 406-12, Apr 2008, doi: 10.1038/ajh.2007.73.
[81] Y. M. Bae *et al.*, "Serotonin depolarizes the membrane potential in rat mesenteric artery myocytes by decreasing voltage-gated K+ currents," *Biochem Biophys Res Commun,* vol. 347, no. 2, pp. 468-76, Aug 25 2006, doi: 10.1016/j.bbrc.2006.06.116.
[82] N. R. Tykocki and M. T. Nelson, "Location, Location, Location: Juxtaposed calcium-signaling microdomains as a novel model of the vascular smooth muscle myogenic response," (in English), *Journal of General Physiology,* vol. 146, no. 2, pp. 129-132, Aug 2015, doi: 10.1085/jgp.201511468.
[83] V. V. Matchkov, C. Aalkjaer, and H. Nilsson, "A cyclic GMP-dependent calcium-activated chloride current in smooth-muscle cells from rat mesenteric resistance arteries," *J Gen Physiol,* vol. 123, no. 2, pp. 121-34, Feb 2004, doi: 10.1085/jgp.200308972.
[84] J. Goyette and K. Gaus, "Mechanisms of protein nanoscale clustering," *Curr Opin Cell Biol,* vol. 44, pp. 86-92, Feb 2017, doi: 10.1016/j.ceb.2016.09.004.
[85] A. Honigmann and A. Pralle, "Compartmentalization of the Cell Membrane," *J Mol Biol,* vol. 428, no. 24 Pt A, pp. 4739-4748, Dec 4 2016, doi: 10.1016/j.jmb.2016.09.022.
[86] D. Krapf, "Compartmentalization of the plasma membrane," *Curr Opin Cell Biol,* vol. 53, pp. 15-21, Aug 2018, doi: 10.1016/j.ceb.2018.04.002.
[87] R. M. Shaw and H. M. Colecraft, "L-type calcium channel targeting and local signalling in cardiac myocytes," *Cardiovasc Res,* vol. 98, no. 2, pp. 177-86, May 1 2013, doi: 10.1093/cvr/cvt021.
[88] R. D. Taylor, M. Heine, N. J. Emptage, and L. C. Andreae, "Neuronal Receptors Display Cytoskeleton-Independent Directed Motion on the Plasma Membrane," *iScience,* vol. 10, pp. 234-244, Dec 21 2018, doi: 10.1016/j.isci.2018.12.001.
[89] D. Ghosh *et al.*, "Dynamic L-type CaV1.2 channel trafficking facilitates CaV1.2 clustering and cooperative gating," *Biochim Biophys Acta Mol Cell Res,* vol. 1865, no. 9, pp. 1341-1355, Sep 2018, doi: 10.1016/j.bbamcr.2018.06.013.
[90] W. I. Newman, D. L. Turcotte, and B. D. Malamud, "Emergence of patterns in random processes," *Phys Rev E Stat Nonlin Soft Matter Phys,* vol. 86, no. 2 Pt 2, p. 026103, Aug 2012, doi: 10.1103/PhysRevE.86.026103.
[91] K. G. Beam, J. H. Caldwell, and D. T. Campbell, "Na channels in skeletal muscle concentrated near the neuromuscular junction," *Nature,* vol. 313, no. 6003, pp. 588-90, Feb 14-20 1985, doi: 10.1038/313588a0.
[92] W. A. Catterall, "Localization of sodium channels in cultured neural cells," *J Neurosci,* vol. 1, no. 7, pp. 777-83, Jul 1981.
[93] S. G. Waxman and J. M. Ritchie, "Organization of ion channels in the myelinated nerve fiber," *Science,* vol. 228, no. 4707, pp. 1502-7, Jun 28 1985, doi: 10.1126/science.2409596.
[94] B. A. Block, T. Imagawa, K. P. Campbell, and C. Franziniarmstrong, "Structural Evidence for Direct Interaction between the Molecular-Components of the Transverse Tubule Sarcoplasmic-Reticulum Junction in Skeletal-Muscle," (in

English), *Journal of Cell Biology,* vol. 107, no. 6, pp. 2587-2600, Dec 1988, doi: DOI 10.1083/jcb.107.6.2587.
[95] R. Duffin *et al.*, "The CDK inhibitor, R-roscovitine, promotes eosinophil apoptosis by down-regulation of Mcl-1," *FEBS Lett,* vol. 583, no. 15, pp. 2540-6, Aug 6 2009, doi: 10.1016/j.febslet.2009.07.017.
[96] D. V. Gathercole, D. J. Colling, J. N. Skepper, Y. Takagishi, A. J. Levi, and N. J. Severs, "Immunogold-labeled L-type calcium channels are clustered in the surface plasma membrane overlying junctional sarcoplasmic reticulum in guinea-pig myocytes-implications for excitation-contraction coupling in cardiac muscle," *J Mol Cell Cardiol,* vol. 32, no. 11, pp. 1981-94, Nov 2000, doi: 10.1006/jmcc.2000.1230.
[97] Y. Takagishi, S. Rothery, J. Issberner, A. Levi, and N. J. Severs, "Spatial distribution of dihydropyridine receptors in the plasma membrane of guinea pig cardiac myocytes investigated by correlative confocal microscopy and label-fracture electron microscopy," *J Electron Microsc (Tokyo),* vol. 46, no. 2, pp. 165-70, 1997, doi: 10.1093/oxfordjournals.jmicro.a023504.
[98] A. O. Jorgensen, W. Arnold, A. C. Y. Shen, S. H. Yuan, M. Gaver, and K. P. Campbell, "Identification of Novel Proteins Unique to Either Transverse Tubules (Ts28) or the Sarcolemma (Sl50) in Rabbit Skeletal-Muscle," (in English), *Journal of Cell Biology,* vol. 110, no. 4, pp. 1173-1185, Apr 1990, doi: DOI 10.1083/jcb.110.4.1173.
[99] O. Vivas, C. M. Moreno, L. F. Santana, and B. Hille, "Proximal clustering between BK and CaV1.3 channels promotes functional coupling and BK channel activation at low voltage," *Elife,* vol. 6, Jun 30 2017, doi: 10.7554/eLife.28029.
[100] R. E. Dixon *et al.*, "Graded Ca(2)(+)/calmodulin-dependent coupling of voltage-gated CaV1.2 channels," *Elife,* vol. 4, Feb 25 2015, doi: 10.7554/eLife.05608.
[101] C. M. Moreno *et al.*, "Ca(2+) entry into neurons is facilitated by cooperative gating of clustered CaV1.3 channels," *Elife,* vol. 5, May 17 2016, doi: 10.7554/eLife.15744.
[102] S. Tajada *et al.*, "Distance constraints on activation of TRPV4 channels by AKAP150-bound PKCalpha in arterial myocytes," *J Gen Physiol,* vol. 149, no. 6, pp. 639-659, Jun 5 2017, doi: 10.1085/jgp.201611709.
[103] D. Baddeley, I. D. Jayasinghe, L. Lam, S. Rossberger, M. B. Cannell, and C. Soeller, "Optical single-channel resolution imaging of the ryanodine receptor distribution in rat cardiac myocytes," *Proc Natl Acad Sci U S A,* vol. 106, no. 52, pp. 22275-80, Dec 29 2009, doi: 10.1073/pnas.0908971106.
[104] E. Kim, K. O. Cho, A. Rothschild, and M. Sheng, "Heteromultimerization and NMDA receptor-clustering activity of Chapsyn-110, a member of the PSD-95 family of proteins," *Neuron,* vol. 17, no. 1, pp. 103-13, Jul 1996, doi: 10.1016/s0896-6273(00)80284-6.
[105] E. Kim, M. Niethammer, A. Rothschild, Y. N. Jan, and M. Sheng, "Clustering of Shaker-type K+ channels by interaction with a family of membrane-associated guanylate kinases," *Nature,* vol. 378, no. 6552, pp. 85-8, Nov 2 1995, doi: 10.1038/378085a0.

[106] D. H. Cox, "Modeling a Ca2+ Channel/BKCa Channel Complex at the Single-Complex Level," (in English), *Biophysical Journal,* vol. 107, no. 12, pp. 2797-2814, Dec 16 2014, doi: 10.1016/j.bpj.2014.10.069.
[107] D. Shiomi, M. Yoshimoto, M. Homma, and I. Kawagishi, "Helical distribution of the bacterial chemoreceptor via colocalization with the Sec protein translocation machinery," (in English), *Molecular Microbiology,* vol. 60, no. 4, pp. 894-906, May 2006, doi: 10.1111/j.1365-2958.2006.05145.x.
[108] S. Thiem, D. Kentner, and V. Sourjik, "Positioning of chemosensory clusters in E. coli and its relation to cell division," (in English), *Embo Journal,* vol. 26, no. 6, pp. 1615-1623, Mar 21 2007, doi: 10.1038/sj.emboj.7601610.
[109] H. Wang, N. S. Wingreen, and R. Mukhopadhyay, "Self-Organized Periodicity of Protein Clusters in Growing Bacteria," (in English), *Physical Review Letters,* vol. 101, no. 21, Nov 21 2008, doi: ARTN 21810110.1103/PhysRevLett.101.218101.
[110] A. De La Mata *et al.*, "BIN1 Induces the Formation of T-Tubules and Adult-Like Ca(2+) Release Units in Developing Cardiomyocytes," *Stem Cells,* vol. 37, no. 1, pp. 54-64, Jan 2019, doi: 10.1002/stem.2927.
[111] G. T. Dempsey, J. C. Vaughan, K. H. Chen, and X. W. Zhuang, "Evaluation of Fluorophores for Optimal Performance in Localization-Based Super-Resolution Imaging," (in English), *Biophysical Journal,* vol. 102, no. 3, pp. 725a-725a, Jan 31 2012, doi: DOI 10.1016/j.bpj.2011.11.3934.
[112] J. Folling *et al.*, "Fluorescence nanoscopy by ground-state depletion and single-molecule return," (in English), *Nature Methods,* vol. 5, no. 11, pp. 943-945, Nov 2008, doi: 10.1038/nmeth.1257.
[113] A. McEvoy *et al.*, "Self-Organization of the Escherichia Coli Chemotaxis Network Imaged with Super-Resolution Light Microscopy," (in English), *Biophysical Journal,* vol. 98, no. 3, pp. 760a-760a, Jan 2010, doi: DOI 10.1016/j.bpj.2009.12.4175.
[114] W. Stuhmer and W. Almers, "Photobleaching through glass micropipettes: sodium channels without lateral mobility in the sarcolemma of frog skeletal muscle," *Proc Natl Acad Sci U S A,* vol. 79, no. 3, pp. 946-50, Feb 1982, doi: 10.1073/pnas.79.3.946.
[115] E. M. Green, C. F. Barrett, G. Bultynck, S. M. Shamah, and R. E. Dolmetsch, "The tumor suppressor eIF3e mediates calcium-dependent internalization of the L-type calcium channel Ca(v)1.2," (in English), *Neuron,* vol. 55, no. 4, pp. 615-632, Aug 16 2007, doi: 10.1016/j.neuron.2007.07.024.
[116] J. Wu *et al.*, "Structure of the voltage-gated calcium channel Cav1.1 complex," *Science,* vol. 350, no. 6267, p. aad2395, Dec 18 2015, doi: 10.1126/science.aad2395.
[117] H. Shigematsu, T. Sokabe, R. Danev, M. Tominaga, and K. Nagayama, "A 3.5-nm structure of rat TRPV4 cation channel revealed by Zernike phase-contrast cryoelectron microscopy," *J Biol Chem,* vol. 285, no. 15, pp. 11210-8, Apr 9 2010, doi: 10.1074/jbc.M109.090712.
[118] Z. Deng *et al.*, "Cryo-EM and X-ray structures of TRPV4 reveal insight into ion permeation and gating mechanisms," *Nat Struct Mol Biol,* vol. 25, no. 3, pp. 252-260, Mar 2018, doi: 10.1038/s41594-018-0037-5.

[119] R. Conrad *et al.*, "Rapid Turnover of the Cardiac L-Type CaV1.2 Channel by Endocytic Recycling Regulates Its Cell Surface Availability," *iScience,* vol. 7, pp. 1-15, Sep 28 2018, doi: 10.1016/j.isci.2018.08.012.
[120] V. Di Biase, P. Tuluc, M. Campiglio, G. J. Obermair, M. Heine, and B. E. Flucher, "Surface traffic of dendritic CaV1.2 calcium channels in hippocampal neurons," *J Neurosci,* vol. 31, no. 38, pp. 13682-94, Sep 21 2011, doi: 10.1523/JNEUROSCI.2300-11.2011.
[121] B. Schwanhausser *et al.*, "Global quantification of mammalian gene expression control," *Nature,* vol. 473, no. 7347, pp. 337-42, May 19 2011, doi: 10.1038/nature10098.
[122] C. F. Rossow, K. W. Dilly, and L. F. Santana, "Differential calcineurin/NFATc3 activity contributes to the Ito transmural gradient in the mouse heart," *Circ Res,* vol. 98, no. 10, pp. 1306-13, May 26 2006, doi: 10.1161/01.RES.0000222028.92993.10.
[123] C. F. Rossow, K. W. Dilly, C. Yuan, M. Nieves-Cintron, J. L. Cabarrus, and L. F. Santana, "NFATc3-dependent loss of I-to gradient across the left ventricular wall during chronic beta adrenergic stimulation," (in English), *Journal of Molecular and Cellular Cardiology,* vol. 46, no. 2, pp. 249-256, Feb 2009, doi: 10.1016/j.yjmcc.2008.10.016.
[124] C. F. Rossow, E. Minami, E. G. Chase, C. E. Murry, and L. F. Santana, "NFATc3-induced reductions in voltage-gated K+ currents after myocardial infarction," *Circ Res,* vol. 94, no. 10, pp. 1340-50, May 28 2004, doi: 10.1161/01.RES.0000128406.08418.34.
[125] M. Nieves-Cintron, G. C. Amberg, M. F. Navedo, J. D. Molkentin, and L. F. Santana, "The control of Ca2+ influx and NFATc3 signaling in arterial smooth muscle during hypertension," (in English), *Proceedings of the National Academy of Sciences of the United States of America,* vol. 105, no. 40, pp. 15623-15628, Oct 7 2008, doi: 10.1073/pnas.0808759105.
[126] M. Nieves-Cintron, G. C. Amberg, C. B. Nichols, J. D. Molkentin, and L. F. Santana, "Activation of NFATc3 down-regulates the beta1 subunit of large conductance, calcium-activated K+ channels in arterial smooth muscle and contributes to hypertension," *J Biol Chem,* vol. 282, no. 5, pp. 3231-40, Feb 2 2007, doi: 10.1074/jbc.M608822200.
[127] J. Adam, N. Basnet, and N. Mizuno, "Structural insights into the cooperative remodeling of membranes by amphiphysin/BIN1," (in English), *Scientific Reports,* vol. 5, Oct 21 2015, doi: ARTN 1545210.1038/srep15452.
[128] E. Lee *et al.*, "Amphiphysin 2 (BIN1) and T-tubule biogenesis in muscle," (in English), *Molecular Biology of the Cell,* vol. 13, pp. 460a-461a, Nov 2002.
[129] T. T. Hong *et al.*, "Cardiac BIN1 folds T-tubule membrane, controlling ion flux and limiting arrhythmia," (in English), *Nature Medicine,* vol. 20, no. 6, pp. 624-632, Jun 2014, doi: 10.1038/nm.3543.
[130] T. T. Hong *et al.*, "BIN1 Localizes the L-Type Calcium Channel to Cardiac T-Tubules," (in English), *Plos Biology,* vol. 8, no. 2, Feb 2010, doi: ARTN e100031210.1371/journal.pbio.1000312.

[131] T. Wegierski, K. Hill, M. Schaefer, and G. Walz, "The HECT ubiquitin ligase AIP4 regulates the cell surface expression of select TRP channels," *EMBO J,* vol. 25, no. 24, pp. 5659-69, Dec 13 2006, doi: 10.1038/sj.emboj.7601429.
[132] B. Rosati *et al.*, "Robust L-type calcium current expression following heterozygous knockout of the Cav1.2 gene in adult mouse heart," *J Physiol,* vol. 589, no. Pt 13, pp. 3275-88, Jul 1 2011, doi: 10.1113/jphysiol.2011.210237.
[133] C. D. Garciarena, Y. L. Ma, P. Swietach, L. Huc, and R. D. Vaughan-Jones, "Sarcolemmal localisation of Na+/H+ exchange and Na+-HCO3- co-transport influences the spatial regulation of intracellular pH in rat ventricular myocytes," *J Physiol,* vol. 591, no. 9, pp. 2287-306, May 1 2013, doi: 10.1113/jphysiol.2012.249664.
[134] G. K. Yuen, S. Galice, and D. M. Bers, "Subcellular localization of Na/K-ATPase isoforms in ventricular myocytes," *J Mol Cell Cardiol,* vol. 108, pp. 158-169, Jul 2017, doi: 10.1016/j.yjmcc.2017.05.013.
[135] J. R. Sanes and J. W. Lichtman, "Induction, assembly, maturation and maintenance of a postsynaptic apparatus," *Nat Rev Neurosci,* vol. 2, no. 11, pp. 791-805, Nov 2001, doi: 10.1038/35097557.
[136] A. D. Nelson and P. M. Jenkins, "Axonal Membranes and Their Domains: Assembly and Function of the Axon Initial Segment and Node of Ranvier," (in English), *Frontiers in Cellular Neuroscience,* vol. 11, May 9 2017, doi: ARTN 13610.3389/fncel.2017.00136.
[137] M. Kirmiz, N. C. Vierra, S. Palacio, and J. S. Trimmer, "Identification of VAPA and VAPB as Kv2 Channel-Interacting Proteins Defining Endoplasmic Reticulum-Plasma Membrane Junctions in Mammalian Brain Neurons," (in English), *Journal of Neuroscience,* vol. 38, no. 35, pp. 7562-7584, Aug 29 2018, doi: 10.1523/Jneurosci.0893-18.2018.
[138] B. Johnson, A. N. Leek, L. Sole, E. E. Maverick, T. P. Levine, and M. M. Tamkun, "Kv2 potassium channels form endoplasmic reticulum/plasma membrane junctions via interaction with VAPA and VAPB," (in English), *Proceedings of the National Academy of Sciences of the United States of America,* vol. 115, no. 31, pp. E7331-E7340, Jul 31 2018, doi: 10.1073/pnas.1805757115.